Master's thesis

NTNU
Norwegian University of Science and Technology
Faculty of Natural Sciences
Department of Materials Science and Engineering

Vetle Holum

The effect of soaking and electrical poling on domain structure and chemical surface properties of ferroelectric implant materials

Master's thesis in Chemical Engineering and Biotechnology
Supervisor: Julia Glaum
Co-supervisor: Marcus Hoseth Bentzen
June 2023

NTNU
Norwegian University of
Science and Technology

Vetle Holum

The effect of soaking and electrical poling on domain structure and chemical surface properties of ferroelectric implant materials

Master's thesis in Chemical Engineering and Biotechnology
Supervisor: Julia Glaum
Co-supervisor: Marcus Hoseth Bentzen
June 2023

Norwegian University of Science and Technology
Faculty of Natural Sciences
Department of Materials Science and Engineering

NTNU
Norwegian University of
Science and Technology

Abstract

This thesis aims to produce bulk barium titanate (BT, $BaTiO_3$), electrically charge (pole) the material, and soak it in different soaking media, for the purpose of studying the effect of soaking and electrical poling on the domain structure and chemical surface properties.

Barium titanate is a promising piezoelectric bioceramic in the use of bone implants. Natural bone possesses piezoelectricity, and the broader aim is to create an implant material that can mimic the natural regeneration and healing of bone. This is important for the over 2.5 million people yearly undergoing replacement surgeries. However, leaching of Ba^{2+} from the surface of $BaTiO_3$ can reduce the chemical stability, and threaten the lifetime of the implant. To address this, barium titanate was synthesized through a solid-state synthesis, before the material was poled using corona discharge. Afterward, the material was soaked in ultrapure water to study the change in domain structure, and the leaching of Ba^{2+}. The study gave great insight into the behavior of barium titanate in an electrical field. An increased poling resulted in an increasing piezoelectric coefficient, however, an effect of the poling on the domain structure was not observed. The study showed a strong indication that the Ba^{2+} leaching occurs mostly at the early stage of soaking. A second parallel of BT was soaked in simulated body fluid to study the precipitation on the surface, which can indicate the biocompatibility of $BaTiO_3$. This parallel revealed that an increase in soaking time and a larger electrical poling resulted in an increased amount of precipitation, stemming from the simulated body fluid. These results indicate that by creating an electrically charged surface of barium titanate, the material can become more biocompatible. After 5 days of soaking the piezoelectric properties were still upheld. Future research should focus on conducting a more thorough domain structure analysis and also study the effect of soaking over a larger time scale.

Sammendrag

Målet med denne masteravhandlingen er å produsere bariumtitanat (BT, $BaTiO_3$), påføre elektrisk ladning til (polarisere) materialet og bløtlegge det i ulike væskemedier. Dette gjøres for å studere hvordan væskene og den elektrisk ladde overflaten påvirker domenestrukturen og de kjemiske overflateegenskapene til materialet.

Bariumtitanat er et lovende piesoelektrisk biokeram og spesielt til bruken av beinimplantater. Bein produserer elektrisk ladning naturlig gjennom den piesoelektriske effekten, og det overordnede målet er å lage et implantatmateriale som kan etterligne kroppens naturlige regenerasjon og legning av beinet. Dette er viktig for over 2.5 millioner mennesker hvert år som gjennomgår et inngrep. Imidlertid, kan oppløsningen av Ba^{2+} fra overflaten av $BaTiO_3$ redusere den kjemiske stabiliteten og true levetiden til implantatet. For å håndtere dette, ble bariumtitanat syntetisert gjennom en faststoffsyntese, før materialet ble polarisert med en koronadischarge. Etterpå ble materialet lagt i ultrarent vann for å studere forandringen i domenestruktur og oppløsningen av Ba^{2+}. Studien ga betydelig innsikt i hvordan barium titanat oppfører seg i et elektrisk felt. Økende polarisering resulterte i en økning i den piesoelektriske koeffisienten, men det ble derimot ikke observert en effekt av polariseringen på domenestrukturen. Studien viste en sterk indikasjon på at det meste av oppløsningen av Ba^{2+} skjer i startfasen når materialet legges i væsken. En annen parallell av BT ble lagt i simulert kroppsvæske for å studere den kjemiske utfellingen på overflaten av prøven, som kan gi en indikasjon på biokompatibliteten til $BaTiO_3$. Denne parallellen avslørte at å la materialet ligge lengre i væsken og tilføre et større elektrisk felt til materialet, førte til en økende kjemisk utfelling på overflaten av BT, som stammer fra den simulerte kroppsvæsken. Disse resultatene indikerer at barium titanat kan bli mer biokompatibelt av å introdusere en elektrisk ladning til overflaten av materialet. Etter 5 dager med gjennombløting var de piesoelektriske egenskapene fortsatt intakt. Videre forskning burde fokusere på å gjennomføre en grundigere domenestruktur analyse og også studere effekten av å legge materialet i væske over en lengre tidsperiode.

Preface

The experimental work and the writing of the master's thesis were conducted as part of the course TMT4900, Materials Chemistry and Energy Technology, Master's Thesis. The research was carried out during the spring of 2023 as a continuation of the study performed in relation to the project work in TMT4500 from the fall of 2022 [1]. All the research was done at the Department of Material Science and Engineering (IMA) at the Norwegian University of Science of Technology (NTNU).

Acknowledgements

I would like to express my profound gratitude to my supervisor Julia Glaum and co-supervisor Marcus Bentzen. Your guidance during this semester has been immensely helpful and I am thankful for the scheduling of regular weekly meetings. These meetings have relieved a lot of stress and helped me get a better understanding of the results, and guided me in the right direction. I would also like to thank you for answering on short notice and always being available for questions and guidance. I would also like to thank my lovely bioceramic group for the weekly meetings that included great academic discussions, and also some cake and coffee. The broader FACET group has given me great insight into all the interesting research being conducted in materials science at NTNU and also hosted fun social events. Thank you to the wonderful staff at NTNU that have been giving me training for the different characterization methods. A special thanks to Dennis Meier's research group, and especially Ivan Ushakov and Leonie Richarz for facilitating and conducting the PFM results on my samples. The Research Council of Norway is acknowledged for the support to the Norwegian Micro- and Nano-Fabrication Facility, NorFab, project number 295864. Lastly, I want to give a huge thanks to my classmates, for their continued support, without you guys, this would not have been possible. We have made friendships that will last forever and I am certain that you will continue to be important in my future.

List of Figures

List of Tables

Contents

1 Introduction

The use of ceramics in joint replacement has been ongoing since the 1970s and ceramics were predicted to play a major role as orthopedic implant materials, due to their great chemical stability and biocompatibility [2]. Today, 50 years later, over 2.5 million knee and hip replacements are conducted annually [3], with bioceramics being an essential part of almost all implants. This number is set to increase as life expectancy is predicted to keep increasing [4]. A larger part of the world's population also experiences an increased quality of life, which will lead to people getting a hip or knee replacement at a younger age. The revision burden on such replacements surgeries is around 10%, with the expected lifetime of the implants generally being 15-20 years [5, 6]. When younger people (under 60) make up a bigger part of the patient group, the total risk of revision surgery is set to increase due to more patients outliving the lifetime of the implant. This calls for the need for increased chemical and mechanical stability of knee and hip implants. Improved bioceramics with enhanced biocompatibility, hardness, and wear resistance are key to extending the lifetime and improving the functional properties of these implants.

Historically, the main goal of the 1st and 2nd generations of ceramic bone implants was to maintain the mechanical and physical properties of a natural bone. The ceramic implant was supposed to react as little as possible with the body, and the goal was to find materials being as close to bio-inert as possible. Further research has shown that a new generation of bioceramics is needed to enhance the properties of a ceramic bone implant [3]. It is not enough that the bioceramic can replace defective bone, but it should be able to interact with the body to increase the reliability and longevity of these implants [3]. The 3rd generation of bioceramics aims to use the functional properties of the material to actively assist in the healing of the bone implant. A bioactive ceramic will be engineered to positively interact with human tissue and cells. Barium titanate ($BaTiO_3$, BT) is a promising bioceramic that is being studied for the use in bone implants. The long-term cytotoxic effect of barium titanate is still not fully understood, and it might be too toxic compared to other ceramics such as potassium sodium niobate (KNN). Nevertheless, the extensive research on the material and its great functional properties make it a good model system for the study of bioceramic bone implants [7, 8].

Fukada and Yasuda confirmed the piezoelectric effect in natural bone in the 1950s, and it was later proven that this effect enhances cellular growth and differentiation and improves regeneration [7, 9]. Taking advantage of a piezoelectric material in a bone implant would mimic the natural stress-generated electric field and improve the healing. The piezoelectric properties of BT can be utilized as a functional property to actively assist in the bone growth and integration of the implant to the surrounding tissue, thus improving the lifetime of the implant and the well-being of the patient.

Therefore the aim of this master's thesis is to synthesize a bulk ceramic of barium titanate and study its chemical surface and electrical properties. Studying BT *in-vivo* can be difficult due to large ion loss, a harsh environment, and larger mechanical stresses compared to *in-vitro*. At the same time, an *in-vivo* study should only be done if really necessary, due to the ethics related to an animal study, and the negative consequences for the animals. Therefore a simplified *in-vitro* study where the material is soaked either in ultrapure water (UPW) or simulated body fluid (SBF) was performed. A challenge during the implantation period is the dissolution of BT, which can lead to decreased healing function and reduced lifetime of the implant. The surface changes during soaking in UPW and SBF will indicate the chemical stability of the material. The material was also poled to different states before soaking, to study the effect on the domain structure. By poling the material the goal is to increase the surface charge and enhance the piezoelectric effect which is predicted to lead to increased calcium apatite precipitation during soaking in a body fluid [10]. The precipitation of calcium apatite works as an indication of the biocompatibility of the material.

Barium titanate was synthesized through a solid-state synthesis route. The chemical surface properties of the material were studied before and after soaking using different surface characterization techniques, such as scanning electron microscope (SEM), energy dispersive spectroscopy (EDS), and surface roughness measurements using an optical microscope. The piezoelectric properties of the material were measured both before and after soaking, to make sure that the functional property was upheld after soaking. Finally, the domain structures of the unpoled and poled samples were measured before and after soaking using piezoelectric force microscopy (PFM).

2 Theory

2.1 Piezoelectricity and ferroelectricity

With a growing demand for joint replacement at a younger age, in addition to patients wanting to be more active, the need for a new biomaterial implant is urgent. A class of materials that is of considerable interest in increasing the lifetime and reducing the rehabilitation time of joint replacements, is piezoelectrics. When applying mechanical stress to a piezoelectric material, an electric field is generated. This effect is known as the direct piezoelectric effect and was discovered by the Curie brothers in 1880 [11]. In the reverse version, known as the converse piezoelectric effect, an electric field creates a deformation and mechanical strain in the material. Both effects are illustrated in Figure 2.1.

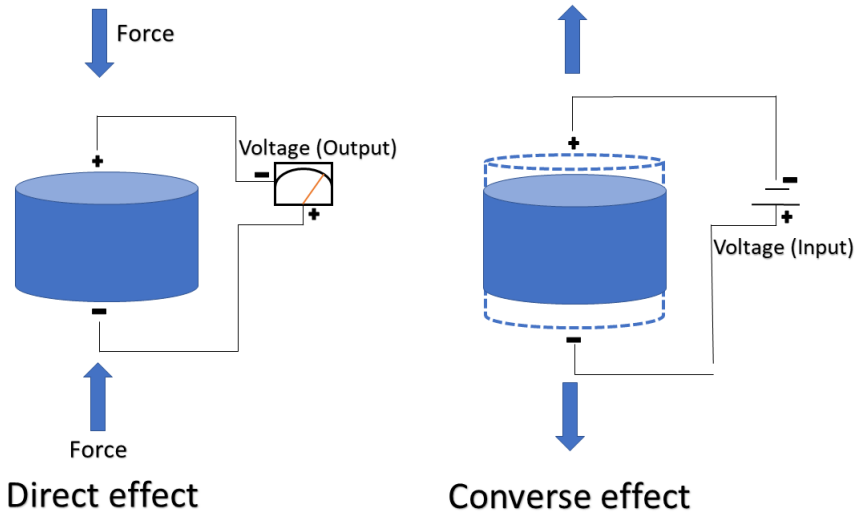

Figure 2.1: Illustration of the direct and converse piezoelectric effect. The figure is obtained from [1] with permission.

A material is classified as a piezoelectric only when certain requirements are fulfilled, and the main one is that the unit cell of a piezoelectric material has to be non-centrosymmetric. A subset of piezoelectrics is ferroelectric materials. These materials are also non-centrosymmetric, but in addition, they have one or more unique polar axes [12]. Alignment of the polar axes creates a spontaneous and reversible polarization in the material, which means that a ferroelectric material has polarization without any external stimulus and that the polarization can be switched by an electric field [11]. Figure 2.2 shows the grouping of the electric materials. Pyroelectrics are a subgroup of piezoelectrics and create an electric field in response to a temperature change, instead of a mechanical stress.

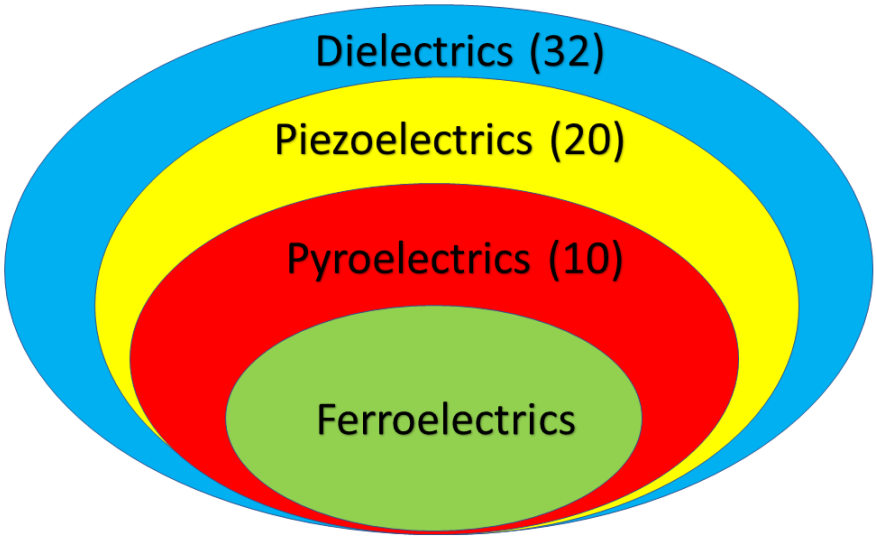

Figure 2.2: The figure shows the grouping of the electric materials. The number in the parentheses shows the amount of point groups that are represented by each class of electric materials. The figure is obtained from [1].

A ferroelectric material only exhibits the properties described above, in a certain temperature range. This range is delimited by a material-specific temperature known as the ferroelectric Curie temperature, T_C. At this temperature, the material experiences a phase transition [13]. In general, a material goes through a phase transition from a higher symmetry to a lower symmetry when decreasing the temperature past T_C. Using $BaTiO_3$ as an example, the material will go from a cubic unit cell to a tetragonal unit cell, and this creates non-centrosymmetry [14].

The properties of a ferroelectric material under T_C are characterized and described by a hysteresis loop, as seen in Figure 2.3 [14]. The hysteresis loop shows the correlation between an external electric field and the polarization of the material. For a bulk ferroelectric material, each domain will have a random polarization orientation which creates a net-zero polarization. This is seen in Figure 2.3 as point O. A domain is a region in the material with the same polarization direction, and is further described in section 2.8. When an external electric field is applied the domains align polarization directions and this creates a net polarization (Point A). At point B the curve starts flatting out before reaching a saturation polarization, P_S, at point C. When the external electric field is shut down, some of the domains will back-switch, but the material is still left with a remnant polarization, P_r (point D). When applying an electric field in the opposite direction the polarization decreases and at point F the polarization reaches zero, and the negative electric field applied is called the negative coercive field, E_C. A negative electric field is continued to be applied until the negative P_S is reached at point G. The electric field is

then switched and negative P_r is achieved at point H, while a positive electric field E_C has to be applied to get the ferroelectric material back to a net-zero polarization state. For an ideal ferroelectric material, the absolute value of the negative and positive P_S, P_r, and E_C values are equal.

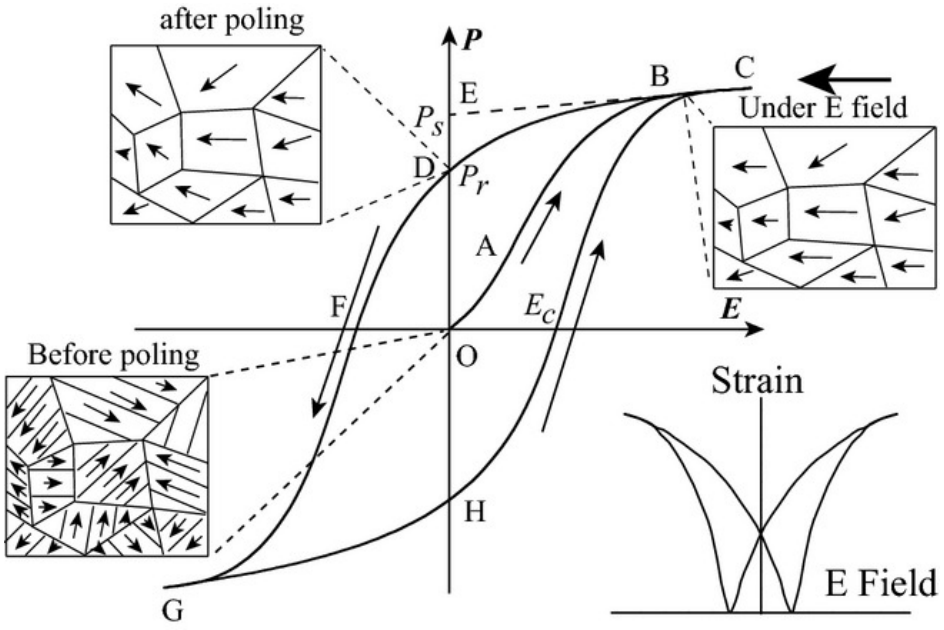

Figure 2.3: The figure shows an illustration of a hysteresis loop for a general ferroelectric material. Each letter describes an important point on the graph, which is explained in detail in the text above. The figure is gathered from a research article from 2014, written by Li Jin, Fei Li, and Shujun Zhang [14].

2.1.1 Applications

The direct and converse piezoelectric effect is taken advantage of for a lot of different applications in society. The use of piezoelectrics in an automotive is substantial, both for different types of sensors, such as tire sensors and knock sensors, but also for fuel injectors in the form of actuators [15]. The sensors take advantage of the direct piezoelectric effect when a mechanical strain creates an electric field signal. An actuator uses the converse effect, when an electric signal is applied to a fuel injector the piezo crystal changes shape and precisely and quickly delivers fuel to the engine [15]. Piezoelectrics can also be used for other applications such as energy harvesting [16]. Attaching a piezoelectric material to tires, shoes, or other applications that experience mechanical vibration could create a micro energy harvester. Microphones, speakers, and other acoustic devices also take advantage of the piezoelectric effect [17]. Piezoelectric materials have also been used in the field of medicine, for biosensors or medical ultrasound, but using piezoelectrics in new medical applications such as bone implants have yet to be fully utilized. The latest years have seen a remarkable interest in the use of piezoelectrics as biomaterials.

2.2 Biomaterials

Biomaterials are defined in many different ways, but overall they are defined as materials used to replace a part or a function of the body. The biomaterial is used to create a device, that is implemented in the body in a safe, reliable, economical, and physiologically acceptable way [18]. It is important to understand the difference between biomaterials and biological materials. Biological materials are per definition materials of biological origin, for example, wood. Biomaterials are, on the other hand, materials used in intimate contact with living tissue [18] for the context of medical applications. For a biomaterial to be effective, the functional, chemical, and mechanical properties are all crucial. For a piezoelectric bone implant, the functional property of electrical stimuli is of main importance. At the same time, a weakness in the mechanical properties could have a negative impact on the functional property of the implant. A biomaterial is often implemented into the body through surgery, and a long lifetime of the device is therefore crucial. The lifetime of the biomaterial is affected by how it is accepted by the tissue, how it reacts chemically to the tissue, and the material degradation. The way the body responds to a biomaterial, and also how the biomaterial affects the body is described through the term biocompatibility [18].

2.2.1 Biocompatbility

The most important criterion for a biomaterial is to be biocompatible. There are strict regulations that must be met for a material to be approved for use as a medical application, some of which are biocompatibility tests [18]. A biocompatible material is accepted by the body, chemically stable, and non-toxic. Ceramics have a high hardness and wear resistance, which reduces the likelihood of releasing particles in the body [19]. Ceramic materials tend to not cause allergic reactions and also have high corrosion resistance in comparison to metals [18]. Even though a material is biocompatible, it does not mean it is bioinert [20]. A bioinert material will from definition have no reaction with the body, but this is in reality almost impossible, as described by Williams in 1999 [21]. However, the reaction between the host tissue and the biomaterial can in some cases be utilized for the healing of the body. Ceramic materials that react with the body in a functional way are known as 3rd generation bioceramics. The different generations of bioceramics are further discussed in section 2.4. A piezoelectric implant could react with the tissue through an electric field and assist with the healing of the bone and increase bone formation.

2.3 Bone and bone healing

Understanding the general structure of bone is important when wanting to improve bone formation using a bioceramic implant. The structure of bone is complex and it consists of an inorganic phase embedded in an organic matrix. The inorganic phase is mainly calcium phosphate (apatite, CaP), while the organic matrix is highly oriented collagen fibers [9]. The weight ratio of apatite and collagen varies for different bones in the body, but in general, dry bone consists of 65-70 weight% apatite and 30-35 weight% collagen [22]. The two main types of bone structure are compact bone and cancellous bone. Compact bone is dense and usually forms the outer layer, while cancellous bone is more spongy and makes up the inner layer. Different types of bone in the body will have a varying ratio of the two bone structures, because of the different properties needed. A larger bone that has to handle a more substantial mechanical load, will therefore need more of the dense compact bone structure [23]. Bone does not only consist of apatite and collagen, but cells are also an important part. There are four main different bone cell types: osteoblasts, osteoclasts, osteocytes, and bone-lining cells [23]. These cells all play a crucial role in the healing and remodeling of bone.

The exact mechanism of bone growth and healing is not fully established, but there are some main theories revolving around the healing effect of osteoblasts. These cells are responsible for the formation of bone through the synthesis of osteoid. Osteoid mainly consists of collagen, and the osteoid is later mineralized, through the deposition of hydroxyapatite (HA), to form the inorganic phase [23]. One of the leading theories describes how piezoelectricity creates an electric field attracting the osteoblasts to the bone [24]. When mechanical stress is applied to a bone the piezoelectric effect of the highly oriented collagen fibers results in an electric polarization attracting the osteoblasts. Even though the theory revolving around piezoelectricity and healing of bone is not fully established, the presence of piezoelectricity of bone was proven already in the 1950s [9].

Fukada and Yasuda confirmed the piezoelectric effect of bone, but it only appeared when a shearing force made the collagen fibers slip past each other [9]. The effect measured was small and the d_{11} piezoelectric coefficient maximum value reported was $6 \cdot 10^{-9}$c.g.s. e.s.u., amounting to around one-tenth of the coefficient for quartz [9]. This piezoelectric effect was later related to the healing of bone and in 1988 it was confirmed by Davies that surface charges affect cell migration and protein adhesion [25]. A piezoelectric implant material can therefore mimic the stress-generated electrical potential in bone and increase the cellular growth and differentiation [7]. The use of such a material as a bone implant in orthopedics is thus clear.

2.4 Ceramics in orthopedics

Orthopedic surgery is a reconstructive surgery involving the use of prosthetic biomaterials to replace or repair damaged musculoskeletal tissue to restore function or relieve pain [3]. The improvement of biomaterials and anesthesia, together with the increased focus on sterility made orthopedic surgeries practical in the 1900s. In the late 20th century and in the 21st century, ceramics have been used successfully for different orthopedic applications, especially for prostheses. Ceramic prostheses need sufficient mechanical and functional properties, and ceramics are favorable, due to generally having great biocompatibility, strength, hardness, and corrosion and wear resistance [3].

The stability and biological reactivity of ceramics in orthopedics are crucial for increasing the lifetime of the materials. As described in section 2.2.1 no material is truly bioinert. This is further described by Pezzoti, who explains that even though the bulk of the material may not change, the surface reacts with the biological environment to some extent [20]. Therefore it is important to study these reactions and find ceramics that have high hydrothermal and chemical stability. A small change in the surface chemistry of a ceramic could make the material go from being bio-friendly to being rejected by the body, leading to inflammation and fibrous encapsulation [3]. The testing of ceramics for orthopedics is performed *in-vitro* and *in-vivo*. *In-vitro* tests are used to study the chemical stability and biocompatibility of the ceramic, but it usually do not account for mechanical loading or stress which could lead to some challenges in getting reliable data before proceeding to *in-vivo* tests.

2.4.1 Generations of bone implants

The first two generations of bone implants focused on mechanical properties and the material being bio-inert or bio-tolerant [3]. However, the third generation of bioceramics also focuses on effectively integrating with the host tissue. It is not enough that the ceramic is biocompatible, it also needs to be bioactive. This means that the material can interact with the tissue in a functional way, for example by inducing bone formation. As explained earlier, one type of these smart biomaterials is piezoelectric materials, and barium titanate (BT) is one of these promising materials.

2.5 Barium titanate and lead-free piezoelectrics

Barium titanate was the first polycrystalline ferroelectric ceramic discovered, however, it did not take long before it got challenged and outperformed by another material, lead zirconate titanate (PZT). PZT has a higher Curie temperature and more tunable piezoelectric properties than barium titanate. Therefore it was not before the start of the 2000s that the interest in BT as a piezoelectric started rising again, due to the increased focus on lead-free piezoelectrics [7].

In 2003, the EU passed a legislature that declared PZT as a hazardous substance and put a spotlight on trying to substitute PZT with safer materials [26]. Lead is a well-known toxic element that can cause serious health issues, such as having neurotoxic properties. Lead is further classified as a possible human carcinogen while lead compounds are classified as probable human carcinogens [27]. This raises the question about environmental, social, and governance (ESG) risks when producing and utilizing lead piezoelectrics. Today, PZT is still the most used piezoelectric, and the ESG risks for the workers producing PZT are therefore still present. Even though the EU legislature from 2003 made PZT a hazardous material, there are still technical and scientific challenges in substituting PZT in all areas of society, but as a piezoelectric biomaterial, it is certain that PZT can not be used. Therefore research is being conducted on BT as a model system for lead-free piezoelectrics, in the use of medical applications. Even though BT is claimed to be biocompatible, there are still some discussions on the long-term cytotoxicity of BT [7]. Some studies have shown the leaching of Ba^{2+}-ions from BT in biological fluids, and these ions can substitute out calcium (Ca^{2+}) ions from the bone, but no detrimental effects on the bone have yet to be observed [7].

Barium titanate is a perovskite with the general formula ABO_3. In BT, Ba^{2+} is located on the A-site in the corners, while Ti^{4+} is placed at the B-site in the center of the cell and O^{2-} is located at the face center of the unit cell on the C-site [7]. During cooling through the Curie temperature the unit cell transitions from a simple cubic ($Pm\bar{3}m$) to a tetragonal unit cell ($P4mm$). These two unit cells of barium titanate are presented in Figure 2.4 and an off-set of the Ti^{4+}-ion from the center creates a spontaneous polarization for the tetragonal unit cell. The non-centrosymmetry of the $P4mm$ structure makes barium titanate piezoelectric. Perovskites are usually great piezoelectrics and are well-researched, due to their normally lower costs and simple crystal structure compared to more complex piezoelectrics. The stability of perovskites is described by the Goldschmidt tolerance factor (t) given as:

$$t = \frac{R_A + R_X}{\sqrt{2} * (R_B + R_X)}, \tag{2.1}$$

where R_A is the radius of the A cation, R_B is the radius of the B cation and R_X is the X anion radius, which is the oxygen radius for most perovskites [28]. The relation explains how far

away from the ideal ionic radii, the ions in a perovskite can deviate, and still create a stable material. Victor Goldschmidt described this relationship in 1927 through experimental data and concluded that t = 0.8-1.0 makes a perovskite stable [28]. The theoretical tolerance factor of barium titanate is calculated to be 1.063 [29].

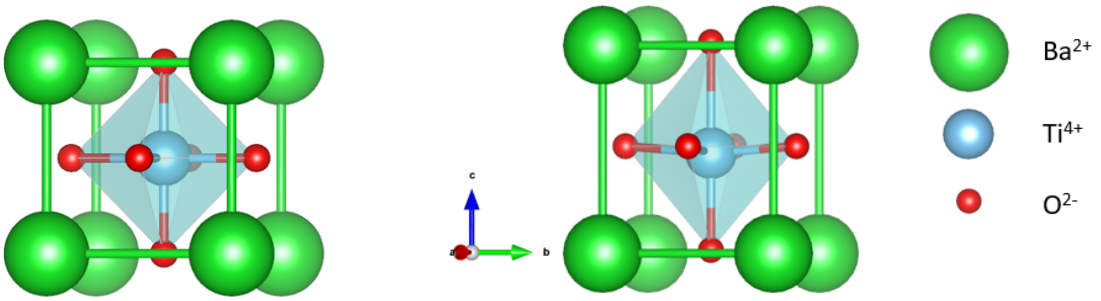

(a) Cubic unit cell (b) Tetragonal unit cell

Figure 2.4: The perovskite unit cell structure of $BaTiO_3$, both as the cubic unit cell (a) and the tetragonal unit cell (b). The figure is made using VESTA and is obtained from Holum (2022) [1]. The crystallographic data used for making the unit cells is given in Appendix A.

2.6 Dissolution

Even though barium titanate is a promising lead-free piezoelectric as a model system for bone implants, some challenges still remain. Achieving sufficient chemical stability is challenging, due to the ion dissolution of perovskites. In piezoelectric applications, a larger strain is often wanted. As explained using the Goldschmidt factor, varying ionic radii will increase the strain on the material and therefore reduce the stability [28]. This creates a paradox for piezoelectric applications. The piezoelectric coefficient, d_{33} explains the relationship between strain and electric field, and a larger strain on the material will result in a larger electric field as the output [30]. Therefore it is important for piezoelectric applications to balance the need for strain and stability. For the application of a bone implant, the need for chemical stability is crucial, due to the requirement of a long lifetime. A bone implant needs to be resistant to repetitive varying stresses over a long time. The implant will also be in contact with not only human tissue but also body fluid in motion. Biological body fluid, such as human blood plasma, contains different ions, where Na^+ and Cl^- are most dominant [31]. Ionic crystals that are in contact with a polar solvent will experience ion dissolution due to electrostatic forces.

The general mechanism of ion dissolution is explained using thermodynamics and it is based on Raoult's law (equation 2.2) and the general concept of energy reduction [32]:

$$(\frac{P_A}{P_A^0}) = x_A, \tag{2.2}$$

where P_A is the partial pressure of component A in the system, while P_A^0 is the standard partial pressure of A, and x_A is the mole fraction of A. Raoult's law explains how the partial pressure of A is equal to the standard potential of A times the mole fraction. In equilibrium, the chemical potential of A in liquid and gas needs to be equal:

$$\mu_A(g) = \mu_A(l), \tag{2.3}$$

where $\mu_A(g)$ is the chemical potential of A in gas and $\mu_A(l)$ is the chemical potential of A in liquid. The general law of chemical potential explains how to derive the chemical potential of A, using the standard chemical potential, $\mu_A^0(g)$, the gas constant (R), temperature (T[K]), and the partial pressure of A (P_A). This relation is given in equation 2.4:

$$\mu_A(l) = \mu_A^0(g) + RT * lnP_A. \tag{2.4}$$

When combining equation 2.2, 2.3 and 2.4, the general relation of the chemical potential of component A in the liquid is given:

$$\mu_A(l) = \mu_A^0(l) + RT * lnx_A, [32]. \tag{2.5}$$

This equation describes a relation between the chemical potential of a component in solution and in the standard phase. If the chemical potential of a component is lower in the solution, the dissolution is thermodynamically favored, due to the driving force of energy reduction.

For barium titanate, the dissolution in an aqueous media is most predominant through Ba^{2+} leaching, following reaction 2.6 [33].

$$BaTiO_3(s) + H_2O \leftrightarrow Ba_2{}^+(aq) + TiO_2 + 2\,OH^-. \tag{2.6}$$

Thermodynamic calculations have shown that a substantial amount of Ba^{2+} ions should be leached [33]. At a lower pH, following Le Chatelier's principle, the reaction equilibrium will be pushed further towards the right side, due to the limited amount of OH^- ions. Increased leaching of Ba^{2+} at lower pH has also been confirmed experimentally [33–35]. The other products created during leaching of Ba^{2+}, are TiO_2 and OH^-. This means that the pH in the system will increase during leaching, and the creation of TiO_2 will make an outer layer with excess Ti, that is barium-depleted $BaTiO_3$ [34]. This outer layer could have an impact on both the electrical and mechanical properties of BT when used as a bone implant.

2.7 CaP precipitation

The use of simulated body fluid (SBF), is crucial when performing *in-vitro* studies on the dissolution of BT. Simulated body fluid has ion concentrations nearly equal to the human blood plasma, and can be used to study both the ion dissolution of BT, but also the apatite formation. Almost all materials form apatite to bond to living bone, and apatite formation on an implant material is therefore crucial for the bioactivity of the material. SBF has proven to be able to predict both qualitatively and quantitatively the *in-vivo* bioactivity of materials, which could be helpful to reduce to use of animal testing [31].

Understanding the connection between apatite formation in SBF and *in-vivo* is important in the application of bone implants. As explained, research shows a correlation between CaP precipitation in SBF and the *in-vivo* bone bioactivity of a material [31]. Section 2.3 explained that the main inorganic constituent in bone is apatite. An increase in the apatite formation will therefore likely promote bone ingrowth, but how can a material be optimized to increase apatite formation [36]?

As explained, the idea behind a piezoelectric bone implant is to mimic the natural generation of an electric field during mechanical stress on the bone. It is believed that an electric field generated by the implant could attract Ca^{2+} and Mg^{2+} ions to the surface of the material and promote apatite formation [8]. If the material used as a bone implant could induce an electric field the apatite formation is increased. An as-sintered piezoelectric ceramic has randomly oriented domains, but by poling the material the polarization orientation will align. The alignment of dipoles will create a larger surface charge on the material. A poled piezoelectric material undergoing mechanical stress will induce a larger electric field, which is then predicted to increase apatite formation. Poling a piezoelectric ceramic could therefore create larger domains that again will increase the biocompatibility of the material.

2.8 Domains and poling

A polycrystalline ferroelectric ceramic material will have a net-zero polarization, even though the material has a reversible and spontaneous polarization. The reason for this is due to the polarization direction in different domains canceling out. Domains are regions in a material that has the same polarization direction. In a polycrystalline material, these domains are formed in a random arrangement with different polarization directions and strengths. The polarization strength is mostly determined by spontaneous polarization but altered by local boundary conditions such as grain boundaries and accumulated charges. The polarization cancels out and this random arrangement makes the bulk material have a net-zero polarization [23]. Domains are created due to the lowering of energy. When regions with different polarization directions

are created, the electrostatic energy decreases. The boundaries between domains are known as domain walls and are always present when domains are created. The interface energy of domain walls increases the total internal energy, but as long the electrostatic energy has a larger negative contribution, the creation of domains is favored. When the decrease of electrostatic energy is equal to the increase of domain wall energy, an equilibrium domain state is obtained [37].

As explained in section 2.5, $BaTiO_3$ has a stable tetragonal unit cell, and an off-set of the Ti^{4+} from the center creates a spontaneous polarization. This spontaneous polarization is in the [001] direction, as shown by studying the tetragonal unit cell in Figure 2.4. This is why d_{33} is the mainly used piezoelectric coefficient for perovskites, due to it describing the piezoelectric response in this direction. This [001] polarization can be in any of the six cubic directions, $\langle 001 \rangle$, leading to tetragonal ferroelectrics having six domain states [38]. Some of these domain states are structurally distorted and the neighboring polarization is rotated by 90°. The domain walls separating these domains are known as 90° domain walls, and the pattern it creates is called the herringbone pattern. The polar axis of neighboring domains can also be oriented by 180° and they are separated by 180° domain walls, resulting in a stripe formation [38]. Both of these general domain patterns are illustrated in Figure 2.5.

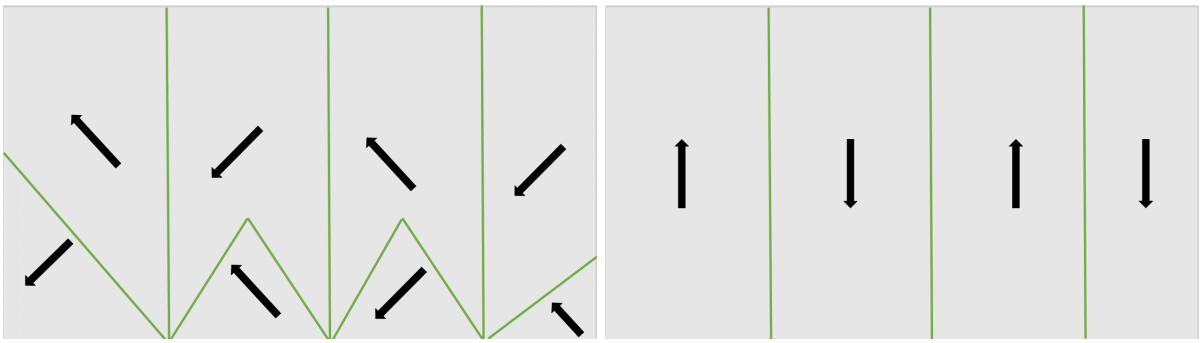

(a) Herringbone pattern with 90° domain walls. (b) Stripe formation with 180° domain walls.

Figure 2.5: Illustration of the general domain patterns with 90° (a) and 180° (b) domain walls. The polarization direction is presented by the black arrows, while the green lines are the domain walls.

Poling

By poling the material, and applying a high electric field at a temperature under T_C the domains are oriented [23]. Poling of a ferroelectric material can create new domains, together with the increase or shrinkage of already existing domains. The domains with a polarization direction already aligned with the electric field will increase in size, while the other domains will shrink [39]. The effect of poling on the domain structure of a general ferroelectric material is shown in Figure 2.6. The same electrical field is applied for the semi-poled and the poled sample, but the poling time is longer for the poled sample. When removing the electrical field the sample is

left with a remnant field, P_r. The strength of the remnant polarization is dependent on available domain states [40]. If only two domain states are possible for the ferroelectric material the $P_r = 0.26P_S$, where P_S is the saturation polarization, as explained in section 2.1. As explained in the previous paragraph, a tetragonal ferroelectric material can have six domain states. This leads to $P_r(max) = 0.83P_S$ [40]. These are the theoretical values, but the actual values are lower, due to some domains not being able to reorient due to internal stresses, and also some domains flipping back after removing the poling [40].

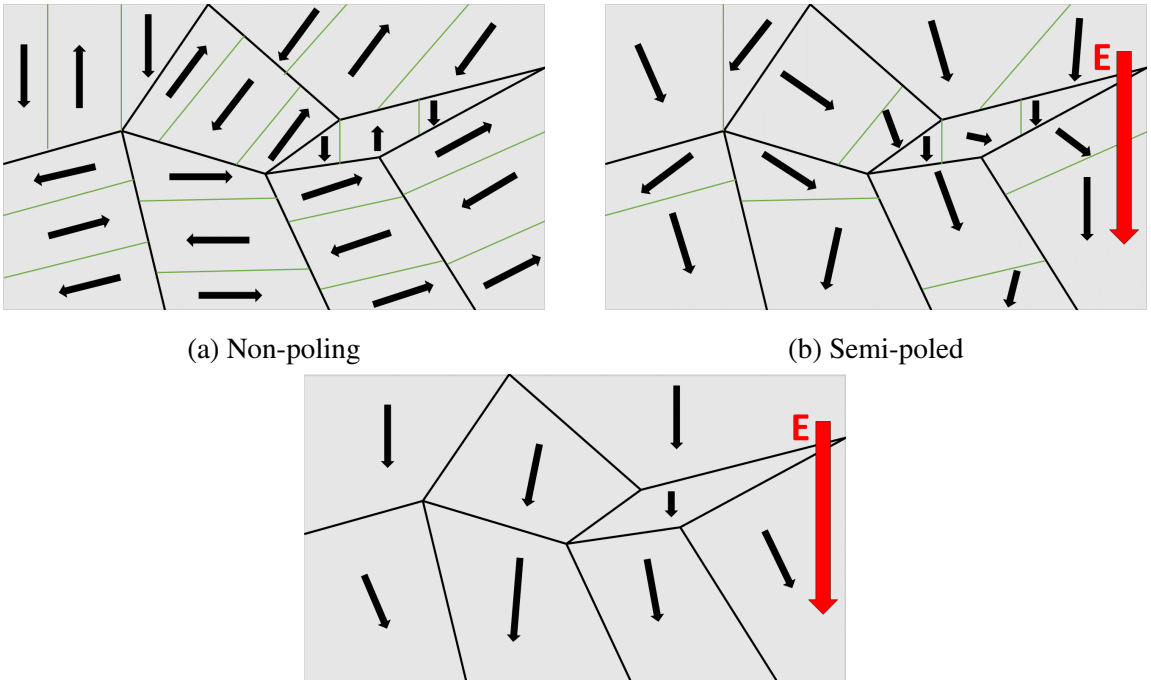

(a) Non-poling

(b) Semi-poled

(c) Poled

Figure 2.6: Illustration of general ferroelectric domains before and after poling for different states. The red arrow shows the electric field direction, while the black arrows show the polarization direction of each domain. The thicker black lines represent the grain boundaries while the thinner green lines are the domain walls.

2.9 Piezoresponse force microscopy (PFM)

To study the domain patterns explained in section 2.8, piezoresponse force microscopy can be used. This is a surface characterization technique utilizing both the direct and converse piezoelectric effect [41]. These effects are described in detail in section 2.1. PFM is a modified technique of atomic force microscopy (AFM). AFM functions by measuring the force between a tip and the sample, by using the deflection of a cantilever. If the stiffness of the cantilever is known, the force can be calculated by measuring the bending of the cantilever using a reflected laser beam [42]. By having a ferroelectric sample and applying an AC electric field through the tip while in contact with the sample, the AFM is modified into PFM. The alternating field will deform the sample due to the converse piezoelectric effect. Due to the alternating applied electric field, the sample will deform periodically. The direct piezoelectric effect will make the ferroelectric sample induce an electric field local to the mechanical deformation [41]. The strength of this measured electric field is known as PFM amplitude, while the electric phase shift between the applied and induced electric field is known as the PFM phase. If the polarization direction of the domain is parallel to the applied electric field the sample will oscillate in-phase, and for anti-parallel polarization direction, the oscillation happens out-of-phase [43]. This phase difference and a change in the PFM amplitude for different areas of the sample are used to differentiate the different domains from each other.

In an unpoled bulk ferroelectric material, there are both in-plane and out-of-plane polarization due to the random polarization orientations. When an alternating current is applied the compression/extension of the sample will lead to a vertical displacement of the cantilever, while a shear strain in the sample leads to torsion or buckling of the cantilever [41, 44]. This cantilever movement is shown in Figure 2.7. The vertical displacement is analyzed using vertical PFM and explains the out-of-plane domains, while the torsion is analyzed using lateral PFM and explains the in-plane domains. As can be seen in Figure 2.7, the in-plane polarization also leads to buckling, but this signal is analyzed by vertical PFM. The vertical deflection of the cantilever and the buckling will both give a vertical signal which can be difficult to distinguish. By rotating the sample 180° the deflection signal will not change while the buckling signal leads to an inversion in the PFM contrast. This is important to keep in mind, and can be a common source of error when analyzing PFM images [44].

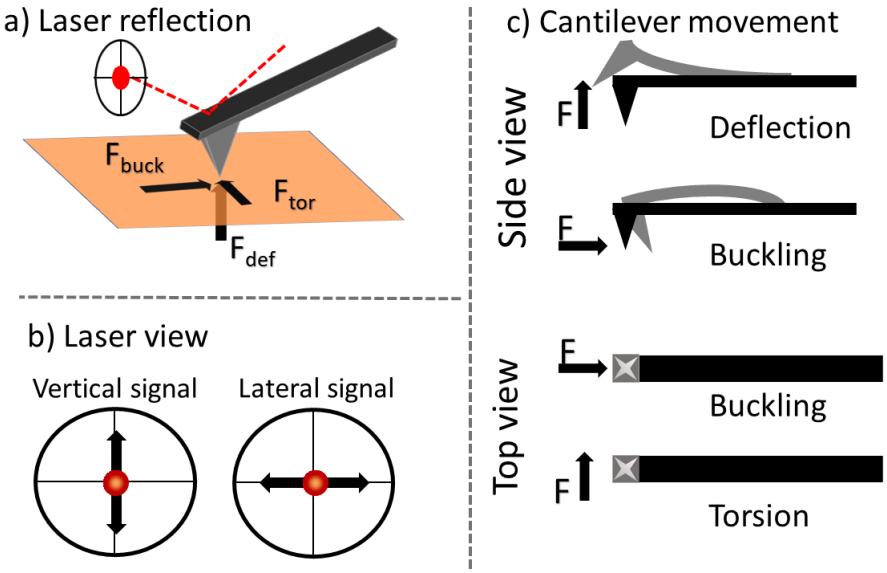

Figure 2.7: This figure is recreated based on an article from 2011 by Elisabeth Soergel [44]. a) shows the PFM cantilever and the laser reflection, together with the forces affecting the cantilever both in-plane and out-of-plane. b) shows the laser signal in the vertical and lateral directions. c) presents the cantilever movement that is analyzed in the vertical direction: deflection and buckling, and in the lateral direction: torsion.

2.10 Solid-state synthesis

One of the most common ways to synthesize ceramic materials is through the solid-state synthesis method. An illustration of this process is given in Figure 2.9 at the end of the section. In this method, powders of the precursors are reacting during heating and create the final product. For the synthesis of barium titanate, the solid-state reaction is given as [45]:

$$BaCO_3(s) + TiO_2(s) \rightarrow BaTiO_3(s) + CO_2(g). \tag{2.7}$$

To achieve optimal properties of a ceramic material it is important to control the particle size and particle size distribution. This can be done through different mechanical and chemical techniques. One of the most common mechanical powder preparation techniques is ball milling [46].

2.10.1 Ball milling

Ball milling is a particle size reduction step, that usually produces a broad particle size distribution. Therefore, sieving is usually performed after milling. The powder is placed in a milling jar together with grinding media (milling balls) before the milling jar is rotated. During rotation, the powder is crushed into smaller particles by moving between the milling balls and the milling jar walls [46]. A simple illustration of planetary ball milling is shown in Figure 2.8. A

common problem in milling is contamination. The wear of the milling jar walls and the grinding media will introduce foreign particles into the powder. Choosing a milling media and a jar with higher hardness and wear resistance will reduce contamination in the powder. Controlling the milling time is also crucial. It is important to find an optimal milling time where there is a balance between wanted particle size and low impurities. Ball milling can be performed either by wet milling or dry milling. An obvious advantage of dry milling over wet milling is that the resulting powder does not have to be removed from a liquid. On the other hand, wet milling has the advantages of good homogenization and smaller particles [46]. It is important to achieve free-flowing powder during milling, and this is obtained easier for wet milling than dry milling. To increase the density of the green body after pressing, a lubricant can be added as a milling aid [46].

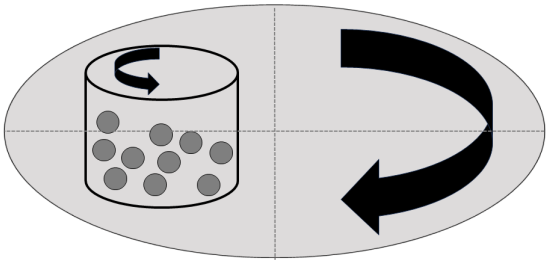

Figure 2.8: Simple illustration of planetary ball milling.

2.10.2 Shape forming

Shape forming of ceramic materials can be performed by pressing. The prepared powder is put in a die together with additives, before being pressed, either uniaxially or isostatically. Uniaxial pressing is a simple method where the pressure is applied along a single axis. Applying pressure only along a single axis creates some problems. The most common problems after uniaxial pressing are nonuniform density and cracking [46]. Density variation in the green body, together with die wear could lead to cracking of the sample. By using additives such as lubricants and binders, these problems can be reduced or avoided. Lubricants will minimize die-wall friction and friction between the particles, making the particles free-flowing. The binder will mechanically strengthen the green body, making it able to handle the shape-forming process before sintering [46]. To solve some of the challenges with uniaxial pressing, isostatic pressing can be used. The pressure is applied in all directions and this removes the problem with density gradients seen in uniaxial pressing. The limitations of simple shapes in uniaxial pressing are also removed for isostatic pressing. The downsides of isostatic pressing when compared to

uniaxial pressing, are more expensive equipment and batch process [46].

2.10.3 Heat treatment

Calcination

The first heat treatment step in a ceramic synthesis route is usually calcination. Calcination is the main chemical reaction step and is a high-temperature treatment of a powder to improve its characteristics and prepare the powder for shape forming and sintering. This can result in coarsening, decomposition, reaction, and dehydration of the ceramic powder. Coarsening is a non-densifying mechanism where the mass is transported from the surface of the particles that leads to microstructural change without any shrinkage [46]. During calcination, precursors are reacting to create the final product. It is therefore important to keep a high enough temperature for the reaction to take place and a long enough holding time to make sure that all precursors have reacted.

Sintering

Sintering is the next and generally final heat treatment step in a solid-state synthesis. Sintering is a densification step, where the pores are removed and the particles are growing and bonding together. One of the main material transport mechanisms for sintering is diffusion, and these criteria need to be met for sintering to occur [46]:

- A mechanism for sintering must be present
- A source of energy to activate and sustain material transport.

The main source of energy to activate and sustain material transport is generally heat. The sintering process is divided into three different stages. In the initial stage, the particles are rearranged and necks are formed at the contact point between the particles. The densification in this step is limited and a theoretical density of around 60-65% is reached [46]. In the second stage of sintering the necks are growing and the center of the particles (grains) move closer together. The grain boundaries start to move, and the smaller grains are consumed by larger ones. This intermediate stage has the highest amount of shrinkage [46]. In the third and final stage of sintering the pores located at the grain boundaries are removed. If the grain growth is happening too quickly the boundaries move quicker than the pores, which leaves the pores left inside a grain. These isolated pores are very difficult to remove, and controlled grain growth is, therefore, crucial to minimize porosity. The main driving force through all these different stages of sintering is a reduction of the surface energy [46].

The diffusion of mass to decrease surface energy can happen through different mechanisms. If the mass transport is happening from the surface to either the lattice or the surface, microstructural changes will occur without shrinkage of the material. This is known as a coarsening mech-

anism, as explained in the subsection above. One of the goals of sintering is densification and this occurs by diffusion of material from the grain boundaries to either the grain boundary or the lattice [46].

By controlling the particle size and temperature the rate of sintering can be decided. An increase in temperature will generally increase the diffusion coefficient and the rate of material transport. This would again lead to an increase in grain growth. It is therefore important to reach a high enough sintering temperature for increased diffusion, but not reach a too high temperature which could lead to exaggerated grain growth and increased porosity. A smaller particle size increases the surface area and therefore increases the surface energy, which is as mentioned, the main driving force of sintering. Having a broad particle size distribution could increase the packing efficiency and decrease porosity. By controlling and changing the particle size and temperature the optimal microstructure of a ceramic could be obtained through sintering.

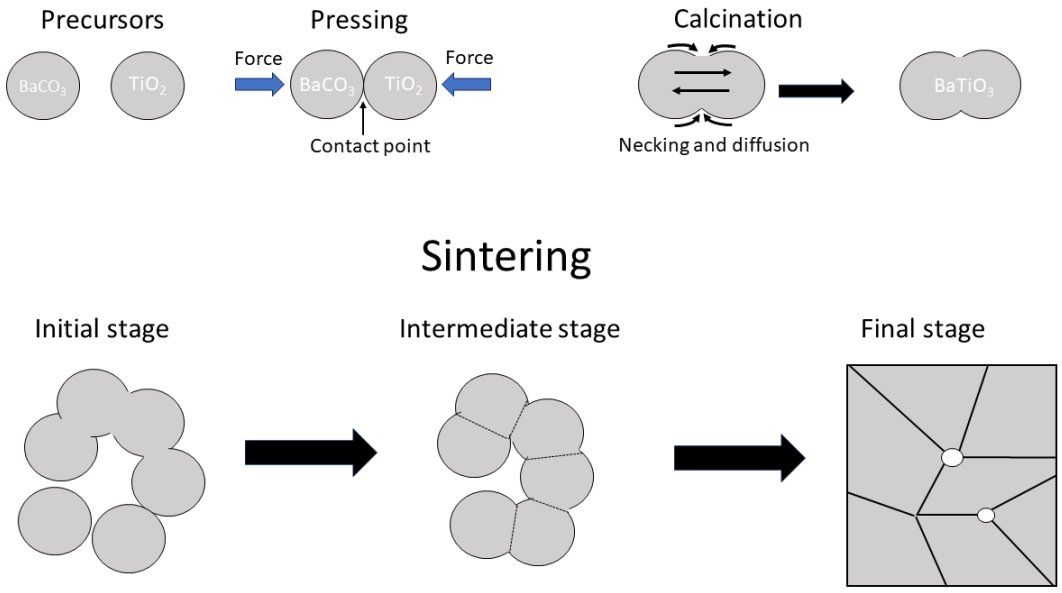

Figure 2.9: Solid-state synthesis method. The precursors are pressed together before a calcination step is performed, where $BaTiO_3$ is synthesized. In the sintering steps, the particles rearrange and necks are formed before grain boundaries and grains are created. In the final stage of sintering, there may be some trapped pores left in the microstructure, seen as white circles.

3 Materials and Methods

3.1 Processing/Synthesis

The synthesis and characterization of barium titanate are based on experiments by Holum from 2022 [1] but with some changes and improvements. A flowchart showing the different steps of the solid-state synthesis of $BaTiO_3$ is presented in Figure 3.1. In total three calcined powder batches (Batch1, Batch2, Batch3) were synthesized, and from these powders, six pellet batches were sintered (BT01, BT02, BT03, BT04, BT05, BT06). An overview of the powder and pellet batches is given in Table 3.1. The calcination and sintering parameters were the same for all the batches, but some of the equipment used in the synthesis of Batch1 was swapped out when synthesizing Batch2 and Batch3, to reduce the probability of contamination. The agate pestle and mortar, and the 250 µm sieve were replaced with different ones, while a ZrO_2 milling jar was changed to a Teflon (polytetrafluoroethylene, PTFE) milling jar. Table 3.2 shows the parameters used when synthesizing the different batches of $BaTiO_3$ for this project, and also for the project by Holum (2022) [1]. After synthesizing the powder and preparing the bulk material in the shape of pellets, the material was characterized as explained in detail in section 3.2. Table 3.3 gives an overview of the different characterization methods and treatments performed on each sample.

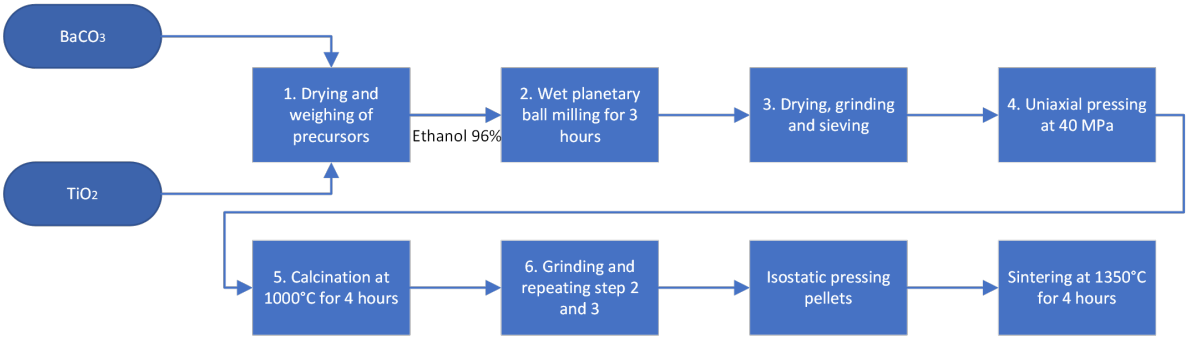

Figure 3.1: A flowchart describing the solid-state synthesis of $BaTiO_3$

Table 3.1: An overview of which powder batches produced which pellet batches.

Powder batch #	Pellet batch # [g]
Batch1	BT01
Batch2	BT02, BT03
Batch3	BT04,BT05,BT06

Table 3.2: An overview of the different batches. The only difference between Batch1, in comparison to Batch2 and Batch3, is the change of the milling jar. An improvement to increase the sintering temperature with 50 °C has been made for Batch1, Batch2, and Batch3 in comparison to the last project.

Batch #	Mass pellets [g]	Calcination parameters	Sintering parameters	Polishing media	Milling jar
Holum (2022)[1]	0.35	1050 °C, 4h	1300 °C, 4h	100% ethanol	ZrO_2
Batch1	0.35	1000 °C, 4h	1350 °C, 4h	100% ethanol	ZrO_2
Batch2	0.35	1000 °C, 4h	1350 °C, 4h	100% ethanol	Teflon
Batch3	0.35	1000 °C, 4h	1350 °C, 4h	100% ethanol	Teflon

Table 3.3: An overview of all the BT samples synthesized and the different measurements and treatments done on each pellet. The pellet ID is BT0ApB, where A is the number of the pellet batch and B is the number of the pellet in each batch.

Pellet ID	Treatments	Measurements
BT01p1	Thermal etch, polishing, poling	SEM, Archimedes, Piezo
BT01p2	Thermal etch, polishing, soaking	SEM
BT01p3	Polishing, poling	XRD, Archimedes, Piezo
BT01p4	Thermal etch, polishing	SEM
BT01p5	Thermal etch, polishing	SEM
BT01p6	Polishing	XRD
BT02p1	Thermal etch, polishing, soaking	XRD, SEM, Archimedes, Surface roughness
BT02p2	Thermal etch, polishing	SEM
BT02p3	Thermal etch, polishing	SEM
BT02p4	Polishing, poling, soaking	Archimedes, Surface roughness
BT02p5	Polishing, poling, soaking	Surface roughness
BT02p6	Polishing, poling, soaking	Surface roughness
BT03p1	Polishing (for PFM), soaking	PFM, Surface roughness
BT03p2	Polishing (for PFM), poling, soaking	PFM, Surface roughness
BT03p3	Polishing (for PFM), poling, soaking	PFM, Surface roughness
BT03p4	Polishing (for PFM), poling, soaking	PFM, Surface roughness
BT03p5	Thermal etch, polishing, soaking	XRD, SEM, Archimedes, Surface roughness, Piezo
BT03p6	Polishing, poling, soaking	Archimedes, Surface roughness
BT04p1	Thermal etch, polishing, soaking	XRD, SEM, Archimedes, Surface roughness, Piezo
BT04p2	Polishing, poling, soaking	Archimedes, Surface roughness
BT04p3	Polishing, poling, soaking	Surface roughness
BT04p4	Polishing, poling, soaking	Surface roughness
BT04p5	Polishing, poling, soaking	Surface roughness
BT04p6	Polishing, poling, soaking	Surface roughness
BT05p1	Thermal etch, polishing, soaking	SEM, Archimedes, Surface roughness
BT05p2	Polishing, poling, soaking	Archimedes, Surface roughness
BT05p3	Polishing, poling, soaking	Surface roughness
BT05p4	Polishing, poling, soaking	XRD, Surface roughness
BT05p5	Polishing, soaking	Surface roughness
BT05p6	Polishing, poling, soaking	Surface roughness
BT06p1	Polishing, poling, soaking	Surface roughness
BT06p2	Polishing, poling, soaking	Surface roughness
BT06p3	Polishing, poling	-
BT06p4	Polishing, poling	Piezo
BT06p5	Polishing, poling	-
BT06p6	Polishing, poling	-

3.1.1 Preparation of powder

Mixing of precursors

$BaCO_3$ and TiO_2 were used as precursors to synthesize $BaTiO_3$ in a solid-state synthesis process. The detailed info on the precursors is presented in Table 3.4. The precursors were prepared for ball milling by being dried overnight in a 120 °C heating cabinet. The stoichiometric weight of each precursor was then weighed out and the precursors were mixed and prepared for ball milling. The theoretical and experimental weight and moles for $BaCO_3$ and TiO_2 are given in Table 3.5, and the calculations are shown in Appendix B.

Table 3.4: Detailed information on the precursors used in the synthesis of $BaTiO_3$

Chemical	Supplier	Purity	LOT number
$BaCO_3$	Sigma-Aldrich	99.98 %	0000022734
TiO_2	Sigma-Aldrich	99.8 %	MKCD6078

Table 3.5: Theoretical and experimental values for the different batches synthesized of $BaTiO_3$

Batch#	Weight [g] and moles	$BaTiO_3$	$BaCO_3$	TiO_2
Batch1	Theoretical weight [g]	20.0	16.9251	6.8498
	Theoretical moles	0.0858	0.0858	0.0858
	Experimental weight [g]	14.7000	16.9256	6.8498
	Experimental moles	0.0630	0.0858	0.0858
Batch2	Theoretical weight [g]	14.0	11.8476	4.7949
	Theoretical moles	0.0600	0.0600	0.0600
	Experimental weight [g]	11.5600	11.8475	4.7939
	Experimental moles	0.0496	0.0600	0.0600
Batch3	Theoretical weight [g]	20.0	16.9251	6.8498
	Theoretical moles	0.0858	0.0858	0.0858
	Experimental weight [g]	18.0128	16.9252	6.8499
	Experimental moles	0.0772	0.0858	0.0858

Ball milling

Ball milling was performed on the precursors to reduce the particle size and increase the rate of reaction for calcination. For Batch1 the precursors were mixed in a 125 mL zirconia (ZrO_2) milling jar together with 96% ethanol. For Batch2 and Batch3 the milling jar was changed to a Teflon jar, as seen in Table 3.2. This was done to remove a likely source of contamination. Yttria-stabilized zirconia (YTZ) balls were used as the milling media, and the milling jar was

filled 2/3 full with YTZ balls. RETSCH PM100 planetary ball mill was used for the milling with a rotation speed of 150 rounds per minute (rpm). The milling time was set to 3 hours, to decrease the particle size enough without introducing too much contamination.

Drying, grinding and sieving

The slurry from the ball milling was dried using a Buchi rotavapor. The slurry was dried at 175 mPa in a water bath at 60 °C. After drying, a plastic spatula removed the powder from the beaker flask. The powder was ground using an agate pestle and mortar and sieved through a 250 µm sieve. Between Batch1 and Batch2 the agate pestle and mortar and the sieve were swapped out to reduce the likelihood of introducing contamination into the powder.

Uniaxial pressing of pellets

The sieved powder was then pressed in a uniaxial press. Before pressing the powder into pellets, stearic acid was applied to the die, as a lubricant additive. The goal is to create free-flowing powder to reduce porosity and defects in the pellets. The powder was split into 2 g each and pressed in a 25 mm die at 40 MPa for 1 minute.

Heat treatment: calcination

The next step in the solid-state synthesis process was the calcination of the powder. The pellets were placed in an alumina crucible with a lid with a small gap and then put in a Super Kanthal 3 oven. The calcination was performed at 1000 °C for 4 hours with a heating and cooling rate of 200 $\frac{^{\circ}C}{h}$.

3.1.2 Producing sintered pellets

After calcination, the pellets were crushed and ground. Afterward, the powder was milled, dried, ground, and sieved. The same parameters and equipment used pre-calcination were reused.

Isostatic pressing of pellets

The calcined powder was first pressed into pellets using a uniaxial press with a 10 mm die at 40 MPa for 1 minute. Stearic acid was again used as a lubricant additive. Continuing after the uniaxial pressing, the pellets were put in a plastic cover to prepare for isostatic pressing. The pellets were pressed isostatically at 29 kpsi (2 kbar) for 1 minute. Each pellet contained 0.35 g powder.

Heat treatment: sintering

The pellets were placed in an alumina crucible and sacrificial $BaTiO_3$ powder was placed underneath and on top of the pellets to cover the samples and reduce the likelihood of volatilization. The sintering was performed in Super Kanthal 3, which was the same oven used for the calcination. The holding time and temperature of the sintering were 1350 °C and 4 hours. The ramping

heating and cooling rate was 200 $\frac{^{\circ}C}{h}$. The sintering parameters were chosen based on literature and prior experiments performed by Holum (2022)[1, 47, 48]

Polishing/Grinding

Before performing measurements on the sintered samples they had to be polished. All the pellets were polished using silicon carbide (SiC) abrasive paper. The polishing was performed manually and it was important to try to polish all parts of the pellet equally. The grit size of the SiC paper was increased gradually from 1200 to 2000 and lastly to 4000. 100% ethanol was used as the polishing media. After polishing with SiC abrasive paper the pellets were cleaned using 100% ethanol and a finger-ultrasound bath at 20% amplitude for 2 minutes. This was done to reduce the likelihood of SiC particles being stuck on the surface. The polishing will create a smoother surface and this is especially important for AFM/PFM measurements. Therefore the BT pellets undergoing PFM measurements were further lapped and polished using respectively Al_2O_3 and SiO_2 particles. This polishing procedure for PFM measurements is further explained in section 3.2.4.

3.2 Characterization

3.2.1 Particle size distribution (PSD)

A PSD measurement of the calcined powder was performed using a Laser Scattering Particle Size Distribution Analyzer (Horiba LA-960). A PSD measurement was used to determine the particle size distribution of the BT powder. The sample used for PSD was gathered directly from the slurry of the ball milling of the calcined powder. The slurry was gathered in a specific way, by stirring the pipette around and collecting and releasing the solution three times. Afterward, the solution was put in the finger-ultrasound bath for 30 seconds at 10% amplitude. Both the gathering of the sample and the ultrasound bath was done to remove agglomeration. In this way, the particle size distribution measurement will be an average of all particles. PSD was measured both as a volume percentage (q) and undersize. The volume percentage describes the percentage of particles that has a certain measured particle size. The undersize shows the fraction of the particles that are smaller than a certain particle size.

3.2.2 X-ray diffraction (XRD)

The phase purity of $BaTiO_3$ was investigated by running X-ray diffraction measurements using a Da Vinci 1 diffractometer. XRD was performed both on the calcined powder and the sintered pellets. The calcined powder was prepared for XRD by using a flat powder holder with ridges and adding the powder to the holder. The surface was then flattened out and it was made sure there was no "cavity" or "mountain" of the powder. XRD on the sintered pellet was run using

a deep sample holder. All the XRD measurements used the same XRD program: 65 min program from $2\Theta = 15°$-$85°$ as a fixed slit. The XRD data was compared to PDFs of the cubic (PDF 01-074-4539) and tetragonal (PDF 04-012-8129) phase of $BaTiO_3$. The data was also compared to PDFs of other stoichiometric phases of Ba, Ti, and O. To analyze contamination, the mismatched peaks were also compared with some aluminum or carbon phases.

3.2.3 Scanning electron microscope (SEM) and energy dispersive spectroscopy (EDS)

The microstructure of BT was investigated using SEM and EDS. The grain structure and grain size were studied, together with focusing on any eventual secondary phases. Before SEM measurements the samples were placed in an alumina crucible and thermally etched. The pellets were thermally etched in the Super Kanthal 3 oven at a peak temperature of 1300 °C for 5 minutes with a ramping rate of 600 $\frac{^\circ C}{h}$. When etching at 1300 °C two of the pellets from BT02 experienced cracking and the peak temperature for thermal etching was therefore lowered to 1250 °C for the remaining pellets (BT03, BT04, BT05, BT06). The samples were also sputtered with carbon to prevent the effect of charging during SEM measurements.

The SEM and EDS measurements were performed in the Nanolab cleanroom (ISO 5), using SEM APREO. The parameters for all the SEM measurements are given in Table 3.6. SEM APREO can also perform EDS measurements, and this data was analyzed using Aztec software. EDS mapping was used to study the chemical composition on the surface of the sample. To get a representative and average view of the microstructure, each sample was studied at three different spots at different magnifications (250x, 500x, 800x, 1500x, 2500x, 5000x, and 10000x).

Table 3.6: SEM and EDS parameters

Current	Voltage	Working distance	Mode	Detector
1.60 nA	5 kV	10 mm	ETD	Secondary electron

3.2.4 Piezoresponse force microscopy (PFM/AFM)

The domain patterns of barium titanate pre-and post-soaking were studied using the atomic force microscope NT-MDT NTEGRA in PFM mode, with an ASYELEC.01-R2 Ti/Ir-coated tip. Only the samples soaked in ultrapure water were studied with PFM, due to the samples soaked in SBF having a too rough surface to achieve any detailed PFM images. Both AFM and PFM scans were performed, but the AFM scans were only used to make sure that topographic artifacts did not influence the analysis of the PFM scans. Prior to the measurements the samples were lapped and polished using respectively Al_2O_3 particles and SiO_2 particles. This is a chemomechanical process due to the mechanical forces from the polishing pad and the chemical forces from the silica slurry. This additional polishing procedure was performed after the regular

mechanical polishing procedure explained in section 3.1.2. Before conducting measurements on the samples, they were cleaned with acetone and ethanol (96%) in an ultrasonic bath and finally cleaned with methanol (70%) using a lens cleaning paper. The samples were then placed on a conductive metal disk using silver paste before being put on an anti-vibration desk. The laser was then aligned before the PFM measurement was run. Both in-plane and out-of-plane polarization measurements were performed. The area scanned over ranged from 20-40 µm. The samples were only scanned in one direction. The PFM signal shown in the images is calculated using the following equation:

$$\text{PFM signal} = A \cdot cos(\phi), \tag{3.1}$$

where A is the PFM amplitude and ϕ is the PFM phase. This is done to reduce the impact of noise and inaccuracies in the measurements.

3.2.5 Piezoelectric measurements

Piezoelectric measurements are crucial to perform on the BT samples, due to the importance of verifying the ferro-and-piezoelectric properties of the samples. The measurements were done using AIX PES Piezoelectrical evaluation. To prepare the samples for piezoelectric measurements the pellets were painted with silver paste (Ami Doduco, Auromal) on each side before being air-dried. The silver paint made the BT samples conductive and also reduced the resistance of the electrical flow when an electrical field was applied. The piezoelectric measurements were controlled using Aixplorer software. An electrical field of up to 1.5 kV at 1 Hz was applied to pole the BT material. The polarization and strain were then measured and plotted as a ferroelectric hysteresis loop and strain loop. The piezoelectric coefficient was measured using a Berlincourt meter, and this is further described in the subsection below (3.2.6).

3.2.6 Preliminary poling study

A preliminary poling study was performed to assess the effect of poling on the piezoelectric response of the barium titanate pellets. The BT pellets were poled using a corona discharge poling setup. The in-house corona discharge setup is illustrated in Figure 3.2. Corona discharge poling is a non-contact poling technique that utilizes a large electric field between a sharp conductive tip and a grounded plate. The sample is then placed on top of this plate and the large electric field creates a secondary effective electric field due to ions being produced and placed onto the sample surface [49]. For this thesis, the piezoelectric barium titanate pellets were placed on a steel plate at room temperature and a 20 kV electric field was applied for different time intervals. The preliminary poling study was conducted with 3 samples for each parallel for the 6 different time intervals, resulting in a total of 18 samples being studied. The time intervals for the poling were: 0 seconds, 10 seconds, 30 seconds, 60 seconds, 180 seconds, and 300 seconds.

Afterward, the samples were painted with silver paste (Ami Doduco, Auromal) and air-dried, to be ready for d_{33} measurements.

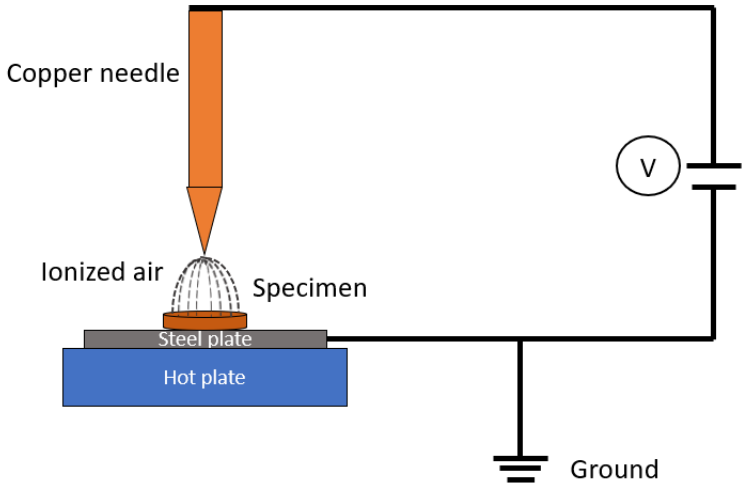

Figure 3.2: The figure shows the in-house corona discharge setup. The figure is made based on inspiration from an article by Julia Glaum and Magnus Rotan from 2020, and a thesis by Marcus Bentzen from 2021 [49, 50].

d_{33} measurements

The piezoelectric d_{33} coefficient of each BT pellet was measured using a Sinocera YE2730A d_{33} Berlincourt meter. The sample was clamped in place and a low-frequency force was applied while the piezoelectric response was measured and the d_{33} could be read out from the instrument. Both the negative and the positive piezoelectric coefficient was measured. By flipping the sample the opposite d_{33}-value was measured. As mentioned, three parallels were run for each time interval, and the piezoelectric coefficients for each poling time were plotted, together with the standard deviation.

3.2.7 Poling

Based on the preliminary poling study, it was concluded that a poling time of 0 seconds, 10 seconds, 60 seconds, and 300 seconds, would give sufficient information about the effect of poling on the piezoelectric and biocompatible properties of barium titanate. After the poling study, the silver paint on all the samples was removed by using acetone and a finger-ultrasound bath. Table 3.7 shows the poling time for each individual pellet. The poling was prepared prior to the PFM measurements and the soaking study. The samples from the preliminary poling study that were not correctly poled, were depoled. The pellets were put on a hot plate at 180 °C, to make sure that the barium titanate reached a temperature over the Curie temperature and that

the domains would switch back to random orientation. The BT pellets were then poled for the correct amount of time as described in Table 3.7.

Table 3.7: Poling time for each specific pellet prior to PFM measurements and soaking study.

Poling time	Pellet ID
0 seconds (Non poling)	BT02p1, BT03p1, BT03p5, BT04p1, BT05p1, BT05p5
10 seconds (Low poling)	BT02p4, BT03p2, BT03p6, BT04p2, BT05p2, BT05p6
60 seconds (Medium poling)	BT02p5, BT03p3, BT04p3, BT04p5, BT05p3, BT06p1
300 seconds (High poling)	BT02p6, BT03p4, BT04p4, BT04p6, BT05p4, BT06p2

3.2.8 Archimedes method

The Archimedes density method is used to calculate the bulk density (ρ_b), closed porosity (π_a), and total porosity(π_t). It was important to measure the porosity both to verify the effect of sintering and also to determine the amount of liquid needed for the soaking study (section 3.4). The pellets were dried overnight in a 120 °C drying cabinet before the dry weight (m_1) was measured. The pellets were then placed in a vacuum chamber and the first 20 minutes were spent to get a sufficient vacuum. Afterward, isopropanol (C_3H_8O) was sucked into the chamber and covered the pellets with at least 2 mm. The pellets were soaked in isopropanol for 30 minutes in a vacuum and then 30 minutes in the open air. Then the wet weight (m_2) of each pellet was measured, by still keeping the pellet in isopropanol. The pellets were removed from the isopropanol and quickly and gently dried with fine paper before the soaked weight was measured (m_3). Based on the values of m_1, m_2, and m_3, the following equations were used to calculate the bulk density, and closed and total porosity.

The bulk density is calculated through equation 3.2.

$$\rho_b = \frac{m_1}{m_3 - m_2} * \rho_{liq}, \tag{3.2}$$

where ρ_{liq} is the density of the liquid and in this case isopropanol. The density of isopropanol is dependent on the temperature (T (℃)) through this equation:

$$\rho_{liq} = -0.0009 * T + 0.8018 \tag{3.3}$$

The closed/apparent porosity and total porosity are calculated using equation 3.4 and 3.5

$$\pi_a = \frac{m_3 - m_1}{m_3 - m_2} * 100 \tag{3.4}$$

$$\pi_t = \frac{\rho_t - \rho_b}{\rho_t} * 100, \tag{3.5}$$

where ρ_t is the theoretical density of barium titanate, $\rho_t = 6.02 \frac{g}{cm^3}$ [51].

In this thesis, the density of two pellets from each sintering batch was measured using the Archimedes method.

3.2.9 Optical Microscope

The surface roughness of the barium titanate pellets was studied pre-and post-soaking using Alicona Infinite Microscope. The S_A value was used as the parameter for determining the surface roughness. This is a value describing the arithmetical mean height on a sample surface and is used to compare the surface roughness of different samples. A 50x optics was used and an 408x408 μm^2 area was studied. The lateral resolution was 2.14 µm, while the vertical resolution was 40 nm, and the surface roughness was measured through a varying thickness of $Z = \pm 30$ µm. The vertical resolution on the instrument was not sufficient to measure the surface roughness on the samples polished and prepared for PFM. These samples have very small topographic differences due to the very thorough polishing procedure explained in section 3.2.4. The vertical resolution was sufficient for the rest of the samples that were only polished manually with a SiC abrasive paper. The reason for measuring the surface roughness both pre-and post-soaking, is that an increase in the surface roughness could indicate Ba^{2+} leaching. For the samples soaked in SBF, a change in the surface roughness could also indicate the precipitation of CaP.

3.3 Simulated body fluid (SBF)

SBF was prepared following the ISO standard 23317. This ISO standard was also used during the entire soaking study as explained in section 3.4.

3.3.1 Preparation

700 mL of ultrapure water (MilliQ) was put in a 1 L plastic beaker and placed in a water bath together with a magnetic stirrer. The water bath was placed on a hot plate and the hot plate was set to 38 °C, together with a gentle stir of the magnetic stirrer. The ultrapure water was left until the temperature reached 36.5 ± 1.5 °C. The reason for using a plastic beaker instead of glass equipment is due to a plastic container having a smooth surface and no scratches. Scratches on glass equipment could induce unwanted apatite formation.

3.3.2 Dissolving reagents

While the solution reached the designated temperature, all the reagents were weighed out to the correct amount, shown in Table 3.8. The reagents were then stored in a desiccator, due to

the hygroscopic properties of the powders. 1M HCl was prepared by diluting a 12M stock of HCl. 8.3334 mL 12M HCl was measured and put in a 100 mL volumetric flask, before adding ultrapure water until it reached the marked line. The reagents were then dissolved in the correct order. All the reagents were carefully dissolved and the following reagent was not added to the solution until the preceding one was completely dissolved. The temperature was also controlled at all times to be 36.5 ± 1.5 °C. $CaCl_2$ was dissolved with extra care due to the large granules resulting in a lower surface area and slower dissolution. After all the 1-8 reagents were dissolved in the solution, the pH was 1.51, and well within the range of 2.0 ± 1.0. Ultrapure water was then added to the plastic beaker so the total volume reached 0.9 L.

Table 3.8: Reagents used for the preparation of SBF.

Order	Reagent	Theoretical amount	Experimental amount	Purity	Supplier
1	NaCl	8.035 g	8.0357 g	99.5%	Sigma-Aldrich
2	$NaHCO_3$	0.355 g	0.3554 g	99.5%	Sigma-Aldrich
3	KCl	0.225 g	0.2255 g	99.5%	Sigma-Aldrich
4	$K_2HPO_4 \cdot 3\,H_2O$	0.231 g	0.2318 g	99.0%	Sigma-Aldrich
5	$MgCl_2 \cdot 6\,H_2O$	0.311 g	0.3116 g	98.0%	Sigma-Aldrich
6	HCl 1M	39 mL	39 mL	-	Sigma-Aldrich
7	$CaCl_2$	0.292 g	0.296 g	95.0%	Sigma-Aldrich
8	Na_2SO_4	0.072 g	0.0747 g	99.0%	Sigma-Aldrich
9	(TRIS):$((HOCH_2)_3CNH_2$	6.118 g	6.1191 g	99.0%	Sigma-Aldrich
10	HCl1 M	0-5 mL	8 mL	-	Sigma-Aldrich

3.3.3 Creating a buffer

When creating the buffer, the temperature was controlled to be 36.5 ± 0.5 °C for all further steps. TRIS was added in small amounts until it dissolved completely and a stable pH was reached. This procedure was kept until the pH reached 7.45 ± 0.01. Then HCl was added with a syringe until the pH reached 7.42 ± 0.01. Then TRIS was again added to the solution while the pH was made sure to be kept under 7.45. This process with adding TRIS and HCl alternately to the solution while keeping the pH between 7.42-7.45 was kept up until all TRIS was dissolved. The temperature was then adjusted to be 36.5 ± 0.2 °C while the pH was adjusted to 7.42 ± 0.01 by adding small amounts of HCl. Finally, the temperature was controlled to be stable at exactly 36.5 °C (less increase or decrease than 0.1 °C/min), and the pH was adjusted to 7.40 exactly.

3.3.4 Washing and cooling

When the solution reached an exact temperature and pH, the pH meter was removed from the solution and rinsed with ultrapure water and the washings were added to the plastic beaker. The SBF solution was then poured from the plastic beaker into a 1 L volumetric flask. The plastic beaker was rinsed with ultrapure water and the washings were added to the volumetric flask. Ultrapure water was then added to the flask until the marked line was reached. The flask was then put on a 20 °C water bath. When the SBF solution reached 20 °C the volume had reduced a bit and small amounts of ultrapure water were then added to adjust for this reduced volume. The SBF was then preserved in a plastic container sealed with plastic film and stored in a 5 °C refrigerator.

3.4 Soaking studies

When all the necessary characterization methods on the BT pellets were completed, the soaking study was performed. The soaking study was performed both for ultrapure water (conductivity = 0.2098 µS/cm at low CO_2 levels [52]) and simulated body fluid. As explained in Table 3.7 the pellets were poled at different states. One pellet at each poling state was soaked in ultrapure water or simulated body fluid for three different soaking times. The soaking times and the soaking media for each pellet are given in Table 3.9. As explained in section 3.3 the ISO standard 23317 was used during the entire soaking study. After the poling, it was made sure which side of the pellet was negative and positive charged. The negative charged surface was placed upwards when soaked in SBF and UPW.

The volume needed for soaking the BT pellets is calculated using the surface area of the samples. The surface area formula is given in equation 3.6.

$$A = 2\pi rh + 2\pi r^2, \tag{3.6}$$

where A is the surface area of the material, r is the radius and h is the thickness. The volume (v_s) that each pellet is soaked in is calculated through equation 3.7.

$$v_s = 100mm * A, \tag{3.7}$$

where v_s is given in $mm^3 = mL$. The total porosity (π_t) is also accounted for when calculating the effective surface area and is measured using the Archimedes method. The adjusted volume (v_s^*) is calculated using equation 3.8.

$$v_s^* = \frac{v_s}{\frac{(1-\pi_t)}{100}}. \tag{3.8}$$

Before soaking the pellets, the pH of the two solutions was measured with a pH meter. The pH meter was first calibrated using standard buffer solutions of pH = 4, 7, and 10. The pH of the soaking solutions was also measured after soaking, following the same procedure. An increase in the pH of the soaking media could give an indication of Ba^{2+} leaching due to the reaction equation shown in theory section 2.6. To make the soaking environment more realistic, it was performed in a heating chamber set to the average body temperature of 37 °C. After soaking the pellets in ultrapure water, they were cleaned by rinsing in 100% ethanol, before being dried in a 120 °C heating cabinet for 10 minutes. The BT pellets immersed in SBF were only rinsed carefully with ultrapure water before being dried in a desiccator. The reason for carefully cleaning the BT samples soaked in SBF is to not remove any eventual CaP precipitation on the surface.

After the completion of the soaking study, all the samples were analyzed using the same characterization methods as before soaking.

Table 3.9: Soaking time and media.

Pellet IDs	Soaking time	Soaking media
BT02p1, BT02p4, BT02p5, BT02p6	1 hour	SBF
BT03p1, BT03p2, BT03p3, BT03p4	1 hour	Ultrapure water
BT03p5, BT03p6, BT04p5, BT04p6	24 hours	SBF
BT04p1, BT04p2, BT04p3, BT04p4	24 hours	Ultrapure water
BT05p5, BT05p6, BT06p1, BT06p2	5 days	SBF
BT05p1, BT05p2, BT05p3, BT05p4	5 days	Ultrapure water

4 Results

4.1 Optimization of microstructure and phase purity

To be able to run the soaking study on the barium titanate pellets, the microstructure and phase purity of the material had to be optimized. Having a phase-pure material and a homogeneous microstructure are important features for optimizing the mechanical and functional properties of the material, and to be able to describe the origin of the observed changes after soaking. These characteristics are also important for making the material as relevant for biomedical applications as possible, due to all material properties having to be optimized for BT to be used as an application in a medical implant.

4.1.1 Microstructure

As described in the experimental subsection 3.1.2, the sintering parameters were chosen based on literature and prior research done by the author[1, 47, 48]. The microstructure for Batch1 of the sintered (at 1350 °C) and thermally etched BT pellets is shown in Figure 4.1a. It is compared with a microstructure of the BT pellets sintered at 1300 °C with the same holding time and ramping rates [1]. This microstructure is shown in Figure 4.1b and was obtained from Holum [1]. The BT sample sintered at 1300 °C shows dark areas of large grains, but lighter grey areas indicating coarse areas with fine grains trapped between the larger grains. Some of these areas are marked with blue circles. The SEM image of the sample sintered at 1350 °C shows large grains with clear grain boundaries and a unimodal grain size distribution. The black areas are pores. On top of the grains, there are some darker elongated particles that could indicate contamination. Some of these particles are marked with a red circle. The lighter grey areas that are seen in Figure 4.1b are not present in Figure 4.1a.

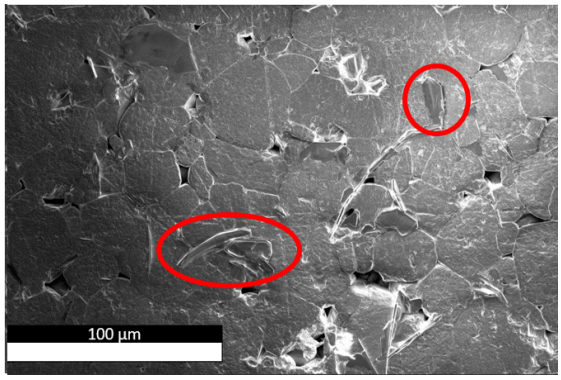

(a) Batch1 (BT01p1 pellet), sintered at 1350 °C

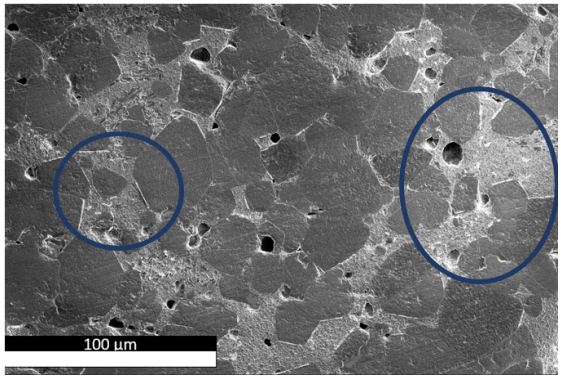

(b) BT pellet sintered at 1300 °C. Obtained from project work thesis by Holum [1].

Figure 4.1: SEM images comparing a microstructure of BT pellet sintered at 1300 °C (a) and 1350 °C (b). Figure a) is obtained from the project work thesis by Holum [1].

Figure 4.2 shows the EDS results of the sintered BT pellets from Batch1. Figure 4.2a shows the microstructure of the scanned area and some secondary phases are seen as darker areas placed on top of the grains. These areas are marked with red circles for the SEM image and the EDS images. The brighter purple areas in Figure 4.2b match the shape and position of the darker areas in Figure 4.2a, and could therefore indicate aluminum contamination. For the EDS images of oxygen and titanium, this effect is not as visible, but the areas marked with red circles are slightly brighter than the rest of the scanned area.

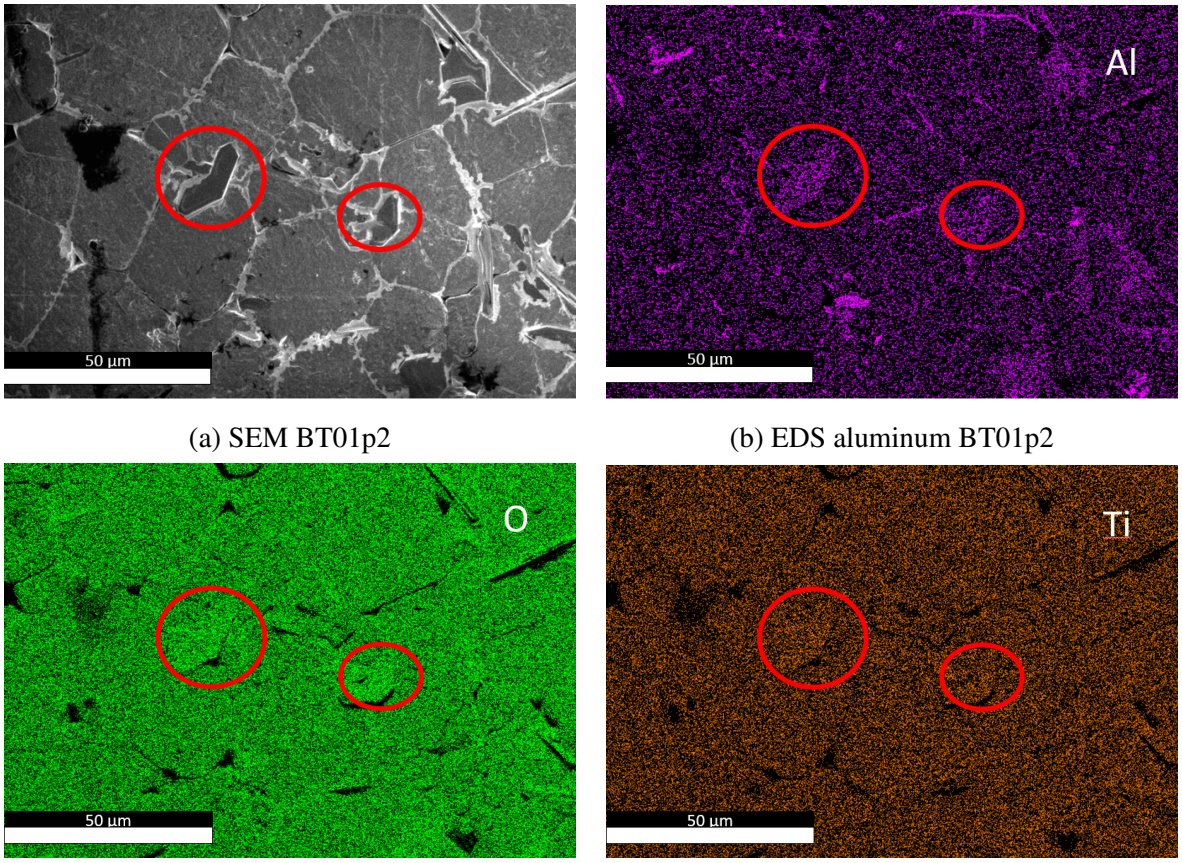

(a) SEM BT01p2

(b) EDS aluminum BT01p2

(c) EDS oxygen BT01p2

(d) EDS titanium BT01p2

Figure 4.2: SEM image of BT01p2 and the corresponding EDS maps of aluminum, oxygen, and titanium.

As described in the experimental section, the suspected aluminum contamination in Batch1 was tried to be removed by changing the synthesis equipment for Batch2 and Batch3. The microstructure of some of the BT pellets from Batch2 (BT03p5) and Batch3 (BT05p1) are presented in Figure 4.3. There are still some darker particles in the microstructure of the BT pellets sintered from Batch2, marked with a red circle in Figure 4.3a. The darker particles show no clear match with the corresponding aluminum EDS map presented in Figure 4.3b.

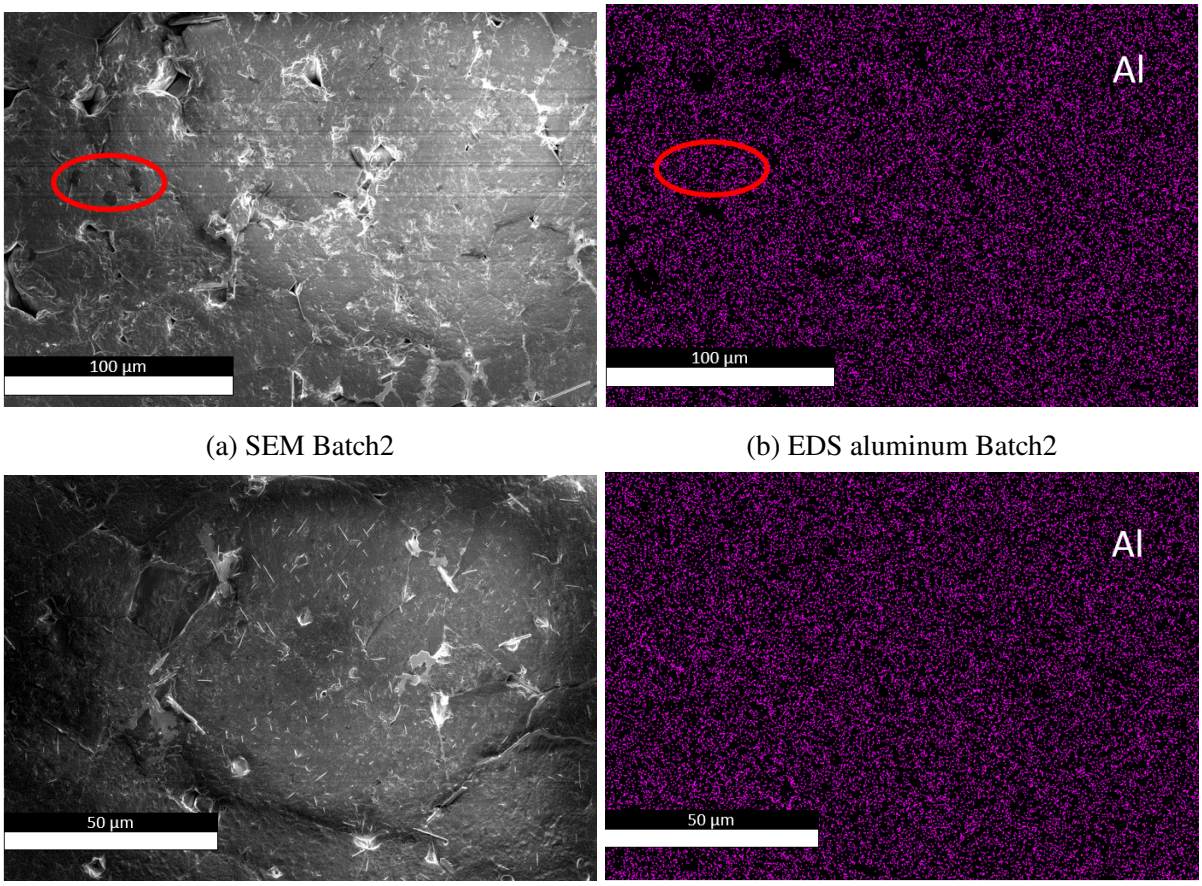

(a) SEM Batch2

(b) EDS aluminum Batch2

(c) SEM Batch3

(d) EDS aluminum Batch3

Figure 4.3: SEM images of pellets from Batch2 (BT03p5) and Batch3 (BT05p1) and the corresponding EDS map of aluminum.

4.1.2 Phase-purity (XRD)

The phase purity of both the barium titanate powder and pellets was studied using X-ray diffraction. All the XRD results are compared with the PDFs for tetragonal $BaTiO_3$ (PDF 04-012-8129) and cubic $BaTiO_3$ (PDF 01-074-4539).

The results of the XRD scans for the three different calcined powder batches are presented in Figure 4.4. The X-ray diffractograms are placed on top of each other and normalized. The XRD results show a great match with the PDFs of $BaTiO_3$ for all the powder batches. Every diffractogram has the same small unidentified peak at around $2\Theta = 28 - 29°$, marked by a black arrow. A tetragonal splitting is not that prevalent for the powder X-ray diffractograms. This is seen by specifically looking at the peak at around 45° corresponding to the (200), (020), and (002) peaks. The peak only shows a small shoulder on the left-hand side, but no clear splitting.

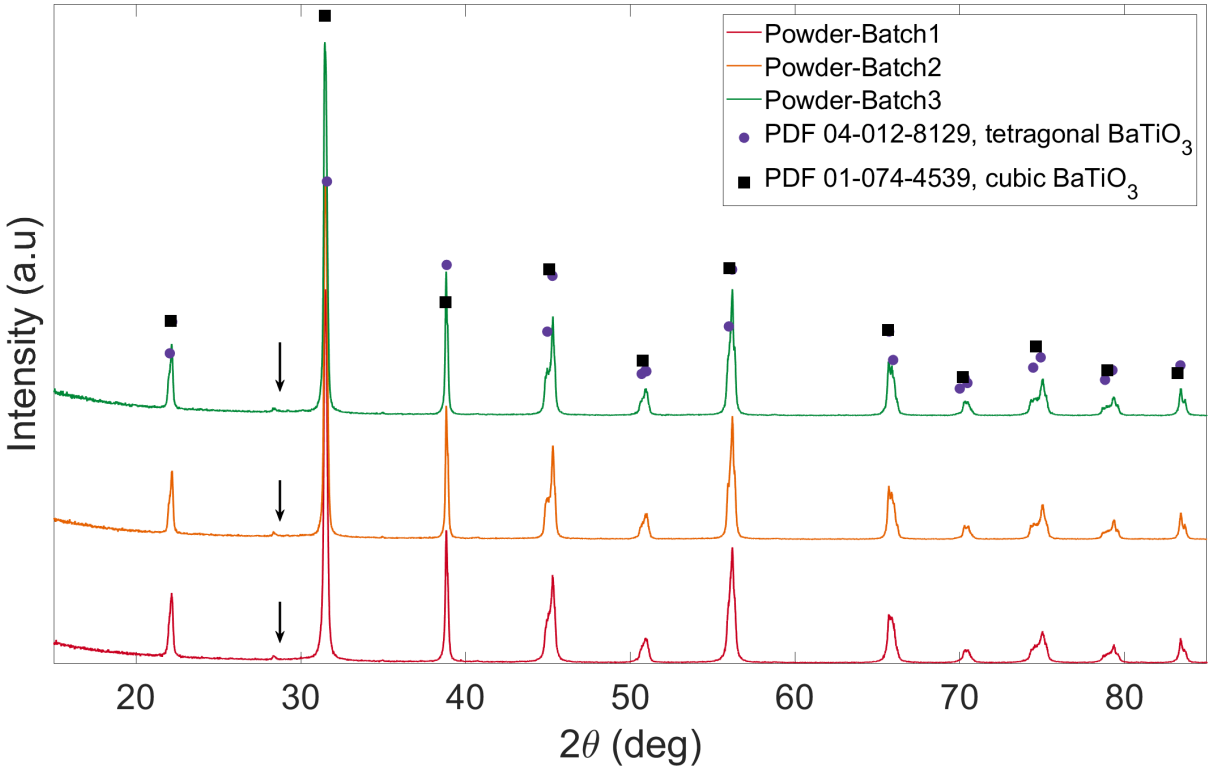

Figure 4.4: Powder XRD of the different calcined powder batches

After sintering, the BT pellets were characterized using X-ray diffraction. The results are presented in Figure 4.5. XRD results on the bulk of one pellet sintered from each powder batch (Batch1, Batch2, and Batch3) are presented. The splitting of the peaks was now visible and indicated that the barium titanate was at the stable room-temperature phase of the tetragonal structure. This was observed for most of the main peaks from $2\Theta = 45 - 85°$, but clearly visible for the peaks at 45°, 51°, 56°, and 75°. The unidentified peak at around $2\Theta = 28 - 29°$ was at the same position as for the powder-XRD but decreased in intensity from Batch1 to Batch2 and Batch3. This is illustrated in Figure 4.5 and marked with black arrows. A new unidentified peak at $2\Theta = 44°$ was observed when performing XRD on the bulk samples. This peak was only visible for the pellets synthesized from Batch1 and Batch2, as seen marked with black arrows. The unidentified peaks at 22° and 44° did not match with Cu $\alpha 2$ radiation.

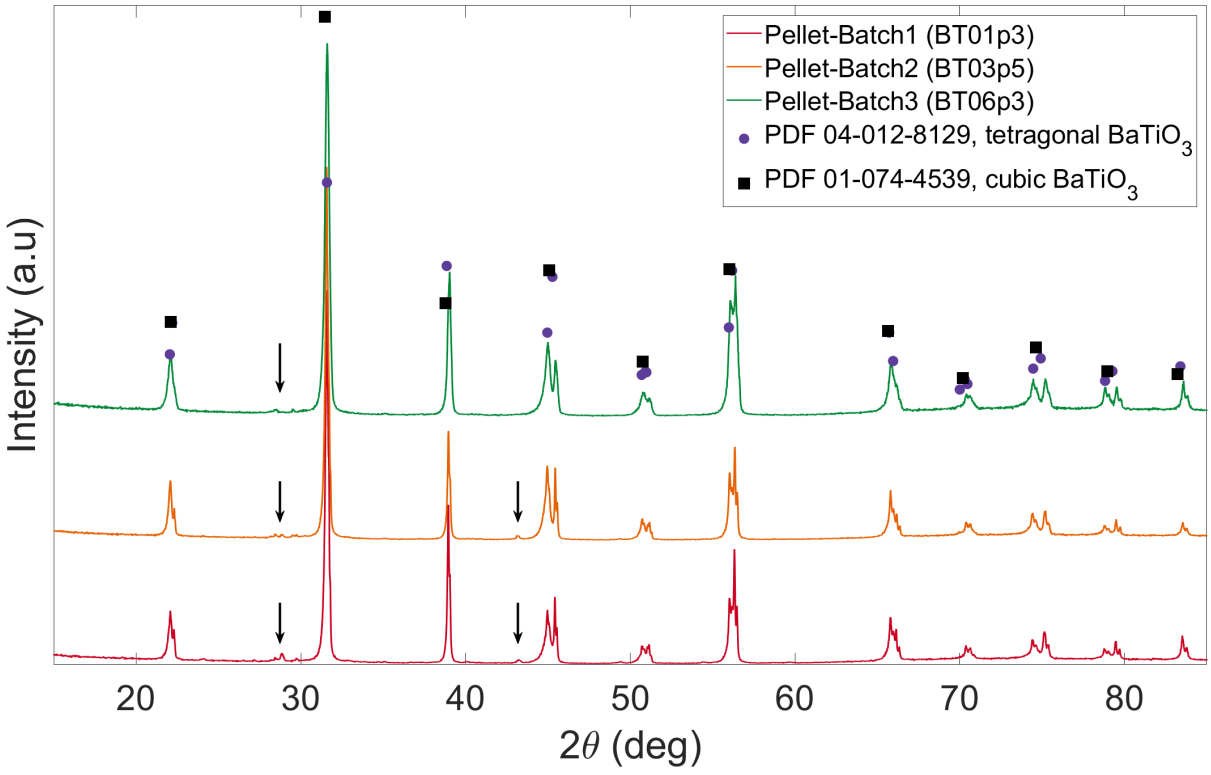

Figure 4.5: XRD of pellets from the different powder batches after sintering.

4.1.3 Particle size distribution

To optimize the properties of the sintered pellets, it is important to control the particle size of the calcined powder. The particle size distribution for each batch is shown in Figure 4.6. Both the volume percentage (q) and undersize of the powders are displayed. As explained in the experimental section 3.2, the volume percentage describes the percentage of particles that has a certain measured particle size. The undersize, on the other hand, displays the fraction of particles that are smaller than a certain particle size value. The PSDs of Batch1, Batch2, and Batch3 were unimodal, which is seen by only having one main peak. The peak particle size of Batch1 was 0.510 µm and the standard deviation was 0.346 µm. The powder in Batch2 had a peak particle size of 1.981 µm and a standard deviation of 1.437 µm. The PSD of Batch3 was more narrow than Batch2, but broader than Batch1. The peak particle size was 0.669 µm and it was also smaller than for Batch2. The standard deviation of Batch3 was 0.924 µm. The standard deviation and peak particle size of each batch are also presented in Table 4.1.

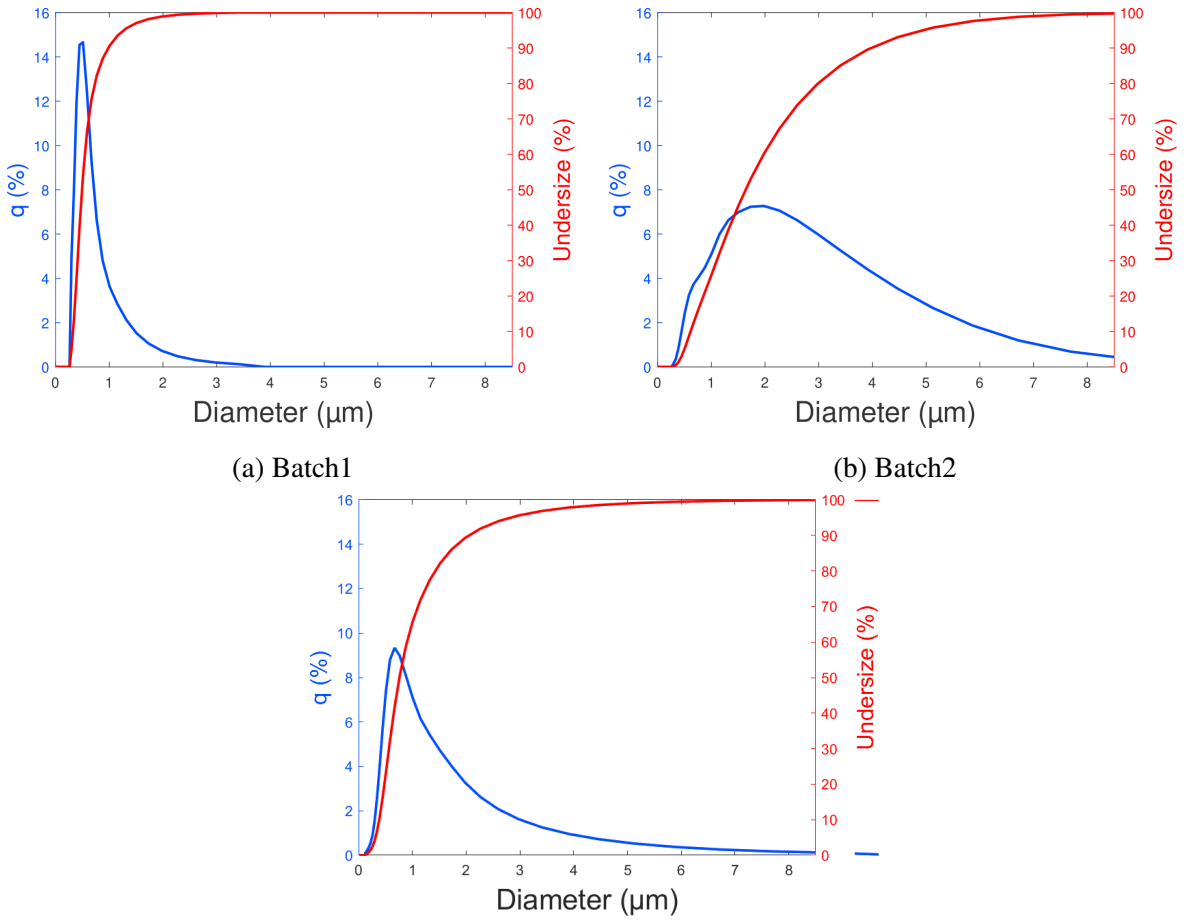

(a) Batch1

(b) Batch2

(c) Batch3

Figure 4.6: PSD of all powder batches

Table 4.1: Peak particle size and standard deviation of each powder batch measured using PSD.

Batch number	Peak particle size [µm]	Standard deviation [µm]
Batch1	0.510	0.346
Batch2	1.981	1.437
Batch3	0.669	0.924

Figure 4.7 shows SEM images of the powder from Batch2. As mentioned, the particle size distribution of Batch2 was broad, and the SEM images confirmed this. The powder consisted of small single particles, but also smaller particles staying together in agglomerate. Figure 4.7b shows the particle size ranging from less than 0.5 µm to agglomerates larger than 2 µm for the powder in Batch2. This confirms the same results seen in the PSD data, and therefore no further SEM images of the other powder batches are presented.

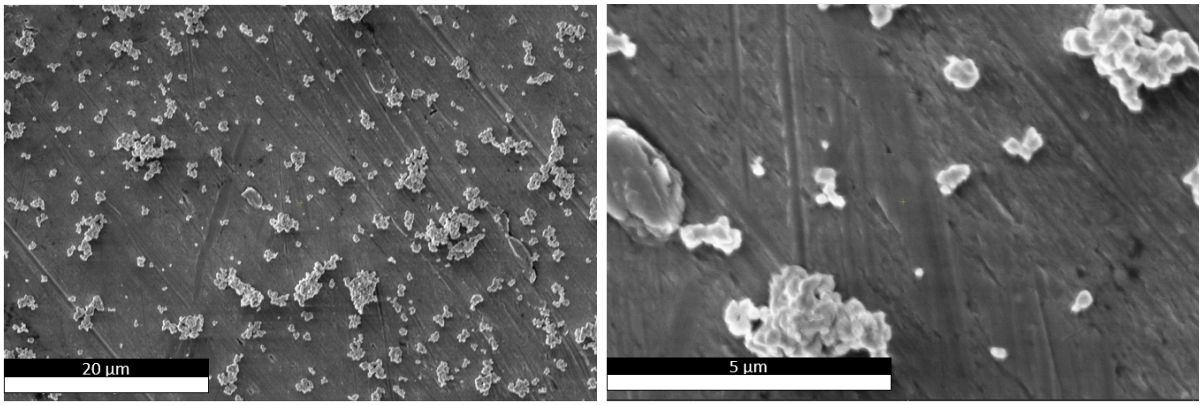

(a) SEM of the BT powder (Batch2).

(b) Zoomed in SEM image of the BT powder (Batch2).

Figure 4.7: SEM images of the BT powder (Batch2).

4.1.4 Relative density

The relative density and standard error of the sintered BT pellets are presented in Figure 4.8. Two pellets from each pellet batch were used to determine the relative density. The relative density values were calculated with the theoretical density of $BaTiO_3$ being $\rho_t = 6.02 \frac{g}{cm^3}$ [51]. The densities varied between 94.791 and 98.809. The pellets sintered from Batch3 (BT04, BT05) had a generally higher relative density than the pellets from Batch2 (BT02, BT03) and Batch1 (BT01), except for BT06 (Batch3). The relative density of the pellets from Batch1 was the lowest.

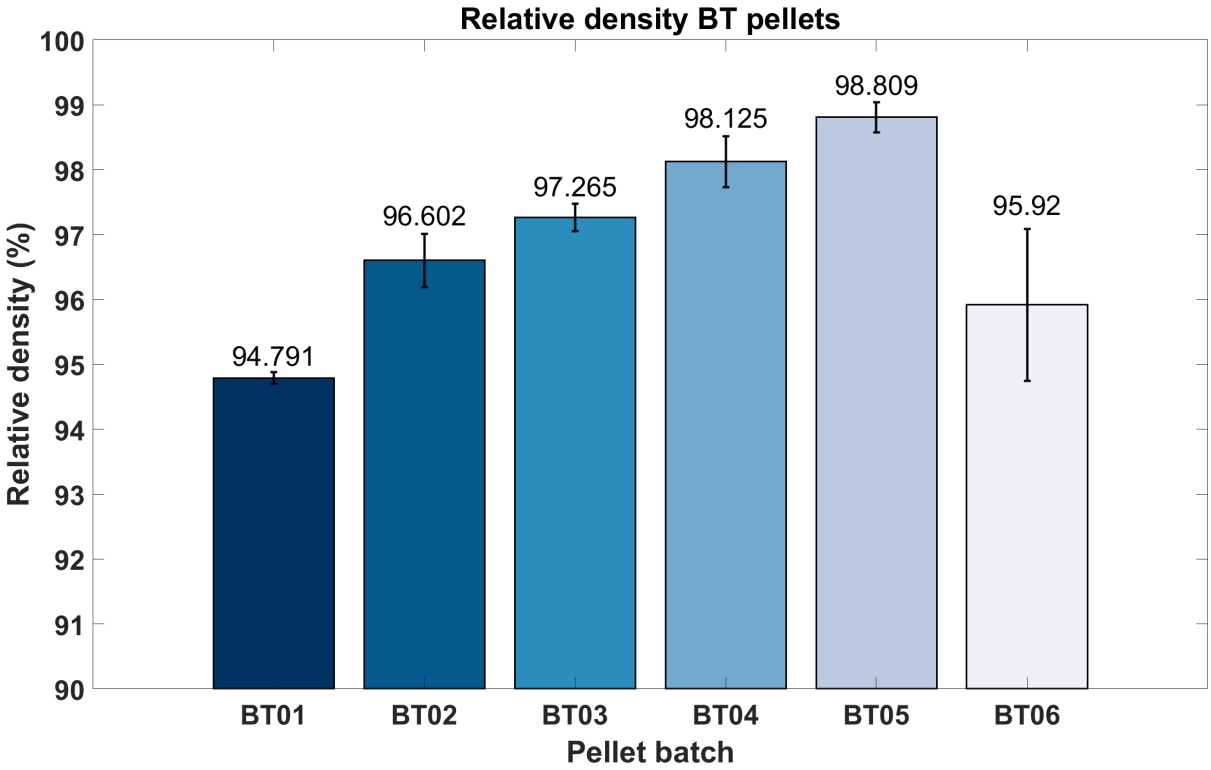

Figure 4.8: Relative density of the different pellet batches of barium titanate. BT01 belongs to powder Batch1, while BT02 and BT03 belongs to Batch2 and BT04, BT05, BT06 belongs to Batch3.

4.2 Surface roughness

After optimizing the powder and pellet properties of barium titanate, the material could be further characterized.

The surface roughness of the polished BT samples was measured using an optical microscope and the results of the unsoaked samples are presented in Figure 4.9. As explained in section 3.2.9, a common parameter for comparing the surface roughness is the S_A value. The average S_A value together with the standard deviation was calculated based on the surface roughness data at three different spots on each sample. The average surface roughness of each pellet varied between $S_A = 0.08\,\mu\text{m} - 0.29\,\mu\text{m}$. A larger surface roughness could indicate pores or defects in the material. The measurements were performed for all the BT samples used for the soaking study, except for BT03p1-BT03p4. The reason for not measuring the surface roughness of these samples was due to these samples being used for the PFM analysis and therefore going through a different polishing procedure. The vertical resolution of the instrument was out of range when measuring the S_A value of the BT samples BT03p1-BT03p4.

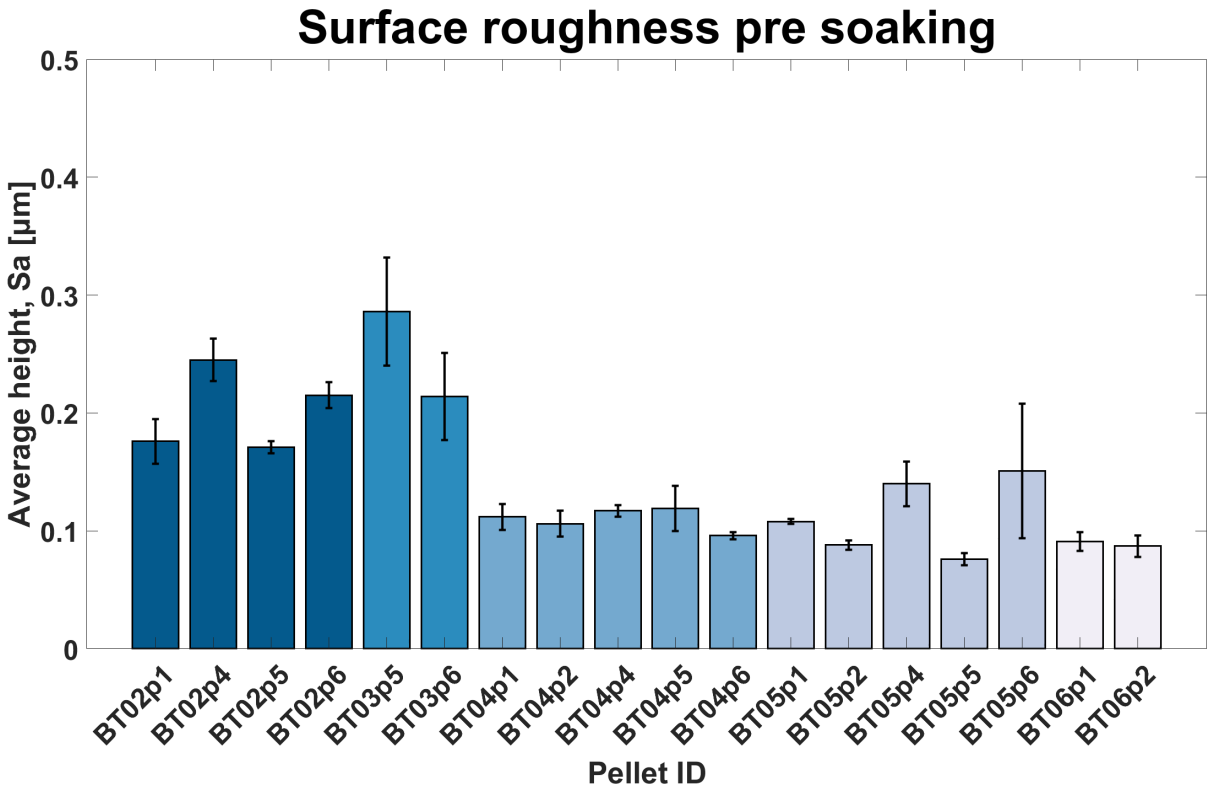

Figure 4.9: Surface roughness of the sintered BT pellets before soaking.

4.3 Piezoelectric properties

The main functionality of barium titanate in the use of bone implants comes from its piezoelectric properties. Therefore it was important to measure and confirm the piezoelectric properties of the BT pellets before and after soaking. Figure 4.10a shows the hysteresis polarization loops of four different pellets before soaking. The samples had varying thicknesses from 0.95-1.10 µm, but the same electric voltage of 1.5 kV was applied to each sample. The polarization and strain were plotted against the electric field by normalizing the electric voltage to the thickness of the sample. There was not used any insulating medium, such as silicone oil, and therefore an electric voltage of only 1.5 kV was applied, to reduce the risk of a dielectric breakdown. BT04p1 and BT06p4 showed symmetrical hysteresis polarization loops, confirming that a ferroelectric material had been synthesized. BT01p3 and BT03p5 showed polarization loops with a less distinct hysteresis behavior, which is seen by the loops being flatter and also being pinched around the electric field, E = 0 kV/cm. To study the piezoelectric behavior of the BT01p3 sample further, the electric voltage was increased up to 3 kV. At 2.4 kV the sample showed a distinct ferroelectric hysteresis behavior. By increasing the electric voltage to 3 kV the sample sparked and experienced a dielectric breakdown. The strain loops are presented in Figure 4.10b and BT04p1 and BT06p4 show butterfly-shaped loops with a peak displacement of 0.06%. BT01p3 and BT03p5 show strain loops that have a flatter butterfly shape, which reached a peak displacement of around 0.02%. The piezoelectric coefficients were measured using a Berlincourt meter, and the positive and negative d_{33}-values are presented in Table 4.2. The positive values ranged from 1.1 pC/N to 18.5 pC/N, while the negative values ranged from -1.1 pC/N to -15.2 pC/N.

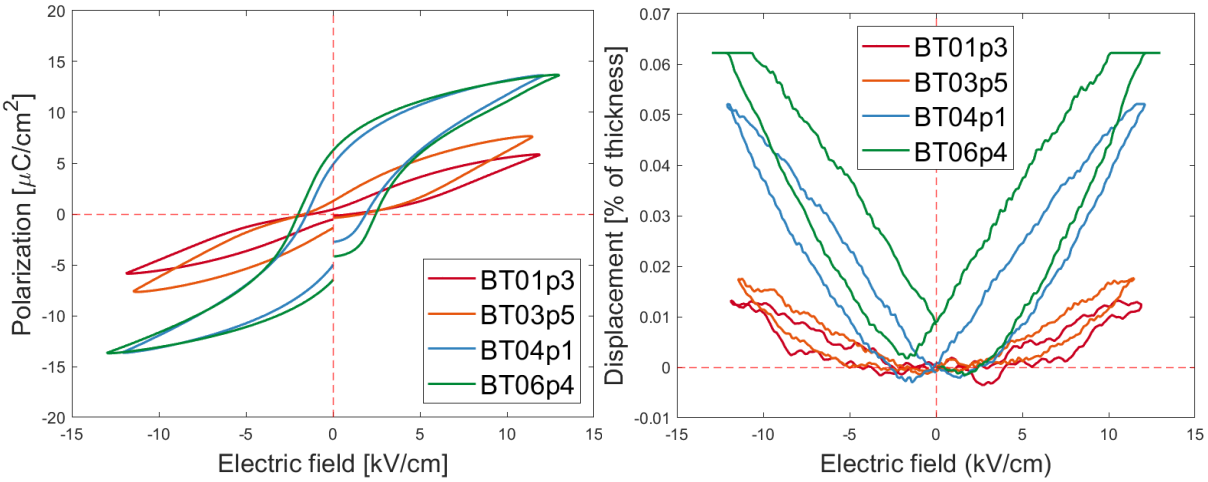

(a) Polarisation curves

(b) Displacement curves

Figure 4.10: Piezoelectric measurements of four BT samples before soaking.

Table 4.2: d_{33} measurements performed by a Berlincourt meter on pre-poled BT before soaking.

Pellet ID	d_{33} [pC/N] (positive)	d_{33} [pC/N] (negative)
BT03p5	18.5	-15.2
BT04p1	2.2	-2.0
BT06p4	1.1	-1.1

4.4 Poling and domains

4.4.1 Preliminary poling study

To determine the appropriate poling parameters for the BT pellets, a preliminary poling study was performed on 18 different barium titanate samples. The BT samples were poled for 6 different time intervals by corona discharge and both the negative and positive piezoelectric d_{33} coefficient was measured with a Berlincourt meter. The results are presented in Figure 4.11. It showed a semi-linear increase in the piezoelectric coefficient for increased poling time until 3 minutes of poling when it started flatting out. The negative d_{33} values were measured by flipping the sample, and the material showed a great symmetrical behavior of the piezoelectric coefficients. The negative values were plotted to confirm that the poling was consistent and that the two opposite sides of the BT pellet had opposite surface charges. Due to the poling behavior shown in Figure 4.11, the poling parameters chosen for the soaking study were: 0 seconds, 10 seconds, 60 seconds, and 300 seconds.

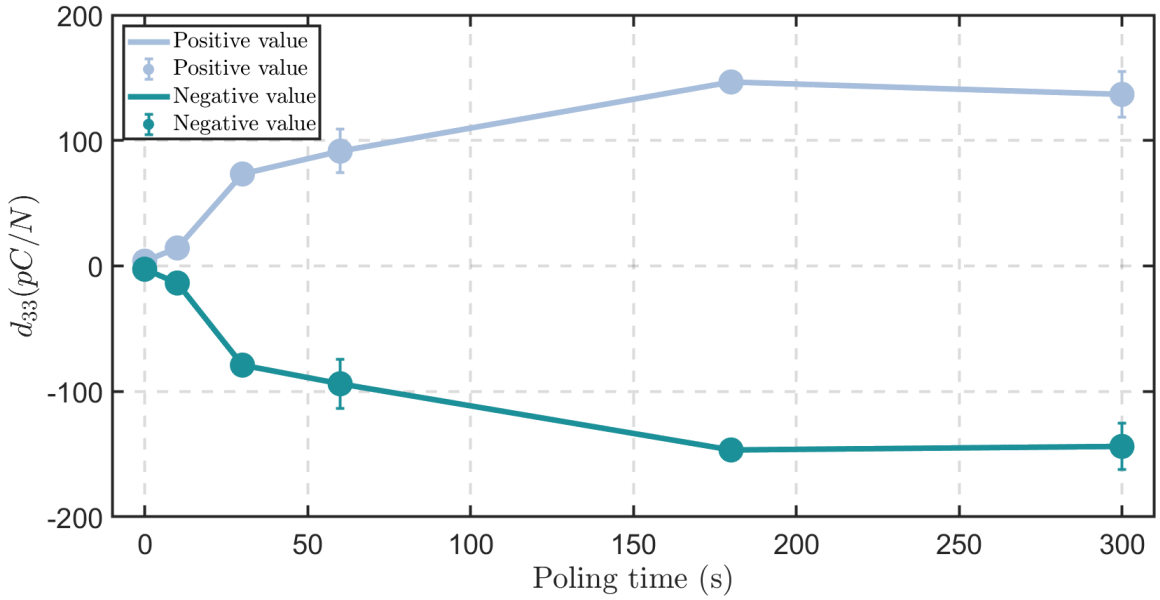

Figure 4.11: The positive and negative piezoelectric coefficients after poling the BT samples for different poling times. Three samples were poled for each of the six different poling times.

4.4.2 Domain structure

After poling, the domain structure was studied using piezoelectric force microscopy. As explained in the experimental section 3.2.4, the signal output is given as the PFM amplitude times the PFM phase. The signals detected were both in-plane and out-of-plane signals. Figure 4.12 shows the in-plane signal of the samples poled to different states. To compare the PFM scans over the same area size, the PFM images were cropped to an area of 20x20 μm^2. This is shown in Figure 4.13. The images were cropped using the software Gwyddion. All scans show stripe formations in different directions, which represents piezoelectric domains. The direction of the stripes changes across a grain boundary, which is easily visible for the 10-second poled sample in Figure 4.12b. The grain boundaries are marked inside the blue oval, and the stripe direction is shown with the black arrows. It is important to note that the black arrows only show the stripe direction, and do not explain the polarization direction of the domains. The size of the stripes varies for each sample, and this is observed clearly for the 60-second poled sample in Figure 4.13c. The stripes on the top right part of the area are larger and decrease as moved to the left of the area. This is marked with a blue oval in Figure 4.13c.

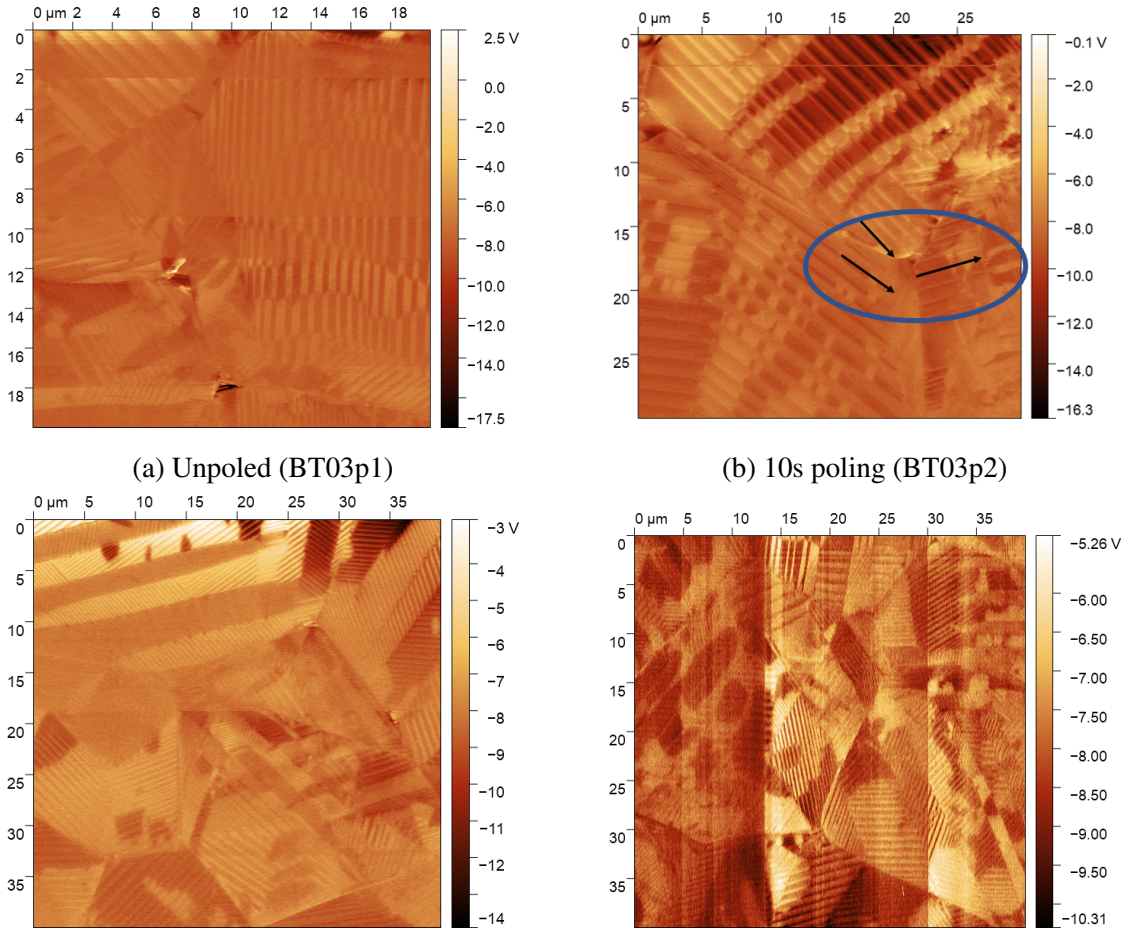

(a) Unpoled (BT03p1)

(b) 10s poling (BT03p2)

(c) 60s poling (BT03p3)

(d) 300s poling (BT03p4)

Figure 4.12: In-plane PFM signal of poled BT samples (BT03p1-BT03p4) before soaking.

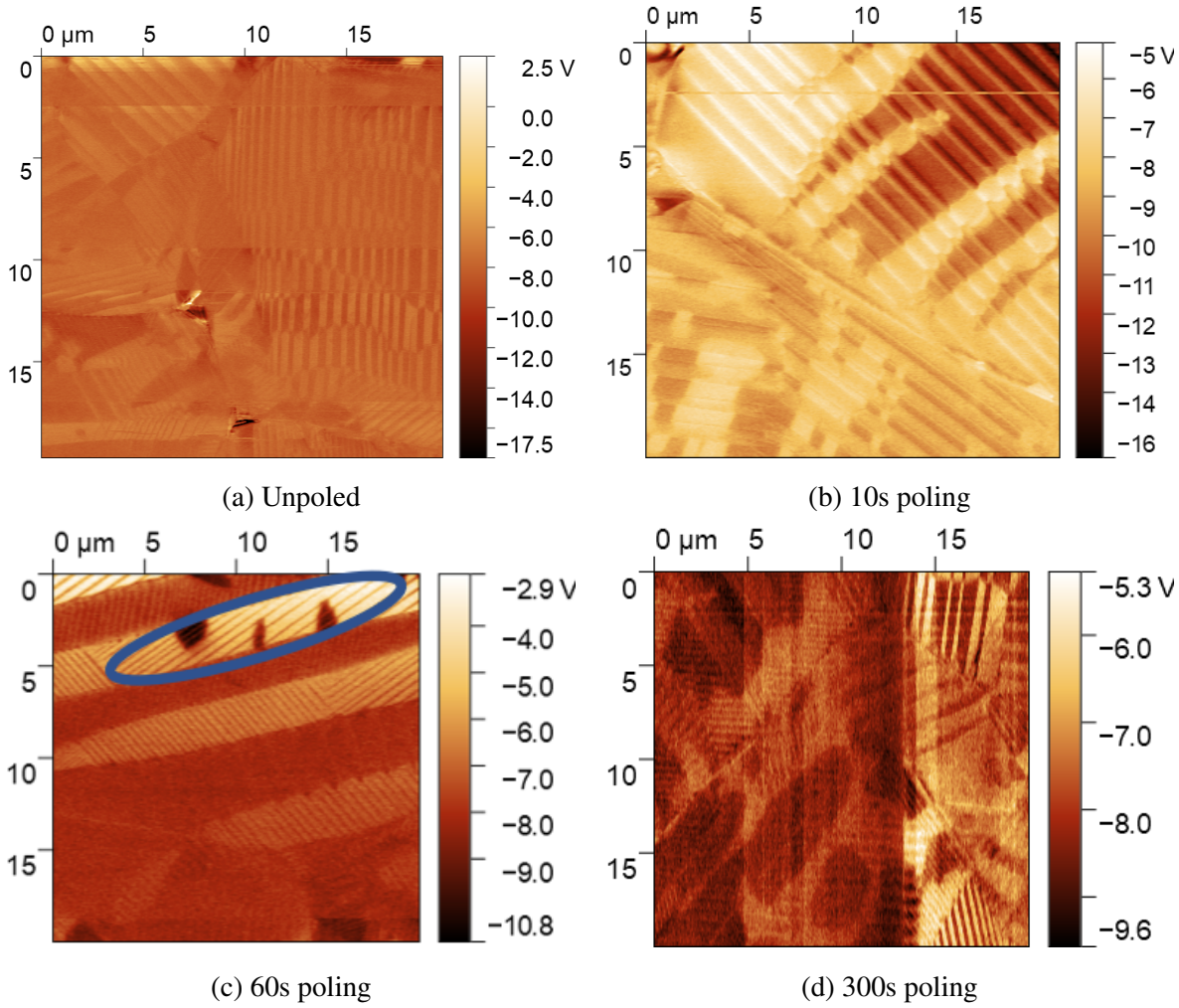

(a) Unpoled

(b) 10s poling

(c) 60s poling

(d) 300s poling

Figure 4.13: Cropped PFM in-plane signal of poled BT samples (BT03p1-BT03p4) before soaking.

The out-of-plane signal shows the polarization in the out-of-plane direction and the results are presented in Figure 4.14. The figure presents cropped images of a 20x20 μm^2 area. The out-of-plane signal was obtained from the same scanned area as the in-plane signal, seen in Figure 4.13, and these images can therefore be compared. The general domain structure was similar for the in-plane and out-of-plane signals. However, the stripe formation seen for the 60-second poled sample in the out-of-plane PFM image, shown in Figure 4.14c inside the blue oval, is more visible than the in-plane-signal in Figure 4.13c. Due to PFM images showing relative values, comparing then in-plane and out-of-plane signals can be challenging. No clear trend in the domain size for increased poling for Figure 4.13 and Figure 4.14 was observed.

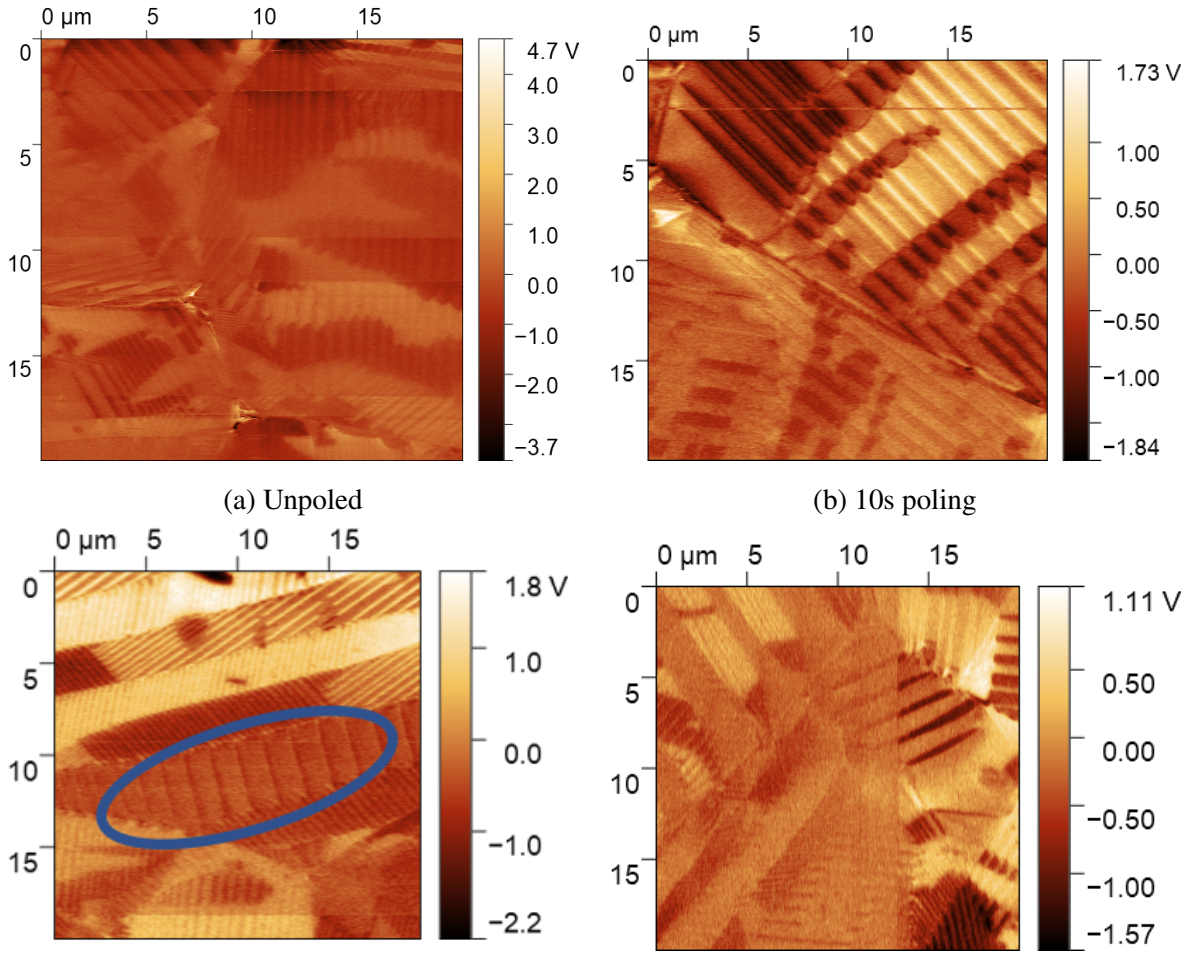

(a) Unpoled

(b) 10s poling

(c) 60s poling

(d) 300s poling

Figure 4.14: Cropped PFM out-of-plane signal of poled BT samples (BT03p1-BT03p4) before soaking.

4.5 Soaking study

After the samples had been poled and characterized with SEM, PFM, XRD, piezoelectric measurements, and optical microscope, the barium titanate pellets were soaked in either simulated body fluid or ultrapure water. The full overview of the soaking parameters is given in the experimental section in Table 3.9. The main goal of soaking the pellets in ultrapure water was to create a simplified *in-vitro* study, where the domain structure and leaching behavior of barium titanate were examined. Soaking BT in simulated body fluid leads to a more complex *in-vitro* study where the target is to observe the precipitation on the surface and how the electrical poling will affect this.

4.5.1 pH

After the BT pellets had been soaked, the pH of the soaking media was measured at two different temperature intervals. The pH was measured right after the vessel was removed from the environmental chamber (liquid temperature, T = 27-30 °C) and when the soaking media reached room temperature (T = 22-24 °C). The results of the pH measurements for the SBF solution are given in Table 4.3. The pH did not change a lot for the SBF, due to it being a buffer solution.

Table 4.3: pH of the SBF after soaking. The pH values are measured right after the solution was removed from the heating cabinet and after the solution had reached room temperature. A blank sample of SBF without a BT pellet soaked was placed and taken out of the heating cabinet following the same time interval.

Time soaked (poling time)	pH at 27-30 °C	pH at 22-24 °C
Unsoaked	7.57	7.65
Blank (1 hour)	7.57	7.67
1 hour (non-poled, 10sec, 60sec, 300sec)	7.59, 7.58, 7.58, 7.59	7.70, 7.69, 7.68, 7.68
Blank (24 hours)	7.56	7.62
24 hours (non-poled, 10sec, 60sec, 300sec)	7.53, 7.53, 7.52, 7.54	7.60, 7.62, 7.58, 7.61
Blank (5days)	7.62	7.66
5 days (non-poled, 10sec, 60sec, 300sec)	7.58, 7.58, 7.58, 7.58	7.65, 7.67, 7.60, 7.66

The results from the pH measurements of the UPW are shown in Table 4.4 and the pH values at room temperature are presented in Figure 4.15. The figure shows an increase in the pH for all samples and all soaking times when compared to the blank sample. The blank sample showed a decreasing pH when compared to the unsoaked sample as well. The UPW containing the unpoled samples increased in pH for the first hour of soaking and decreased back to the initial value after 5 days. The pH of the UPW for the poled samples did not change a lot, but the 60s

poled and 300s poled samples decreased slightly for the first hour and then increased until 5 days of soaking, reaching approximately the initial value.

Table 4.4: pH of the ultrapure water after soaking. The pH values are measured right after the solution was removed from the heating cabinet and after the solution had reached room temperature. A blank sample of ultrapure water without a BT pellet soaked was placed and taken out of the heating cabinet following the same time interval.

Time soaked (poling time)	pH at 27-30 °C	pH at 22-24 °C
Unsoaked	6.15	6.20
Blank (1 hour)	5.78	5.85
1 hour (non-poled, 10sec, 60sec, 300sec)	6.93, 6.25, 5.97, 5.98	7.10, 6.28, 6.07, 6.05
Blank (24 hours)	5.77	5.76,
24 hours (non-poled, 10sec, 60sec, 300sec)	7.23, 6.48, 6.14, 6.24	6.66, 6.21, 6.10, 6.17
Blank (5days)	5.94	5.96
5 days (non-poled, 10sec, 60sec, 300sec)	6.38, 6.35, 6.50, 6.23	6.14, 6.19, 6.38, 6.16

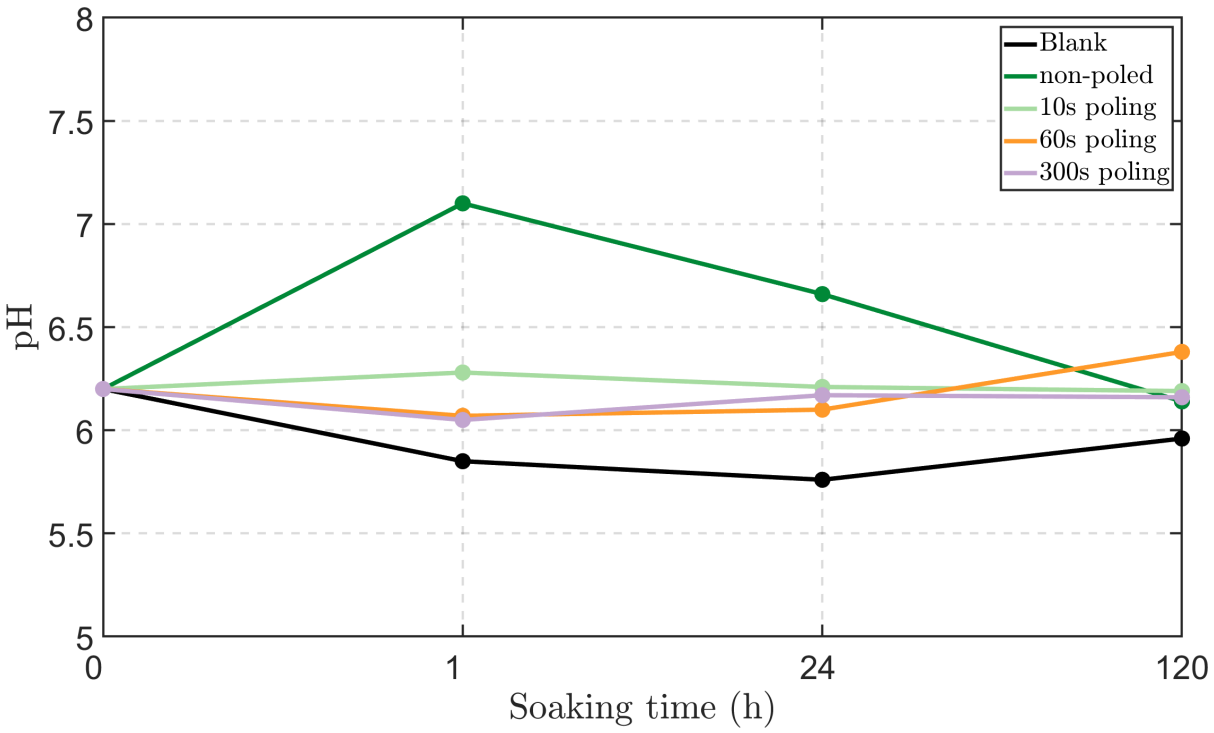

Figure 4.15: pH measured at room temperature of the ultrapure water after soaking.

4.5.2 Surface roughness

An indication of leaching can also be detected by studying the change in surface roughness after soaking. Figure 4.16 displays the surface roughness of all samples after soaking. When compared to the S_A-values of the unsoaked samples given in Figure 4.9, a general increase can be observed.

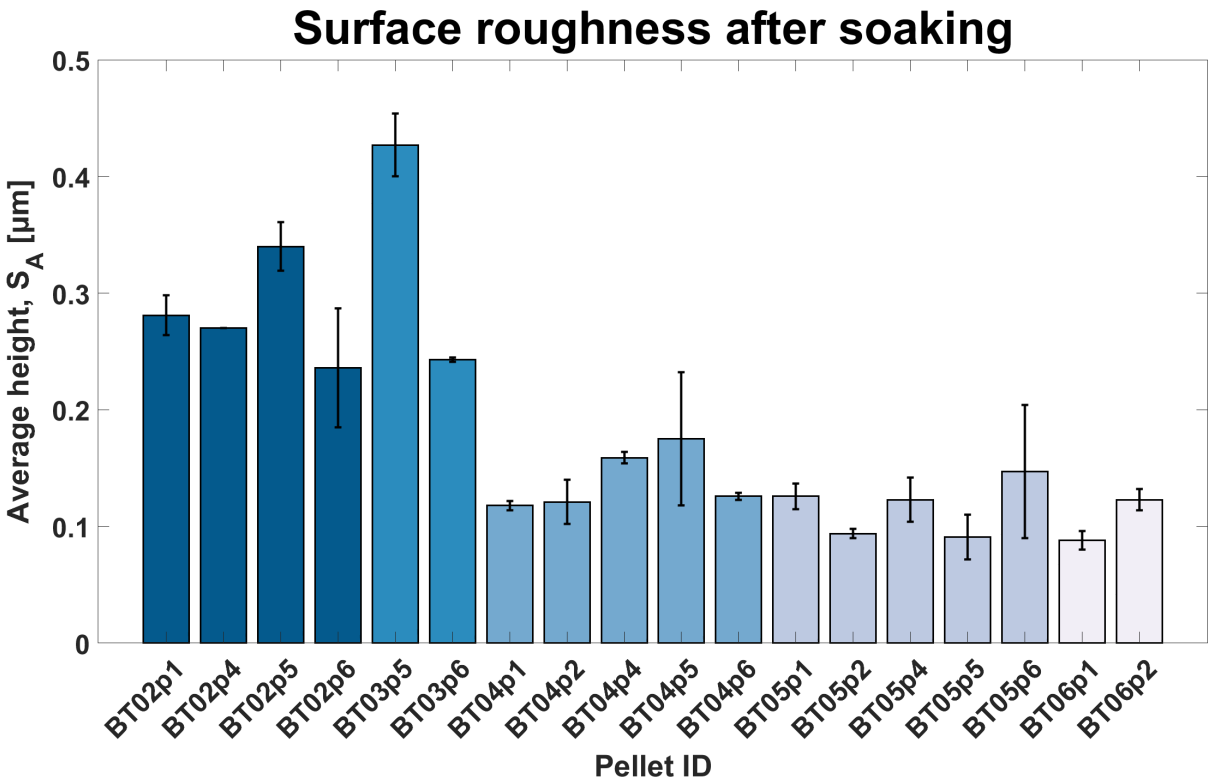

Figure 4.16: Surface roughness after soaking

This general increase in surface roughness of the BT pellets after soaking can be further studied by observing Figure 4.17. The plot compares the average surface roughness of the BT pellets before soaking and after soaking for both UPW and SBF samples, without considering the poling state. As shown in Figure 4.9 the BT pellets initially had varying S_A-values and therefore the exact values are not of interest, but the differences between before and after soaking are important. As can be seen in Figure 4.17, the surface roughness increased after soaking for all parallels of different soaking times and soaking media. The standard deviation also increased after soaking for all parallels. The surface roughness increased most for the 1-hour soaked samples and then increased less for the 24-hour soaked samples, and even less for the BT samples soaked for 5 days. The 1-hour soaked samples also had the largest standard deviation.

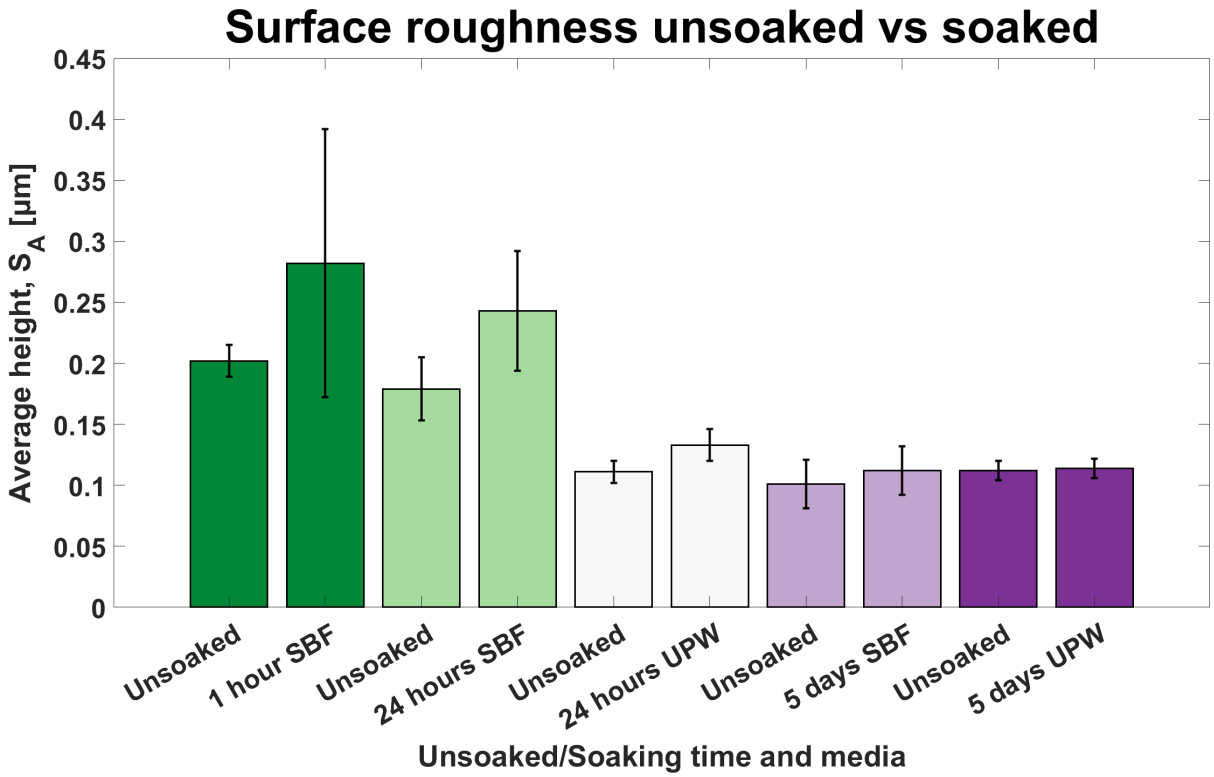

Figure 4.17: Surface roughness before soaking vs after soaking

Figure 4.18 shows the average surface roughness of barium titanate pre and post-soaking with respect to poling. The average S_A-values are calculated by using the results for all soaking times. As described earlier, the soaked samples experience an increase in surface roughness, but there does not seem to be a clear trend with respect to poling. The non-poled samples show a large standard deviation after soaking.

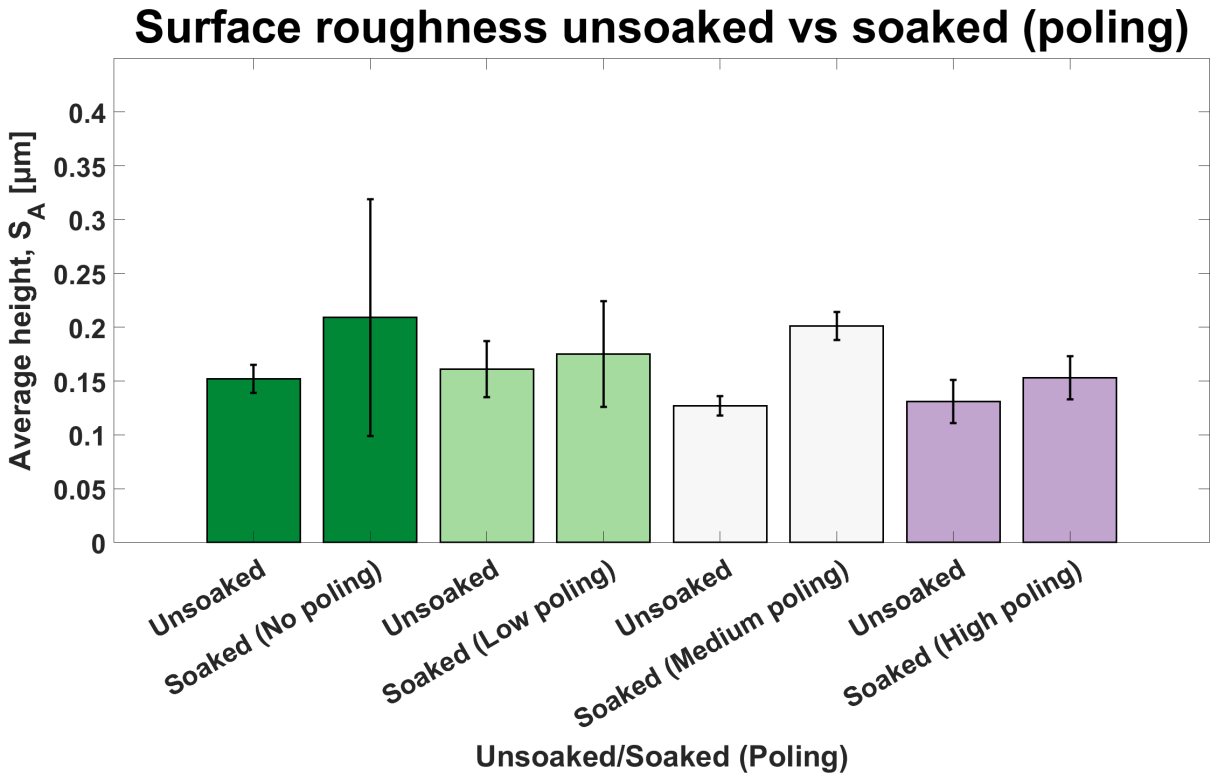

Figure 4.18: Surface roughness before soaking vs after soaking with respect to poling.

4.5.3 Phase purity

The phase purity and structural changes of barium titanate after soaking were investigated using XRD. The XRD diffractograms for the non-poled and high-poled soaked samples in SBF and UPW, for every soaking time, are presented respectively in Figure 4.19 and 4.21. By comparing with the unsoaked sample (black line) there is no substantial change in the XRD diffractograms after soaking for the SBF-soaked and UPW-soaked samples.

SBF

Figure 4.19 shows small unidentified peaks at around $2\Theta = 28 - 29°$ in almost all of the diffractograms. There was no clear trend for these peaks in conjunction with soaking time or poling. The peaks at around $2\Theta = 22°$ and $2\Theta = 44 - 46°$ show some change in the peak shape for the different samples. In general, for the poled samples, the left-hand side of the 22° and 44-46° peaks has a higher intensity compared to the right side of the peak. The unpoled samples show varying peak shapes. The unpoled 1-hour and 24-hour soaked samples have a higher intensity on the right side of the peaks, while the unpoled unsoaked and 5-day soaked samples have a higher intensity on the left side of the peaks. This is seen in more detail for the 22° peak in Figure 4.20.

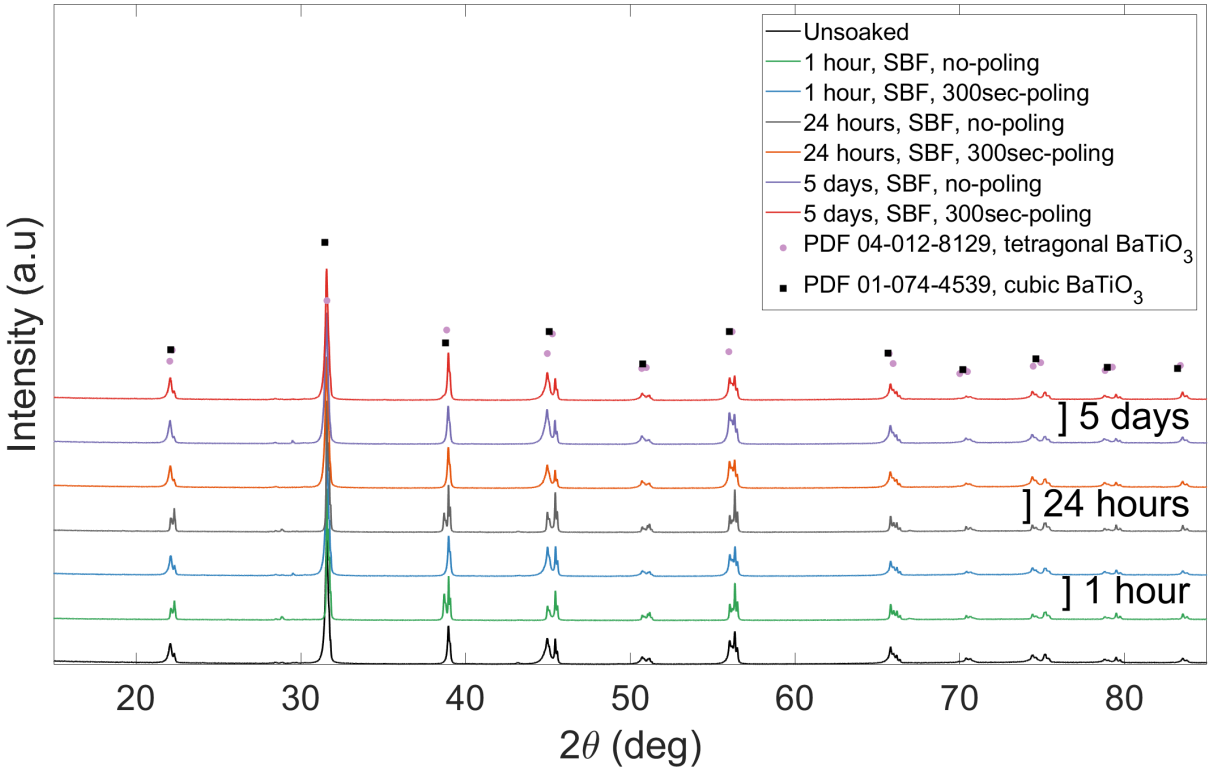

Figure 4.19: XRD diffractograms of the non-poled and high-poled BT pellets soaked in SBF. The XRD diffractogram of an unsoaked BT pellet is also added as seen in the black graph.

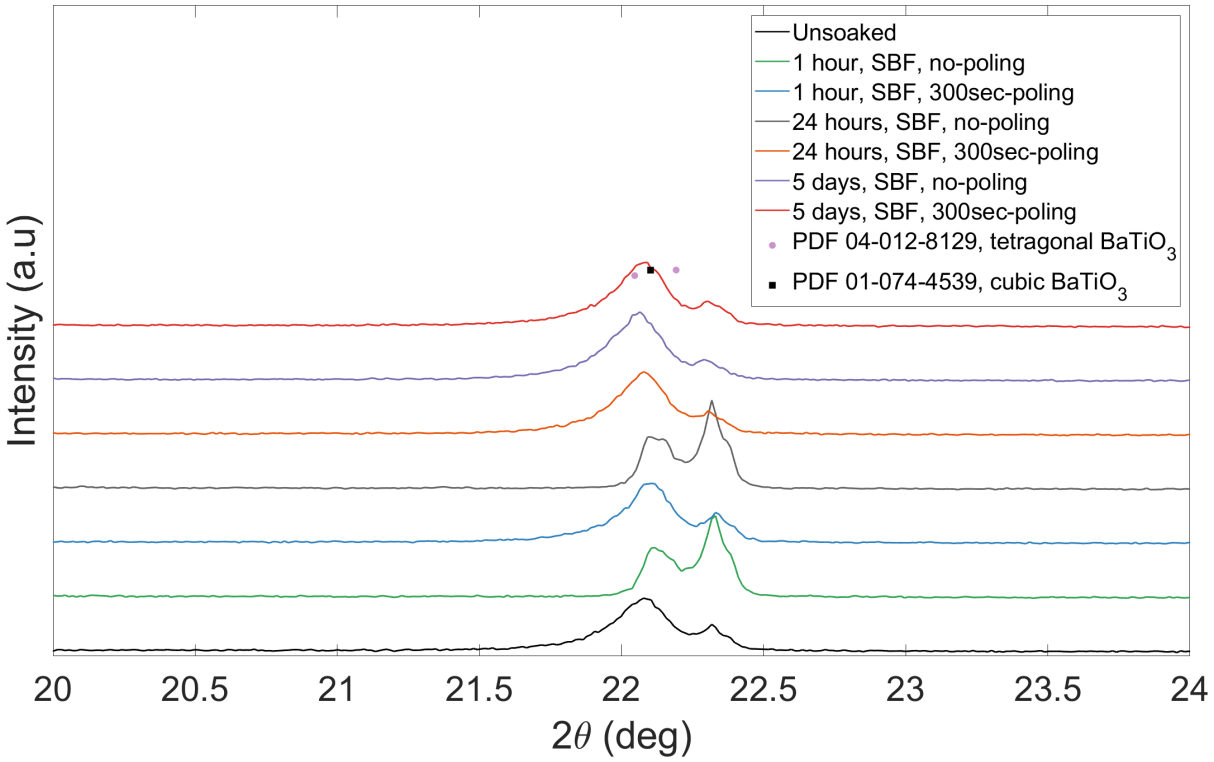

Figure 4.20: Zoomed in XRD diffractograms around the 22° peak, of the non-poled and high-poled BT pellets soaked in SBF. The XRD diffractogram of an unsoaked BT pellet is also added as seen in the black graph.

UPW

Figure 4.21 shows the XRD diffractograms for the BT samples soaked in UPW. The XRD diffractograms of the poled 5-days soaked (red line) and poled 24-hours soaked (orange line) samples, show a similar trend as the poled SBF-soaked samples as shown in Figure 4.19. The left side of the peaks at 22° and 44-46° is dominant for the poled samples. However, the XRD diffractogram of the poled 1-hour soaked sample is an outlier. The right side of the peaks at 22° and 44-46° is dominant, which is a similar peak shape as the unpoled samples.

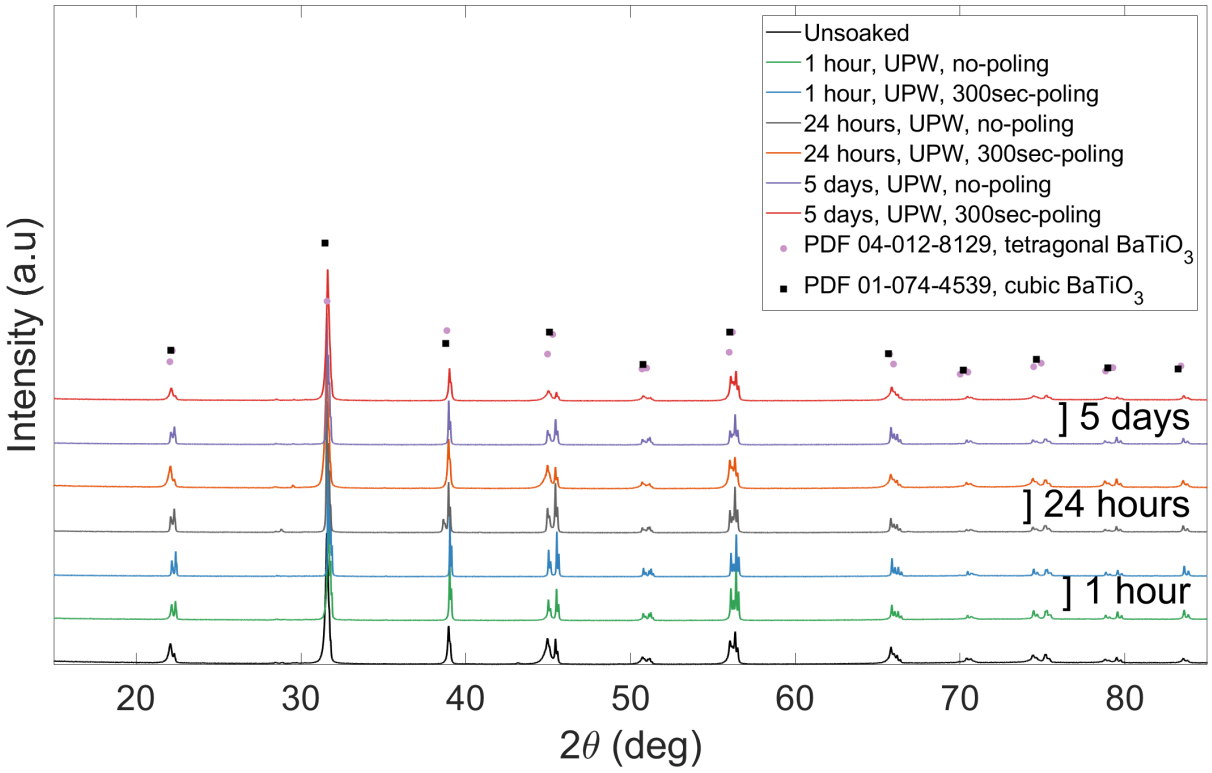

Figure 4.21: XRD diffractograms of the non-poled and high-poled BT pellets soaked in UPW. The XRD diffractogram of an unsoaked BT pellet is also added as seen in the black graph.

4.5.4 Domain structure

Figure 4.22 shows the out-of-plane PFM images for the UPW-soaked BT pellets. The reason for only presenting the out-of-plane PFM signals after soaking was due to the material being poled in this direction, and therefore this signal was of most interest. The images are conducted on the same pellets as before soaking and the results can therefore be compared to Figure 4.14. However, the images show poor quality, especially for Figure 4.22c and 4.22d. As explained in subsection 3.2.4, the samples were cleaned with acetone, ethanol (96%), and methanol (70%) before conducting PFM measurements. Nonetheless, the PFM measurements showed signs of dirt on the samples resulting in the tip collecting dirt and giving poor resolution for the following measurements. Due to the limited amount of resources and time, the PFM tip could not be changed during the measurements. Figure 4.22a shows small stripe-like domains in different directions. The grain boundary in the BT sample can also clearly be seen as the line from the top right to almost the bottom left of the PFM image in Figure 4.22a. The stripe formation changes direction through the grain boundary, going from being tilted slightly to being vertical with the image direction. A similar stripe formation can also be seen for the low-poled sample in Figure 4.22b. The stripes do not change direction throughout the sample, but change size from being larger on the right side of the image and then decreasing towards the left-hand side.

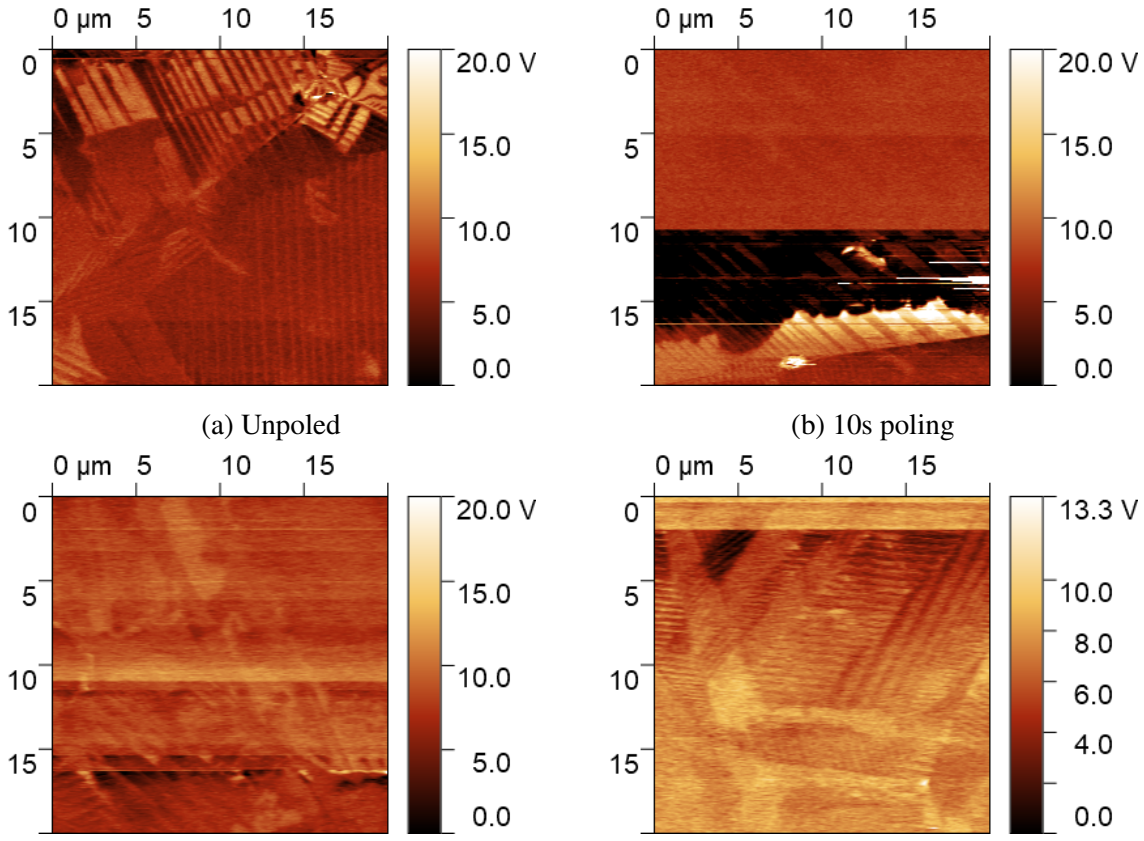

(a) Unpoled

(b) 10s poling

(c) 60s poling

(d) 300s poling

Figure 4.22: Cropped PFM out-of-plane signal after soaking in UPW.

4.5.5 Microstructure after soaking in UPW

The microstructure of the unpoled samples soaked in UPW was studied using SEM. The results are shown in Figure 4.23, and it only shows the unpoled samples soaked for 24 hours and 5 days. The reason for not showing the sample soaked for 1 hour, is due to the pellet being used for PFM analysis. The results can be compared with the microstructure of the unsoaked BT samples, shown in Figure 4.3. The SEM images in Figure 4.23 do not show any charging and the grain boundaries were not as prevalent compared to before soaking. The microstructure after soaking shows some porosity.

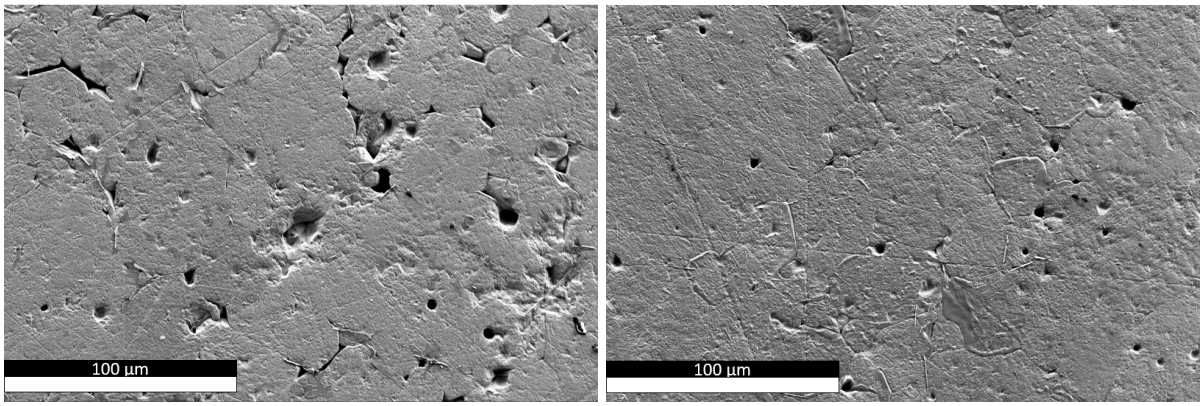

(a) 24 hours soaking (b) 5 days soaking

Figure 4.23: SEM images presenting the microstructure after 24 hours (a) and 5 days (b) of unpoled BT pellets soaked in UPW.

EDS data of an unpoled sample soaked in UPW for 5 days are presented in Figure 4.24. The mapping showed some contamination of carbon. This is seen by the overlap of the dark areas in Figure 4.24a and the green areas in Figure 4.24b. It most likely stems from the carbon sputtering. As explained in the experimental section, the samples were sputtered with carbon before performing SEM measurements, to remove the effect of charging. When comparing the EDS maps for barium and titanium it may indicate a larger amount of titanium than barium on the surface, but due to the EDS spectra of these two elements sharing characteristic x-ray energies, it is challenging to compare these two EDS maps with each other.

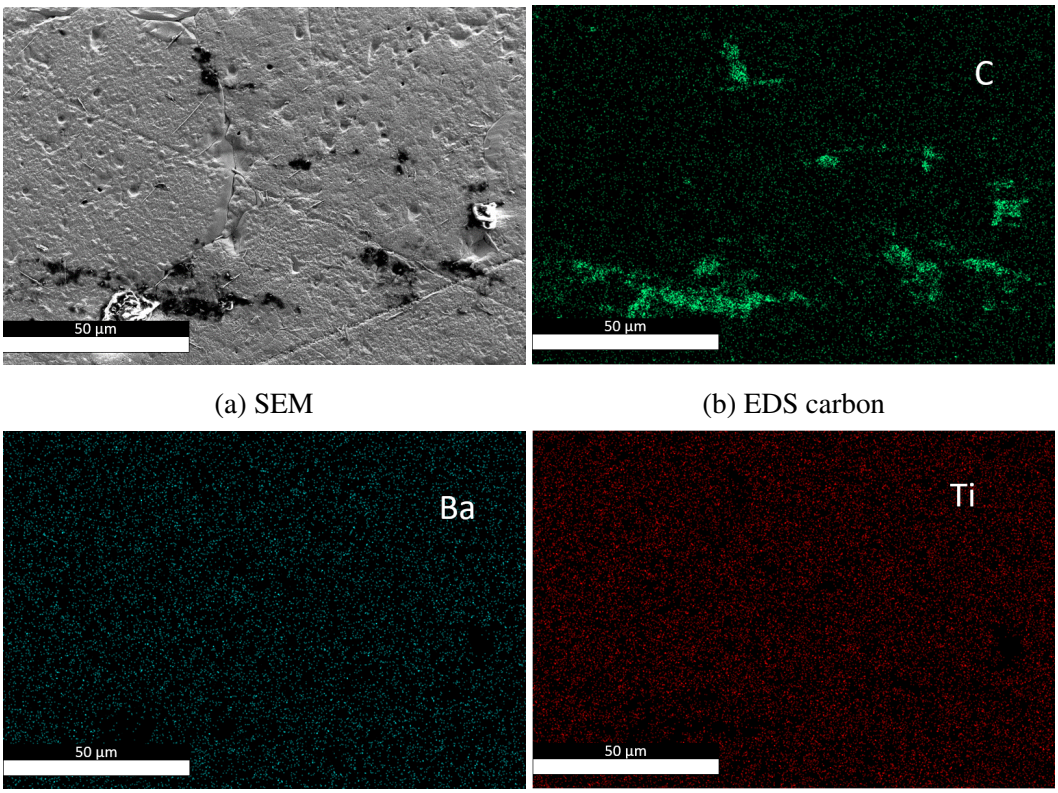

(a) SEM (b) EDS carbon

(c) EDS barium (d) EDS titanium

Figure 4.24: EDS maps of an unpoled BT sample soaked in UPW for 5 days

4.5.6 Precipitation after soaking in SBF

The main reason for conducting a soaking study of barium titanate in SBF was to study the effect of poling and soaking time on the precipitation of calcium phosphate. As explained in section 2.7, an increased surface charge is believed to increase the CaP precipitation on ceramic materials and also increase the *in-vivo* bioactivity.

Weight change

The precipitation after soaking, was first investigated by measuring the weight change. Figure 4.25 shows a small change in the weight for the BT samples soaked in SBF for different soaking times and poling states. The weight of the poled samples decreased slightly until 1 day of soaking, before increasing again after 5 days of soaking. The weight of the unpoled samples decreased for 1 hour of soaking and increased up until reaching 1 day, before the weight decreased again, reaching under the initial weight. This weight change is less than 0.2 wt% and is therefore a marginal change, which it is difficult to draw concluding remarks from.

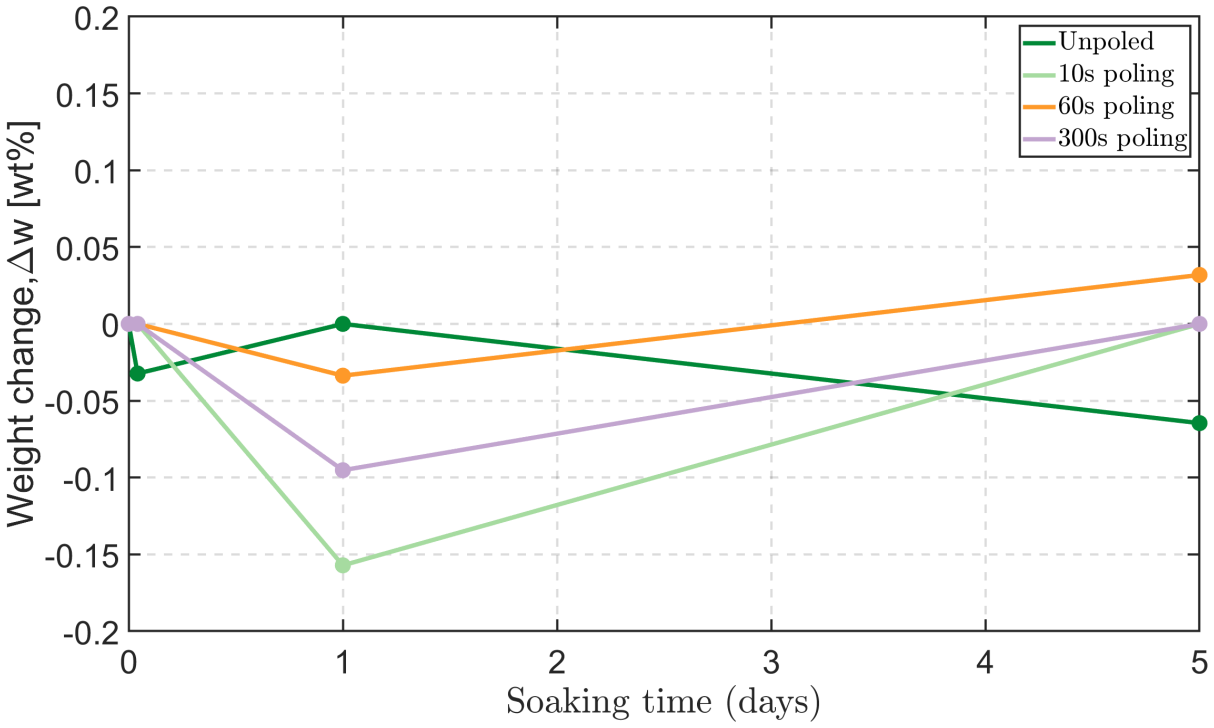

Figure 4.25: Weight change for the samples soaked in SBF.

Microstructure

By further studying the BT samples soaked in SBF, using SEM, some possible correlations between poling time, soaking time, and precipitation were revealed. Figure 4.26 compares the surface of the BT pellets soaked in SBF for 1 hour with different poling states. Figure 4.27 and 4.28 on the other hand presents the SEM micrographs of the BT pellets soaked in SBF for respectively 24 hours and 5 days. For the barium titanate pellets soaked in SBF for 1 hour and 24 hours a substantial precipitation was only observed for the high-poled samples. This is seen in Figure 4.26c and 4.27c as a 15-25 µm large crystal placed on top of the surface. A more detailed image of the precipitate for the 24-hour soaked sample is shown in Figure 4.27d and reveals a cubic-like crystal. The BT samples that were soaked in SBF for 5 days all showed substantial precipitation, even for the unpoled sample. The precipitates on the 5 days-soaked samples were larger in scale and both a large white crystal and irregular-shaped precipitates were observed. A zoomed-in image of the irregular-shaped and undefined precipitate for the 5-day-soaked sample is shown in Figure 4.28d. A clear trend between soaking time, poling, and precipitation was discovered.

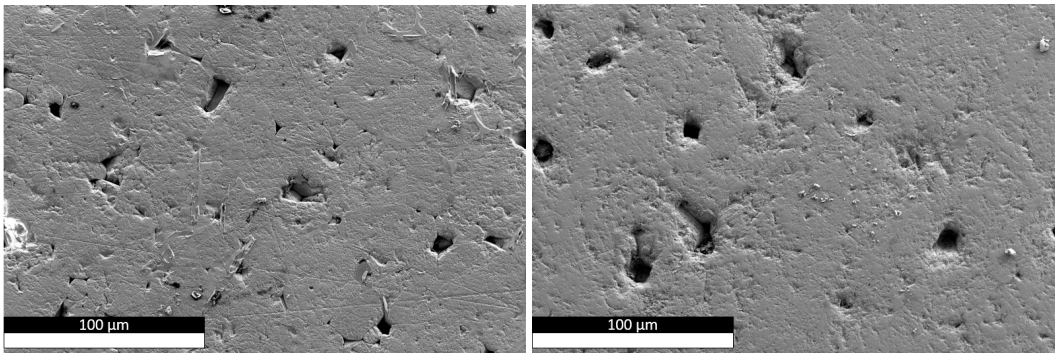

(a) Unpoled (b) 10sec poled

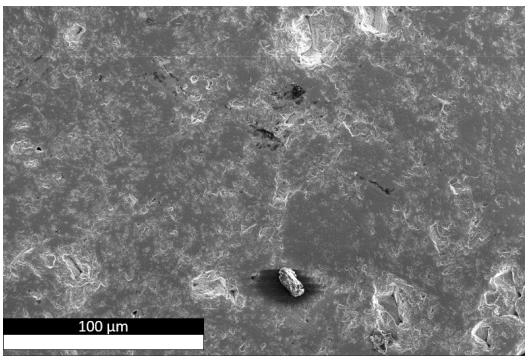

(c) 300sec poled

Figure 4.26: SEM images of the BT samples soaked for 1 hour in SBF.

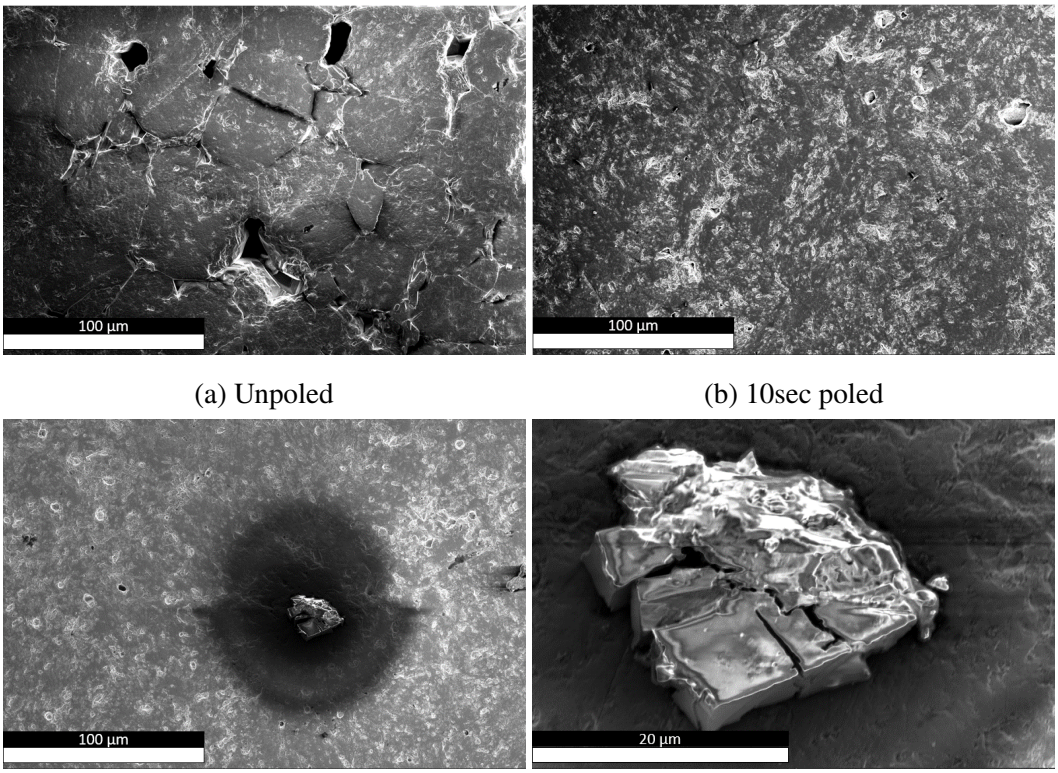

(a) Unpoled (b) 10sec poled

(c) 300sec poled (d) 300sec poled zoomed

Figure 4.27: SEM images of the BT samples soaked for 24 hours in SBF.

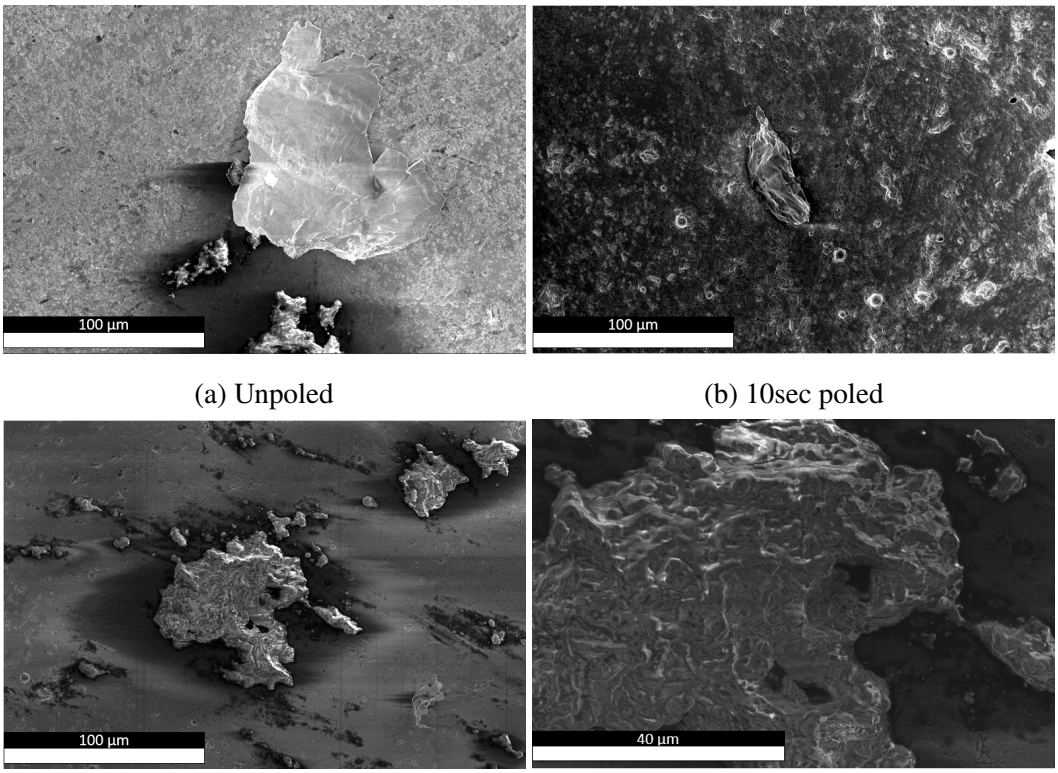

(a) Unpoled (b) 10sec poled

(c) 300sec poled (d) 300sec poled zoomed

Figure 4.28: SEM images of the BT samples soaked for 5 days in SBF.

EDS mapping was conducted to investigate the chemical composition of the different precipitates. The EDS mapping of an area containing both a white crystal and an irregular-shaped precipitate is shown in Figure 4.29a. None of these crystals were observed by the eye, but the SEM showed the large crystal as a bright grey/white color, while the irregular-shaped precipitate had a darker grey color. The EDS maps showed an increased amount of carbon and calcium for the irregular-shaped precipitate. The other elements do not show a clear increase in the amount. The white crystal had less amount of carbon and calcium, but a similar amount of barium, phosphorous, oxygen, and sulfur as the microstructure in the background. The reason for only showing the barium EDS map and not the titanium EDS map is due to the overlapping EDS spectra for the two elements.

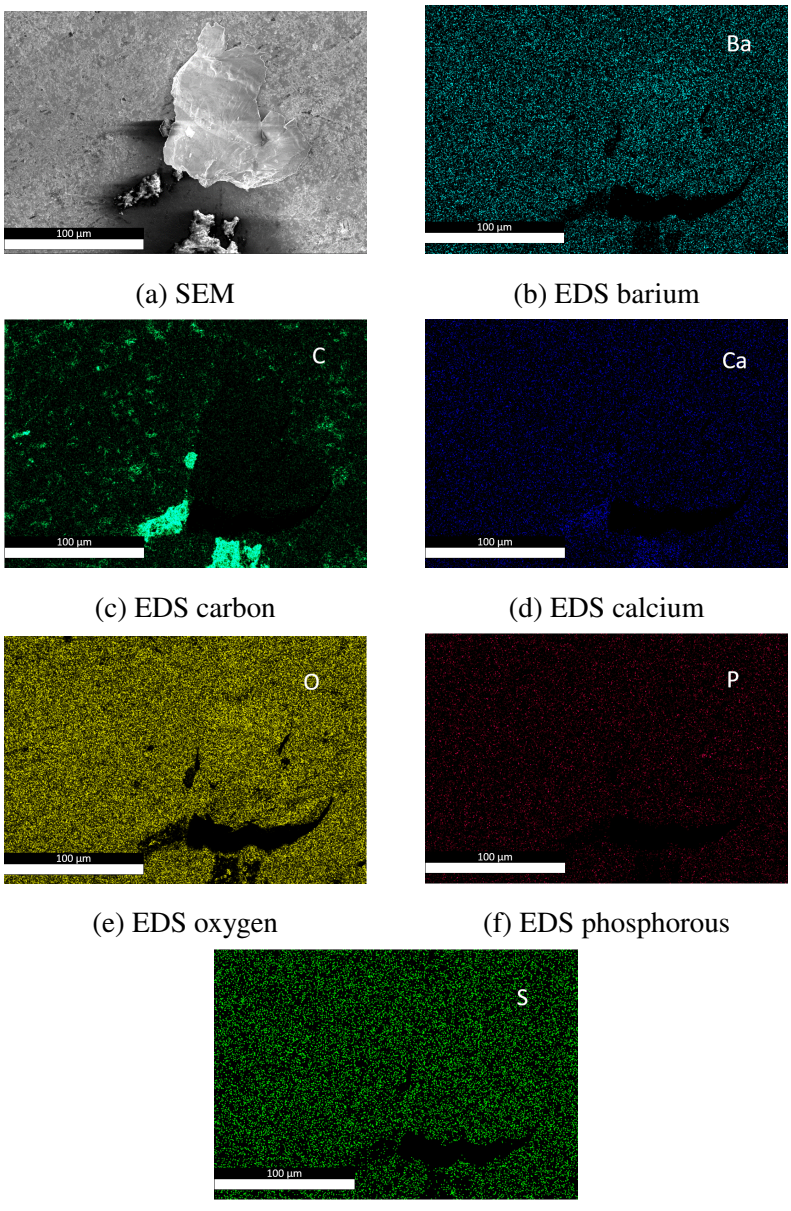

(a) SEM

(b) EDS barium

(c) EDS carbon

(d) EDS calcium

(e) EDS oxygen

(f) EDS phosphorous

(g) EDS sulfur

Figure 4.29: EDS maps of the unpoled BT sample soaked in SBF for 5 days.

4.5.7 Piezoelectric properties

The piezoelectric properties of the material are crucial for the application of barium titanate as a bone implant, and the functional property was therefore studied after soaking in SBF and UPW.

Table 4.5 presents the piezoelectric coefficient, d_{33}, after soaking in SBF and UPW for the non-poled and high-poled samples. The positive and negative values of the samples were not completely symmetrical, due to a calibration error in the Berlincourt meter giving a small shift in the positive values, as seen for all measurements. This also explains why some of the positive d_{33}-values were 0 pC/N. The piezoelectric coefficients for the unpoled samples show similar values before and after soaking, which is observed by comparing Table 4.2 to Table 4.5. The high-poled samples show large piezoelectric coefficient values, ranging from 127 pC/N to 218 pC/N and from -130 pC/N to -222 pC/N. The d_{33}-values for the 5 days soaked samples show the lowest piezoelectric coefficients, but it is a relatively small difference and there does not seem to be a clear linear decline in the d_{33}-value from 1 hour soaking to 5 days soaking.

Table 4.5: d_{33} measurements performed by a Berlincourt meter on soaked and poled samples.

Pellet ID (soaking time, media, poling)	d_{33} [pC/N](positive)	d_{33} [pC/N] (negative)
BT02p1 (1 hour, SBF, no-poling)	5	-10
BT02p6 (1 hour, SBF, 300sec-poling)	194	-200
BT03p5 (24 hours, SBF, no-poling)	0	-5
BT04p6 (24 hours, SBF, 300sec-poling)	218	-222
BT05p5 (5 days, SBF, no-poling)	0	-6
BT06p2 (5 days, SBF, 300sec-poling)	183	-190
BT03p1 (1 hour, UPW, no-poling)	4	-3
BT03p4 (1 hour, UPW, 300sec-poling)	135	-142
BT04p1 (24 hours, UPW, no-poling)	4	-7
BT04p4 (24 hours, UPW, 300sec-poling)	138	-144
BT05p1 (5 days, UPW, no-poling)	0	-9
BT05p4 (5 days, UPW, 300sec-poling	127	-130

SBF

Figure 4.30 shows the piezoelectric properties of the unpoled samples after soaking in SBF for the different soaking times. The 5-day soaked sample (BT05p5) showed a symmetrical and slim characteristic ferroelectric hysteresis loop. The 1-hour soaked sample (BT02p1) showed a flatter loop with less distinct hysteresis behavior. The BT sample soaked in SBF for 24 hours (BT03p5) shows a broadening of the curve and an increase in the remnant polarization. The displacement curves all have a butterfly shape, and the peak displacement increased for a longer soaking time. The peak displacement of BT02p1 and BT03p5 was between 0.03-0.04%, while the 5-day soaked sample (BT05p5) showed a peak displacement close to 0.07%.

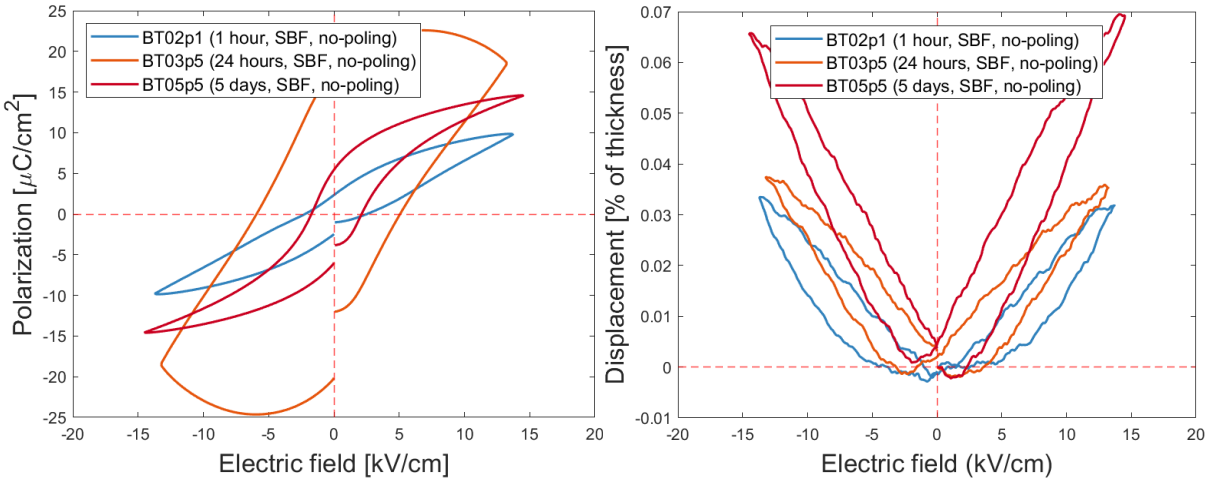

(a) Polarisation curves

(b) Strain curves

Figure 4.30: Piezoelectric measurements after soaking in SBF for the unpoled samples.

The piezoelectric properties of the high-poled samples soaked in SBF are presented in Figure 4.31. All polarization loops show a similar hysteresis behavior which is shifted along the x-axis creating a non-symmetry around the y-axis. The loops are shifted towards higher positive electric field values on the x-axis. The displacement curves show similar behavior as the unpoled samples (BT02p1, BT03p5, BT05p5), with increased peak displacement for increased soaking. The displacement curve for the BT02p6 (1 hour soaked) sample, show a small bump at the highest negative electric fields, which could be due to dielectric discharge.

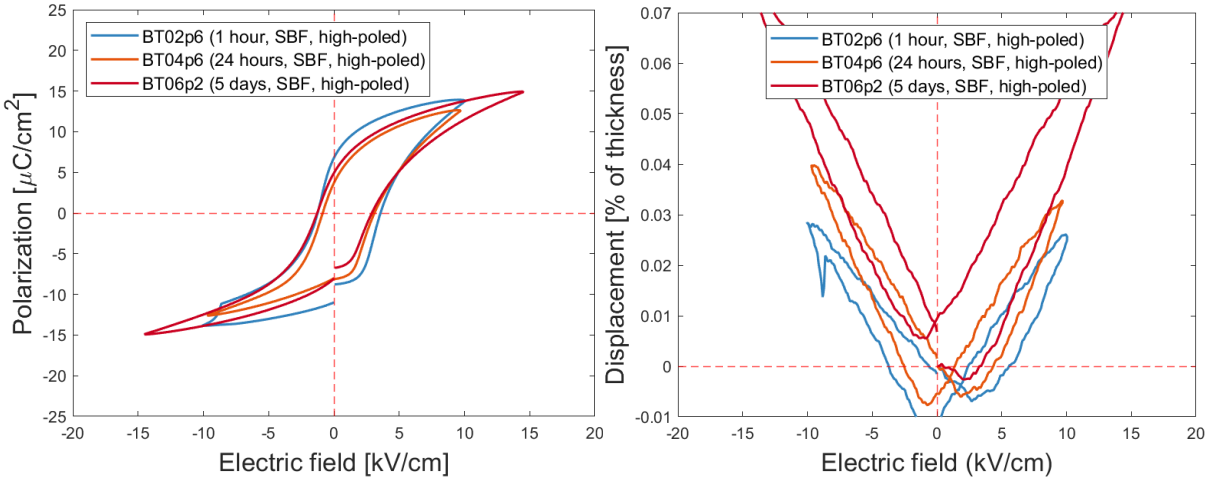

(a) Polarisation curves

(b) Strain curves

Figure 4.31: Piezoelectric measurements after soaking in SBF for the high-poled samples.

UPW

Figure 4.32 and Figure 4.33 show the piezoelectric properties of the barium titanate pellets soaked in UPW for the different soaking times of respectively the non-poled and high-poled samples. The non-poled barium titanate pellets soaked in UPW show symmetrical hysteresis loops, except for the 1-hour soaked sample (BT03p1) which has a flatter and less distinct hysteresis behavior and a higher degree of dielectric behavior. The displacement curves all have a butterfly shape. BT03p1 showed a peak displacement of around 0.03%, while BT04p1 showed a peak displacement between of around 0.04%. The 5-day soaked sample (BT05p1) has a peak displacement of around 0.07%.

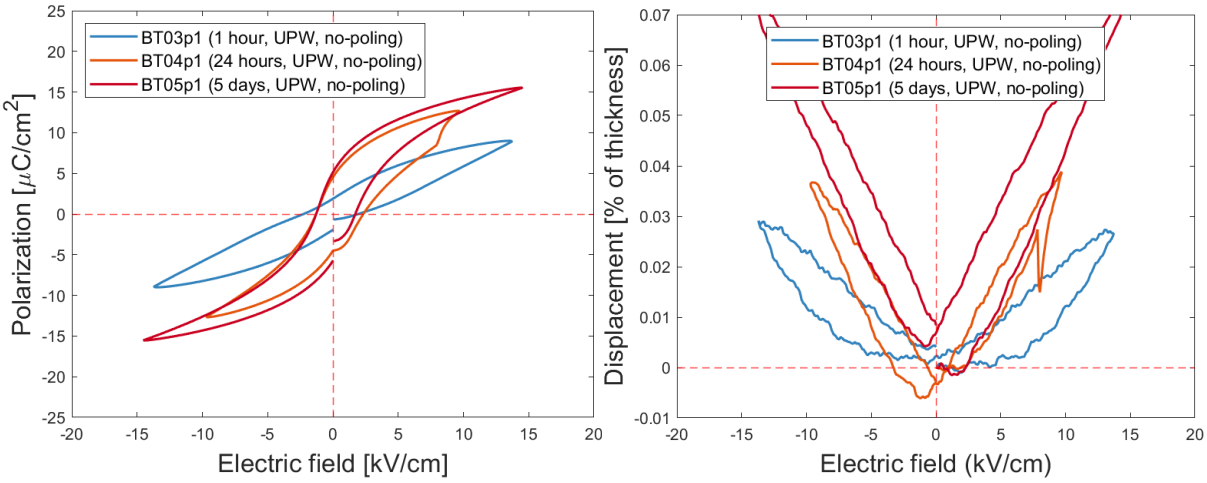

(a) Polarisation curves

(b) Strain curves

Figure 4.32: Piezoelectric measurements after soaking in UPW for the unpoled samples.

The high-poled samples soaked in UPW showed non-symmetrical hysteresis loops at lower voltages, but when applying a 1.5 kV voltage the $BaTiO_3$ pellets showed more symmetrical loops even though the loops were still a bit shifted. For BT04p4 and BT05p4 the loops were shifted towards higher positive electric field values on the x-axis, as seen in Figure 4.33. The polarization loop of the BT03p4 sample was shifted in the opposite direction, probably due to the sample being placed with the positive surface charge pointing upwards during the piezoelectric measurement. The 1-hour soaked sample had a peak displacement of around 0.03%, while the 24-hour and 5-day soaked poled BT samples had a peak displacement between 0.05-0.06%.

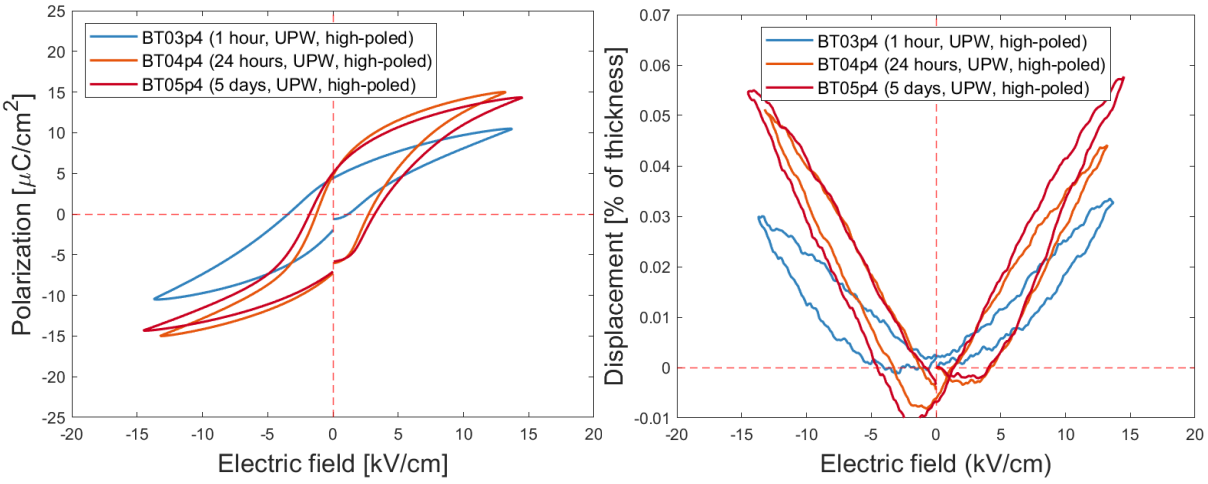

(a) Polarisation curves

(b) Strain curves

Figure 4.33: Piezoelectric measurements after soaking in UPW for the high-poled samples.

5 Discussion

5.1 Optimization of the microstructure

Before characterizing the functional properties of barium titanate and conducting a soaking study, the microstructure and phase purity of the material had to be optimized. An inhomogeneous microstructure could lead to inhomogeneous properties and variable poling state on the material which was unwanted. For barium titanate to be used in a real-life medical application the properties have to be perfected, and it was therefore important to enhance the microstructure properties of BT.

5.1.1 Microstructure

The microstructure of a sintered barium titanate pellet from Batch1 is presented in Figure 4.1a and clearly shows a unimodal grain size distribution of large micrometer-scale grains. On top of the grains, there is observed a darker phase with an elongated shape. These elongated particles could indicate contamination and this was further confirmed with the EDS maps presented in Figure 4.2. This is further discussed in section 5.1.2.

As explained prior, the sintering parameters were decided based on earlier research by the author, and other research articles [1, 47, 48]. The sintering parameters are key to optimizing the microstructure of a material. The microstructure of the 1350 °C sintered BT pellets, for all batches, are relatively homogeneous, with no smaller grains in between the larger ones. This is shown in Figure 4.1a and 4.3. On the other hand, smaller grains trapped between larger ones was a feature on the microstructure of the previous BT pellets sintered at 1300 °C by Holum [1], seen in Figure 4.1b. An increased sintering temperature of +50 °C made a substantial change in the grain growth. The increased sintering temperature changed the grain distribution from bimodal to unimodal by controlled grain growth. As explained in the theory section 2.10.3, the main source of energy to activate and sustain material transport is heat. By increasing the sintering holding temperature, more energy is applied to the system, and diffusion and grain growth can happen on a larger scale. In the theory section, it is described how the smaller fine grains are consumed by the larger ones in the intermediate stage of sintering [46]. This is shown experimentally by comparing Figure 4.1b and 4.1a with the removal of the lighter grey areas, representing fine grains.

A similar change in the microstructure of barium titanate with increased sintering temperature was shown in a research article by Lu et al. from 2010 [53]. Lu's barium titanate synthesis method was comparable to the one in this thesis, by pressing 10 mm discs and using an alumina crucible and sacrificial powder for the sintering. A difference was the holding temperature only being 2 hours compared to 4 hours, for the BT samples sintered at 1335 °C and 1350 °C. Lu's

findings support the results in this thesis, that a bimodal grain size distribution was present when sintering at a lower temperature than 1350 °C, but a unimodal grain size distribution was reached when sintering at 1350 °C [53]. The reason for not increasing the sintering temperature, even more, is the risk of negative effects due to liquid-phase sintering. An increased liquid phase may lead to unwanted excessive grain growth [46]. This was further discussed by Lu et al., which also obtained small peaks in the XRD diffractograms originating from a liquid phase of $Ba_6Ti_{17}O_{40}$ [53]. Excessive grain growth could also lead to poor piezoelectric properties. This is explained in an article by Zheng et al., where the d_{33}-value increases until a 1 µm grain size, and decreases for further enlargement of the grains [54]. A larger grain would lead to larger and more complex ferroelectric domains and domain walls [54]. Larger domains contain an expanded amount of mass, and the movement of these domains is more challenging due to more mass being in motion. Therefore, a ferroelectric material with larger grains will respond less actively to an external electric field and thus decrease the piezoelectric properties.

Another way of removing finer grains is by having a slower cooling rate. This will give the atoms more time to diffuse and rearrange [46]. This will reduce the risk of excessive grain growth when increasing the sintering temperature, and could lead to a higher relative density of the material due to reducing the trapping of pores [46]. As shown in Figure 3.2 the density of the 6 pellet batches is high and the relative density is varying between 94.791%-98.809%. Expanding the cooling time was therefore not necessary. The reason for BT01 having the lowest density may be due to increased contamination, which was successfully removed for BT02-BT06. This is discussed in the following section.

5.1.2 Phase-purity

The EDS maps of aluminum, shown in Figure 4.2, reveal a brighter purple area matching the exact spots of the darker areas in the SEM image (Batch1). A brighter area in an EDS map displays a larger signal of a certain x-ray energy corresponding to a specific element and therefore reveals an enhanced amount of this element. In prior research conducted by Holum, aluminum contamination was discovered [1]. Those EDS scans showed very clear and bright areas, but Figure 4.2 only shows faintly bright areas which could indicate that the aluminum contamination is low and that the darker particles are not a pure aluminum phase. In the research conducted by Holum in 2022, the milling was performed using an Al_2O_3 milling jar which explains a much higher amount of aluminum, compared to the synthesized BT in this thesis where a ZrO_2 milling jar was used for Batch1 [1].

The EDS maps of oxygen and titanium also show a slightly brighter area overlapping the darker particles, which could indicate that the contamination is an oxygen, titanium, and aluminum phase. Due to the overlapping characteristic x-ray energies of titanium and barium, this sec-

ondary phase probably contains barium as well, even though an EDS scan of barium was not shown in the results. During an EDS measurement, characteristic x-rays are emitted from the sample, and when Ba and Ti have overlapping spectra it is arbitrary for the computer software which one gets detected as Ba and Ti, which could create correlation and wrong data if both of the EDS maps were analyzed at the same time. To eliminate the source of aluminum and make sure the majority of the secondary phase was removed, the synthesis equipment for Batch1 was switched out for Batch2 and Batch3. As explained in the theory section 2.10.1, milling is often a source of contamination, and the ZrO_2 milling jar was therefore switched out with a Teflon milling jar.

The reported impurities from Sigma-Aldrich for the precursor materials were also studied. The TiO_2 precursor has a reported aluminum impurity of 116.6 ppm, while $BaCO_3$ has no reported impurity of aluminum. These values are negligibly small and would therefore not be able to create a significant secondary phase on the surface of barium titanate. The microstructure of pellets from Batch2 and Batch3 are presented in Figure 4.3, and show less secondary phase compared to Batch1 (Figure 4.1a). There are still some darker particles on top of the grains, but they are less present and also smaller in size. The aluminum EDS maps for Batch2 and Batch3 detected some aluminum over the entire area, but there were no brighter areas overlapping with the secondary phase, and it was concluded that there was no substantial aluminum contamination on the BT samples for Batch2 and Batch3.

The phase purity was also studied using X-ray diffraction and the results are shown for respectively powder and pellets in Figure 4.4 and 4.5. All XRD diffractograms show a great match with the PDFs for barium titanate, and the diffractograms for the pellets all show tetragonal splitting matching the tetragonal PDF 04-012-8129. This confirms that the stable room-temperature phase of the tetragonal structure ($P4mm$) had been synthesized. The reason for observing splitting in the peaks for tetragonal $BaTiO_3$, and not for cubic $BaTiO_3$ is due to the lattice parameters not being equal anymore. In a cubic unit cell, a = b = c, but for a tetragonal unit cell a = b $\neq$ c. This creates an anisotropy in the crystallographic directions for the tetragonal unit cell, which leads to a small change in the 2Θ-value of the diffraction peaks. The peak at around 45° shows the (200), (020), and (002) peaks. Due to a and b not being equal to c for the tetragonal phase, this creates a splitting in the peak, where the right-hand side of the peak will theoretically remain at twice the intensity value as the left-hand side peak. This is referred to in an article from Zheng 2012 and used as evidence of the tetragonal BT phase [54]. When studying the XRD diffractograms in Figure 4.5, the peak at 45° is split, but does not show double intensity for the right-hand side peak. The reason for this could be due to some defects in the material or the preferred orientation of the grains. This effect is subtle and not substantial for the properties of the material.

There were also observed some small unidentified peaks at around $2\Theta = 28 - 29°$ for the Batch1 pellets, seen in Figure 4.5. These peaks were tried to match with different phases of aluminum, without finding a perfect match. Some of the peaks matched with the PDF 04-013-7798, representing the $Ba_4Ti_{10}Al_2O_{27}$ phase. By changing the synthesis equipment, the peaks declined in intensity and it was concluded that this contamination was almost fully removed and did not affect the properties of the material substantially. This was further confirmed by running a 1-day trial soaking study, where no change in the microstructure or piezoelectric properties of the $BaTiO_3$ sample was observed. The study could therefore move forward to further characterization of barium titanate.

5.1.3 Particle size distribution

To make sure that the BT pellets would have optimized physical properties, such as a high relative density, the calcined powder was studied by performing particle size distribution measurements. In the theory section 2.10.3 it is explained how smaller particles would lead to larger surface energy and increase the driving force of sintering. At the same time, a too narrow distribution of small particles would decrease the packing efficiency, and it is, therefore, important to have particles of different sizes to be able to reach high densities. The three different powder batches have a peak particle size varying between approximately 0.5 - 2 µm and standard deviation varying between approximately 0.3 - 1.5 µm. The three calcined powder batches went through the same milling procedure, but Batch2 and Batch3 used a Teflon milling jar instead of a ZrO_2 milling jar. Zirconia is known for its high hardness, while Teflon is a softer material with great chemical resistance. A decrease in hardness of the milling jar could lead to some less milling of the powder and a slight increase in the particle size as seen for Batch2 and Batch3 in Figure 4.6b and 4.6c. With a decreased hardness of the milling jar, an increase in the standard deviation is also expected and observed by Batch2 and Batch3 showing a broader distribution. Some variation in the particle size distribution can as well stem from the finger-ultrasound bath. The samples were run for 30 seconds in the finger-ultrasound bath, but there was some variation in how quickly the PSD measurement was performed after the initial ultrasound bath. This will have some effect on the grade of agglomeration of the particles, which will affect the peak particle size and standard deviation. Some agglomeration of the particles is observed in the SEM image in Figure 4.7 for Batch2. Overall the calcined $BaTiO_3$ powders showed a unimodal particle size distribution with sufficient particle size and broadness for reaching great physical properties of the sintered pellets.

5.2 Poling effect on domains

One of the goals of this thesis was to study the effect of poling on the precipitation of calcium apatite when soaking barium titanate in SBF. As explained earlier, an increased surface charge on the material is predicted to increase calcium apatite precipitation and the overall biocompatibility of the material. To be able to conduct the poled soaking study, the barium titanate pellets had to go through a preliminary poling study. This study was used to decide the appropriate poling parameters to reach different poling states of $BaTiO_3$. To study the domain structure for the different poling states, the barium titanate material was also characterized using PFM.

5.2.1 Preliminary poling study

The preliminary poling study was performed by poling BT at room temperature using a corona discharge setup at 20 kV for different poling times and then measuring the piezoelectric coefficient using a Berlincourt meter. The results are presented in 4.11 and show a semi-linear increase in the piezoelectric coefficient up until 3 minutes when it starts flatting out. When an electric field is applied to the tetragonal barium titanate, the polarization direction will align with the orientation of the electric field, by a subtle shift of the ions in the unit cell. The poling was performed in the out-of-plane direction, and the approximately same values of the positive and negative d_{33} were observed when flipping the sample 180°. This matches well with theory, due to a flipping of the sample will oppositely switch the polarization direction and hence the surface charge. After 3 minutes of poling, most of the ferroelectric domains had switched polarization direction, and a saturation point was reached. This explains the flattening out of the curve. This behavior is supported by a similar poling study on barium titanate conducted by Bentzen in 2021 [50]. Even though the behavior of the curve is similar, the piezoelectric coefficients in Figure 4.11, are almost on an order of 100 times as large compared to Bentzen's results. Bentzen conducted research on BT thin films deposited by aerosol deposition, and this explains the large difference in the d_{33}-values [50]. For aerosol-deposited thin films, the BT powder is randomly deposited on the substrate resulting in low density and defects, together with tiny grains way below the 1 µm optimum size, resulting in poor piezoelectric properties compared to bulk samples. Another study on more conventionally poled samples was performed by Rotan et al. in 2020 [49]. Calcium and zirconia doped barium titanate (BCZT) reached saturated piezoelectric coefficients already after one minute of poling at 20 kV, using a corona discharge. The reported saturated piezoelectric coefficient was $d_{33} = 421 \pm 21$pC/N [49]. This is around double the saturated d_{33}-value of the poled BT samples in this study, shown in Figure 4.11. Doping is aimed to increase the piezoelectric properties of a material, and this difference in piezoelectric coefficients is therefore excepted.

The preliminary poling study gave great insight into how barium titanate behaves in an elec-

tric field and the chosen poling times for the poled soaking study were 0 seconds, 10 seconds, 60 seconds, and 300 seconds. The reason for choosing these exact values is due to a need of covering a broad range of poling states, and these poling times show great differences in the piezoelectric coefficient. Choosing a poling time longer than 300 seconds did not seem necessary due to the piezoelectric coefficients flattening out after 180 seconds and likely reaching saturation. The reason for choosing 300 seconds instead of 180 seconds was to make sure that saturation is reached for all samples, due to the probable variation in the BT samples. The study also confirms the conclusion of Rotan et al. from 2020, that a corona discharge poling technique can be used on lead-free piezoelectrics without the use of electrodes or insulating liquids [49].

5.2.2 Domain structure

To study the effect of poling on the domain structure of barium titanate, 4 different samples poled to different states, were studied using PFM. The samples were poled out-of-plane and this direction was therefore of most importance for the PFM scans. The samples were later soaked in ultrapure water. The reason for not soaking these samples in simulated body fluid, which would be a more realistic study, is due to the expected precipitation on the surface of BT. PFM is a sensitive characterization method, and small amounts of dirt or a notable variation in the surface topography will lead to poor resolution and in the worst case not being able to study the domains.

A large variation in surface topography was observed in previous work on barium titanate by Holum (2022) [1]. As explained in the experimental section 3.2.4, an additional polishing procedure was implemented for this thesis. This was due to prior research by Holum, showing insufficient optical quality when conducting PFM measurements [1]. An AFM image gathered from previous work by Holum is compared to the AFM image of the barium titanate for this thesis in Figure 5.1. The scanned area is equivalent (20x20 μm^2) and the topography on the surface of the BT sample with no additional polishing varied between 1.3 - 2.5 μm [1]. The surface topography for the BT sample with the additional polishing step, was on the nanometer scale, only varying between 2977 - 3313 nm. The PFM results on the same scanned area are also presented, to easily compare how an increased flattening of the surface successfully resulted in increased resolution in the PFM scans.

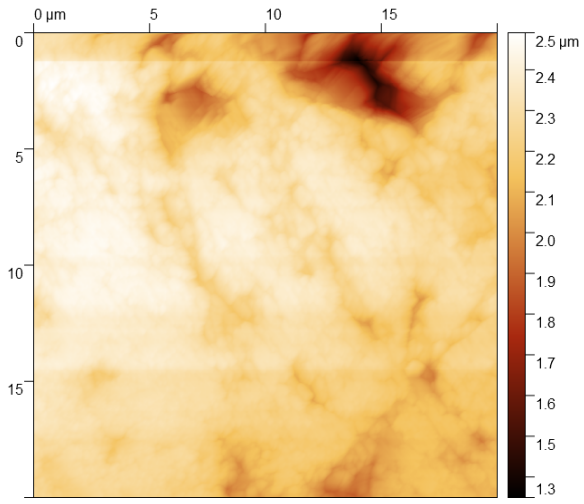

(a) AFM with no additional polishing and a surface finish using SiC 4000 grit size paper.

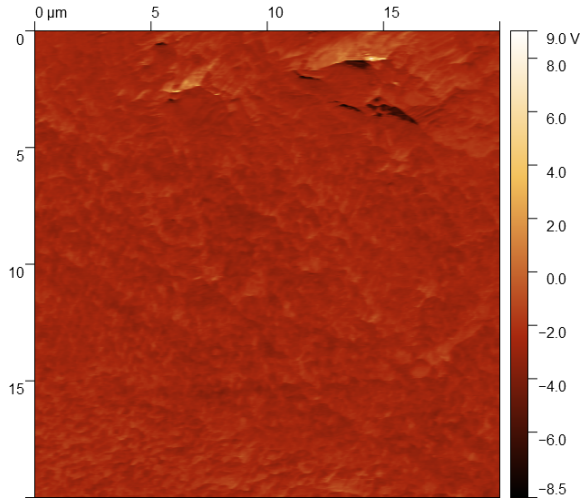

(b) PFM with no additional polishing and a surface finish using SiC 4000 grit size paper.

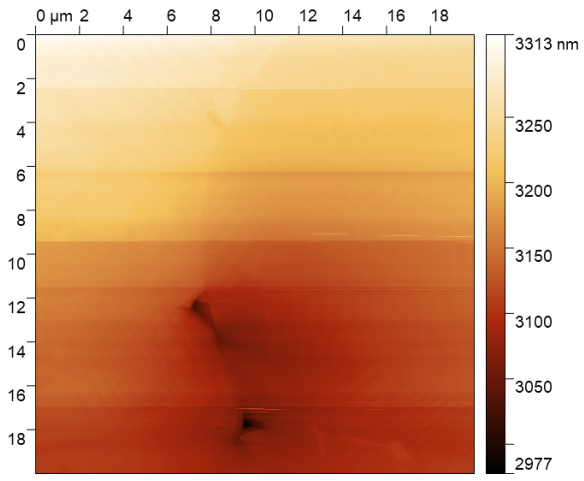

(c) AFM with additional polishing and a surface finish using SiO_2 particles.

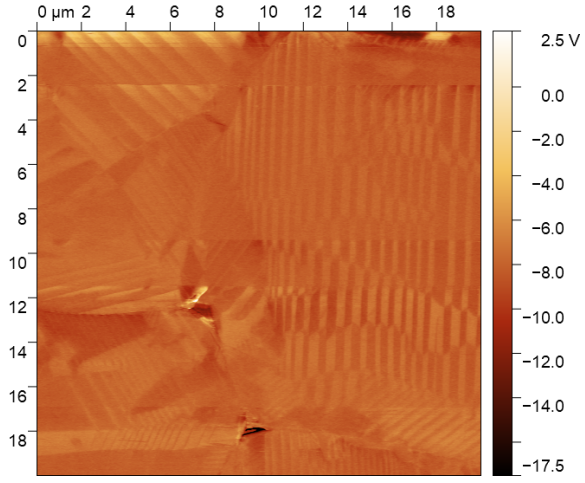

(d) PFM with additional polishing and a surface finish using SiO_2 particles.

Figure 5.1: Comparison of AFM and PFM scans without and with an additional polishing step performed to reduce variation in surface topography. Figure 5.1a and 5.1b are obtained from the project work thesis by Holum [1].

Herringbone domain pattern (90° domain walls) and stripe domain pattern (180° domain walls) are both observed for the different BT samples. As explained in theory section 2.8, this is expected for a ferroelectric material with a tetragonal unit cell, such as $BaTiO_3$. Figure 5.2 presents the domain pattern for the 60-second poled sample (similar to Figure 4.14c), where the herringbone pattern and stripe domain pattern are marked with respectively blue and black circles. Both theoretical models and experimental results have revealed the domain wall motion of 90° domain walls in $BaTiO_3$ when applying electric fields [55]. Therefore, after confirmation of the different domain patterns, the effect of poling on the domain structure was studied.

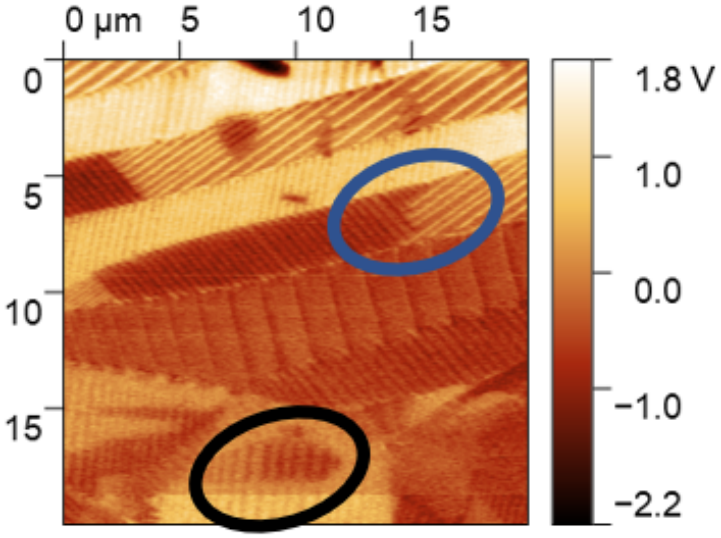

Figure 5.2: PFM of unsoaked BT sample poled for 60 seconds. The blue circle marks a herringbone domain pattern, while the black circle shows a stripe domain pattern.

Figure 2.6 in theory section 2.8 shows the theoretical understanding of how poling should affect the domain structure of a ferroelectric material. Poling will align the polarization direction for the different domains, and the domains already aligned with the electric field will increase in size. In contrast, the other domains will shrink [39]. Therefore, increased poling on the barium titanate samples was predicted to increase the ferroelectric domain size, but this effect was not observed. The stripe domains do not seem to increase in width for increased poling, and the polarization directions are not uniform for the scanned area of the high-poled sample as seen in Figure 4.14d. If one polarization direction would be dominant in the scanned area, there would be one color contrast dominating the PFM image. As seen in Figure 4.14d, there are areas with both darker and lighter red colors and no clear dominant contrast. It is worth noting that the variation in the measured electric voltage, seen as the right y-axis in the PFM images, is less for the high-poled sample (Figure 4.14d) than the unpoled one (Figure 4.14a). This could indicate that the polarization directions are more alike in the high-poled sample than the unpoled one which is as expected, but due to some small defects altering the electric voltage, seen in

white for the unpoled sample, it is challenging to draw a conclusion. It would be plausible to consider that the reason for not seeing any clear increase in the domain size after poling, was due to a too-low electric field being applied. As described in section 5.1.1, the large grains would lead to broader and more complex ferroelectric domains which respond less actively to an electric field. This is also confirmed experimentally by Ghosh et al., concluding that the maximum domain wall motion happened at approximately 2 µm and decreased for larger grains [55]. However, this can not be the case due to the preliminary poling study showing the alignment of polarization orientation through increased piezoelectric coefficient, and the electric field applied for the poling was therefore sufficient (Figure 4.11).

Theory section 2.9 and Figure 2.7 explain that the vertical PFM signal is both affected by the out-of-plane piezoelectric effect, but also the in-plane polarization, due to the buckling effect. The deflection and buckling effect can be difficult to distinguish and a 180° horizontal rotation of the sample will not change the deflection signal but inverse the buckling signal. Therefore it can be used to distinguish the buckling effect from the out-of-plane piezoelectric effect (deflection). By performing data analysis, this could further be analyzed, but due to the complexity and restriction of time, this was deemed unfeasible and beyond the scope of this thesis. This would mean, due to the time restriction, the buckling effect affects the vertical signal. A ceramic material such as $BaTiO_3$ is polycrystalline and would therefore need multiple scanning directions, and this is one of the main reasons why single crystals are often used for PFM. The PFM scans were also conducted on different samples in different areas, which could lead to a large variation in the exact domain structure. For further work, the PFM should be conducted on the same sample, by poling it to a different poling state for each measurement and marking the exact area for investigation. By this experimental procedure, the variation error for each sample and each spot on the surface is removed, which would give a more accurate representation of the change in the domain structure after poling.

5.3 Soaking study in aqueous media (UPW)

5.3.1 Leaching of barium ions

The BT samples showed an indication of leaching during soaking in ultrapure water. The pH change of the soaking media indicated strongly that Ba^{2+} ions had been leached from the BT pellets. The increase of the surface roughness on the surface of BT was strong evidence of dissolution happening during soaking in UPW.

pH

The dissolution of Ba^{2+} ions into a solution is explained in the theory section 2.6 and reaction 2.6 [33]. The reaction equation is also given underneath, as reaction 5.1. The formation of Ba^{2+} ions, also generates an excess outer layer of TiO_2 (s) on the surface and an increased concentration of hydroxide ions in the solution. Hence, studying the fluctuation of the pH during the soaking of barium titanate could give an indication of the potentially ongoing dissolution of barium ions. This study is important for the understanding of the chemical stability of $BaTiO_3$ and to get greater insight into the potential lifetime of a ferroelectric bone implant.

$$BaTiO_3(s) + H_2O \leftrightarrow Ba_2{}^{+}(aq) + TiO_2 + 2\,OH^{-}. \tag{5.1}$$

The pH of the UPW after soaking increased compared to the blank sample, for all parallels run. This is identified in Figure 4.15, and is a strong sign of Ba^{2+} leaching. Nevertheless, the pH did not increase substantially for all the soaked samples compared to their original pH value before soaking. The blank sample decreased in pH for the first 24 hours before increasing until reaching 5 days. This could indicate that the containers were not fully tight and that some CO_2 dissolution occurred. The presence of CO_2 in the atmosphere and in the water has been taken into account in previous soaking studies of $BaTiO_3$ [34, 56]. Dissolution of CO_2 from the air into the solution will usually create a more acidic environment and decrease the pH [57]. The reaction equations taking place when CO_2 is dissolving in water is given in reaction 5.2, 5.3, and 5.4 [57].

$$CO_2 + H_2O \leftrightarrow H_2CO_3 \tag{5.2}$$

$$H_2CO_3 \leftrightarrow H^{+} + HCO_3{}^{-} \tag{5.3}$$

$$HCO_3{}^{-} \leftrightarrow H^{+} + CO_3{}^{2-} \tag{5.4}$$

CO_2 dissolution from the atmosphere is a probable cause of why the pH of the blank sample decreased and was always lower than the UPW vessels containing a barium titanate sample. Even though only a few BT samples experienced a rise in the pH value, some dissolution of Ba^{2+} was probably still present for all samples, but due to the simultaneous dissolution of CO_2 from the air, it outweighed a basic pH change. A simple illustration of this is presented in Figure 5.3.

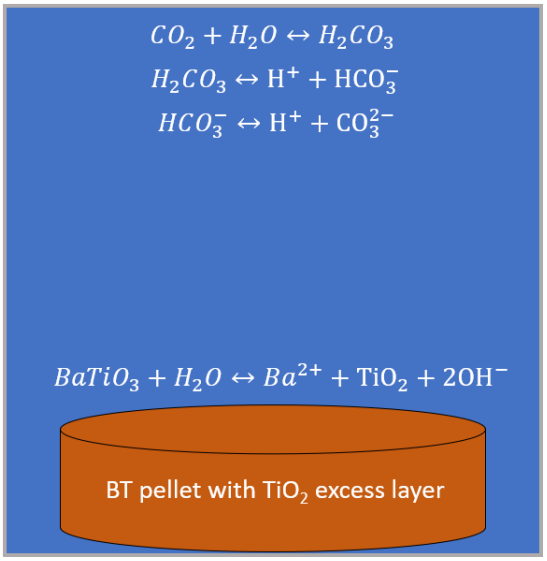

Figure 5.3: An illustration showing a simplified version of what is happening during the soaking of a barium titanate pellet in ultrapure water inside a not fully tight vessel.

When studying the effect of poling on the dissolution of Ba^{2+}, it is noteworthy that the non-poled sample was the only one that increased the pH substantially after 1 hour of soaking. Afterward, it started decreasing until approximately reaching the initial pH value after 5 days of soaking. This could indicate that for the non-poled samples, most of the dissolution happened in the early stage of soaking. After a while, the pH reached back to the initial state, due to the surface of the barium titanate being leached and therefore it could not supply more barium to keep pushing the equilibrium. This is also supported by Neubrand et al. who claimed that the dissolution from $BaTiO_3$ is a surface reaction due to the diffusion of bulk ions being very slow [33]. This general behavior is also supported experimentally by Blanco Lopez, that shows rapid leaching of Ba^{2+} before reaching a plateau in the time frame of hours [34, 35]. A theory by Tripathy et al. explains how the dissolved CO_2 in the water may react with the leached Ba^{2+} and redeposit as $BaCO_3$ on the BT surface and hinder further leaching of Ba^{2+} [56]. This also supports the results in this thesis showing a decrease in the leaching rate of Ba^{2+} for extensive soaking. The suggested reaction equations by Tripathy et al. showing the formation of $BaCO_3$ are given below: [56]

$$Ba_2^+ + CO_2 + H_2O \rightarrow BaCO_3 + 2\,H^+. \tag{5.5}$$

$$2\,H^{+} + CO_3^{2-} + BaTiO_3 \rightarrow BaCO_3 + TiO_2 + H_2O. \tag{5.6}$$

The pH behavior of the poled samples could also indicate a stronger dissolution in the early stages of soaking, even though the pH change is relatively flat. The pH of the blank samples decreased most after 1 hour, and due to the poled-sample not changing pH, a possible explanation is a substantial leaching of Ba^{2+} for the early stage of soaking balancing out the pH. The poled samples have a charged surface which would attract ions and could lead to a screening effect that can reduce the leaching. This is a possible explanation of why the poled samples experienced a small pH change. The BT pellets were placed with the negative surface pointing upwards, and a negative surface could lead to re-adsorption of Ba^{2+} on the surface, leading to a decrease of free barium ions. This is also discussed in a research article by Neubrand et al. from 2000 [33]. The experimental pH data indicates that poling increases the chemical stability of BT, but variations in surface defects or porosities of each sample could also influence the leaching of the surface, by creating a larger effective surface area. Therefore no certain conclusion can be made, but it is a promising sign for further research.

Surface roughness

The surface roughness data further confirms the behavior of increased leaching at the early stage of soaking, before it starts plateauing. Figure 4.17 shows an increased surface roughness for all soaking times, but mostly for the 1-hour soaked samples. The samples experience an initial roughening before an extensive soaking leads to a smoothing of the surface. It is worth noting that the surface roughness of the 1-hour soaked UPW samples is not measured, due to the limitation of the vertical resolution of the optical microscope. The samples were used for the PFM study and therefore had a very flat surface. The BT samples soaked in UPW for 24 hours and 5 days show similar behavior as the SBF-soaked samples, and therefore it is expected that the 1-hour soaked UPW sample would have experienced a similar trend. Initially, it may seem intuitive that the surface roughness would keep increasing for longer soaking times, but this is not the case. A plausible explanation would be that after 1 hour of soaking only some spots of the sample is leached, while after 24 hours and 5 days, the entire surface is leached. This effect is illustrated in Figure 5.4. Some spots could leach preferably due to defects. An article by Chen et al. explains how an increased vacancy of the B cations in perovskites would decrease the activation energy of the migration of A cations from the subsurface to the outside surface [58]. When there are more defects close to the surface it would lead to a larger space for the migration of Ba. This again will lead to increased leaching, due to, as explained by Neubrand et al., the dissolution of $BaTiO_3$ being a surface reaction [33]. When the entire surface is leached, this would create a lower S_A value, due to a decreased height difference. This also explains the increased standard deviation observed for the samples soaked at shorter time intervals. When only some spots on the surface area are leached, the surface roughness measurements will vary quite a lot, creating a large standard deviation. When the entire initial surface is dissolved, restructuring may also happen, due to the reconstruction of the surface of perovskites often being associated with metal leeching [58]. Surface reconstruction would create less surface roughness due to the lowering of energy.

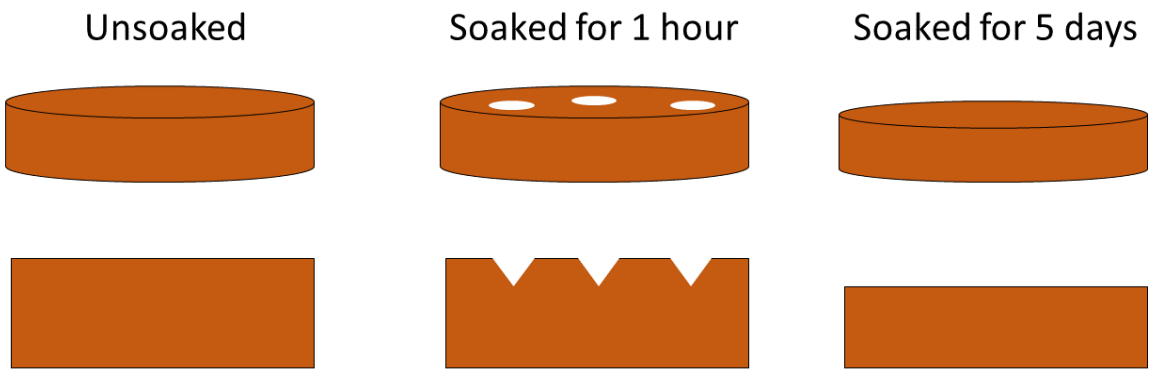

Figure 5.4: An illustration showing a simplified version of how it is predicted that the surface of BT is leached during soaking. The Figure shows both the side-view and side/top-view of the BT samples. After 1 hour of soaking only some spots on the surface are leached, and an initial roughening is observed. While after 5 days there is observed a smoothing of the surface, indicating that the entire surface is leached. It is important to note that this figure shows an exaggerated surface roughness effect, just to illustrate the message.

Figure 4.18 shows the effect of poling on the surface roughness and there does not seem to be a very clear trend. The unpoled samples show a similar increase as the medium-poled samples but have a much larger standard deviation. This could reveal a sign of increased leaching for the unpoled sample, which was suggested when studying the pH values. Though the S_A-value does not increase substantially more for the unpoled sample and drawing a conclusion based on the surface roughness data is therefore not possible.

5.3.2 Domain structure after soaking

One of the aims of the UPW soaking study was to compare the domain structure before and after soaking. The out-of-plane PFM results for the 1-hour soaked samples are presented in Figure 4.22. Due to dirt on the tip leading to poor resolution on the PFM images, comparing the pre and post-soaked domain structures of barium titanate is challenging. Piezoelectric force microscopy is a sophisticated and complex method where both measurement and data processing are important. Therefore a more thorough analysis, with an even cleaner sample, and where the sample is also rotated to combat the buckling effect is important. As explained in section 5.2.2,

the scanned area should also be marked, so there is an accurate representation of the domain structure pre and post-soaking. For further study on the domain structure after soaking there are some important questions that need to be answered. Do the domains get smaller or less prevalent after soaking? How the domains are affected after soaking, can give great insight into the biocompatibility and lifetime of the bone implant. A decrease in the size of the domains could indicate a decrease in poling, which could see a probable negative effect on the functional properties of the implant. Trying to figure out how the leaching of Ba^{2+} affects the domain structure is therefore of great importance.

5.3.3 Microstructure

No substantial change in the microstructure of the samples before and after soaking in UPW was observed, when comparing the SEM images in Figure 4.3 and 4.23. The 24-hour sample (Figure 4.23a) showed a larger amount of pores, than the 5-day soaked samples (Figure 4.23b). This could be seen in connection with the surface roughness data, showing a larger surface roughness increase after 24 hours of soaking than 5 days of soaking in UPW. However, the closing of pores would not be so likely during restructuring and leaching of the entire surface. Pores of similar size were also observed before soaking as seen in Figure 4.3. Therefore this effect of increased pores after 24 hours compared to after 5 days of soaking, could just be a result of the variation of microstructure on the surface of each sample and the variation between each sample. As seen in Figure 3.2, the relative densities for the different pellet batches varied quite a bit, and the soaking are performed on pellets from different batches.

Even though the SEM images do not show any significant differences, the EDS scan shows a decrease of Ba on the surface of the 5-day soaked sample. This is presented in Figure 5.5. As mentioned earlier, Ba and Ti have some overlapping x-ray energies, and the software allocates the signals randomly. Therefore the Ti EDS maps are also presented, to make sure that the software did not allocate the Ti and Ba very unevenly. For Figure 5.5a and Figure 5.5b the signals seem to be evenly distributed to an approximately 1:1 ratio, and the software is therefore not a source of error. After soaking, the EDS signal of the BT pellets is weaker, which is due to a shorter scanning time and resolution, but Figure 5.5d shows more dense signals than Figure 5.5c. From the chemical formula of $BaTiO_3$, the ratio of Ba and Ti should be 1:1, but after potential leaching of Ba^{2+}, the ratio is set to decrease. Therefore a stronger Ti signal than Ba signal, indicates leaching of Ba^{2+} ions after soaking in UPW for 5 days, but due to a lower scanning resolution, the pre and after-soaking images can not be compared quantitatively. The conclusion is therefore drawn by observing a more dense EDS map of Ti (Figure 5.5d) than Ba (Figure 5.5c) after soaking.

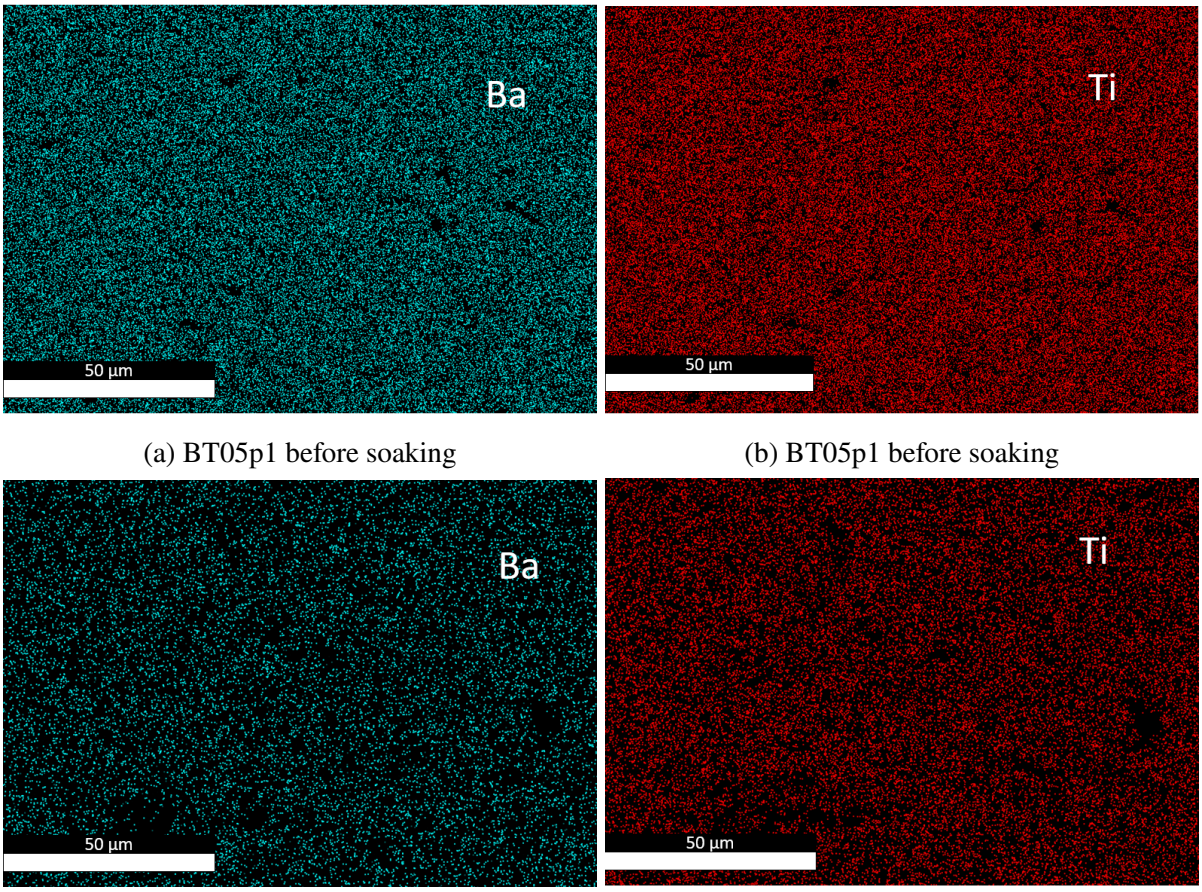

(a) BT05p1 before soaking

(b) BT05p1 before soaking

(c) BT05p1 after soaking

(d) BT05p1 after soaking

Figure 5.5: Comparison of barium and titanium EDS maps pre and post-soaking of BT05p1. The sample was unpoled and soaked for 5 days in UPW.

5.3.4 Phase purity

XRD measurements were also performed after soaking to study the effects on the bulk properties. The XRD diffractograms for the unpoled and high-poled samples for different soaking times in UPW are shown in Figure 4.21. The XRD diffractograms show no clear change in peak position after soaking. Therefore no severe structural rearrangement of the material has been undergone during soaking. The only significant change in the XRD diffractograms is the peak shapes for the peaks at $2\Theta = 22°$ and $2\Theta = 44-46°$. As shown in Figure 5.6, the left-hand side of the peak at $2\Theta = 22°$ increased for the poled samples soaked in UPW for 24 hours (orange graph) and 5 days (red graph). The same effect was seen for the peak at $2\Theta = 44-46°$, by studying Figure 4.21. However, this effect was not very consistent due to the diffractogram of the poled 1-hour soaked UPW sample (blue graph) showing a larger intensity of the right-hand side than the left-hand side of the peak at 22°. A study performed by Ghosh et al. in 2014 on poled barium titanate, supports the findings in this thesis [55]. Ghosh's results show a decreased intensity of the left side of the peak at $2\Theta = 44-46°$, after poling, while the right side intensity

increased [55]. The peak at 44-46° represents the ⟨200⟩ crystallographic planes in tetragonal BT [55]. Poling is a plausible cause for this intensity change, due to an applied electric field will theoretically change the domain structure and also lead to a subtle shift in the crystal structure. The peak intensity provides information on the crystallinity along specific planes, while the peak shape can express information on the lattice strain. A small change in the crystal structure after poling could therefore lead to lattice strains. This effect is therefore seen in connection with poling and not a soaking effect.

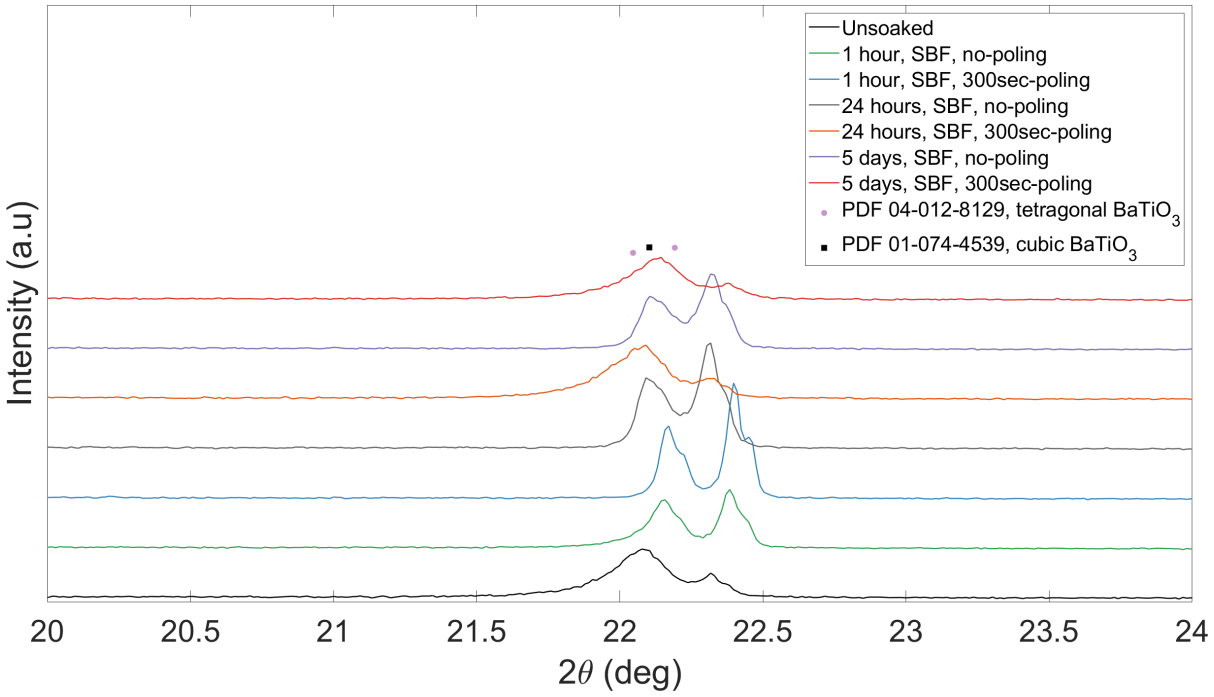

Figure 5.6: Zoomed in XRD diffractograms around the 22° peak, of the non-poled and high-poled BT pellets soaked in UPW. The XRD diffractogram of an unsoaked BT pellet is also added as seen in the black graph.

5.3.5 Piezoelectric properties

Before soaking

The main functional property of barium titanate for a bone implant application is the piezoelectric property. Therefore, multiple parallels of the BT samples, from different pellet batches, were studied to confirm consistency in the piezoelectric properties (Figure 4.10). BT04p1 and BT06p4 showed a characteristic hysteresis polarization loop, together with a butterfly-shaped strain loop, confirming that a piezoelectric material had been synthesized. BT01p3 and BT03p5, on the other hand, showed a higher degree of dielectric behavior when polarizing with an electric voltage of 1.5 kV. The polarization loop had not fully switched yet and was still relatively flat. By applying a higher electric field these samples also experienced a hysteresis loop. Reasons for this could be small variations in the microstructure, with for example a larger grain size

or more defects, leading to a higher electric voltage needed for polarization. Also, these samples (BT01p3,BT03p5) had a thickness of 1.1 µm, while the other samples (BT04p1,BT06p4) had a smaller thickness of around 0.95 µm. As described in the results section 4.3, even though the polarization loop was plotted against the electric field and normalized with respect to thickness, the same electric voltage was applied to all samples. A larger thickness would result in a lower external electric field when applying the same voltage, which would explain why BT01p3 and BT03p5 switched to a hysteresis loop at a higher electric voltage.

The piezoelectric coefficients for the BT samples are quite small, as seen in Table 4.2 but this is expected because these samples were unpoled. In an unpoled sample, the polarization directions are randomly aligned and the external electric field created from the direct piezoelectric effect is therefore in theory net-zero. This is explained in the theory sections 2.1 and 2.8. In experiments, it is expected to still see a small piezoelectric coefficient, due to some orientations being more energetically favored than others. The induced electric field for the application of bone implants is therefore predicted to increase by poling the piezoelectric material, as seen in the preliminary poling study (Figure 4.11).

After soaking

As explained in the theory section 2.3, a piezoelectric bone implant can mimic the stress-generated electrical potential in natural bone and promote bone healing and cellular growth. The introduction section explains the need for bone implants with increased lifetimes of over 20 years, and therefore it is important that the functional properties of the material are upheld while it is soaked in the body. For conducting further soaking studies on barium titanate it is consequently important that the piezoelectric properties are still existing after 5 days of soaking. The piezoelectric coefficients shown in Table 4.5 show a large increase in the d_{33}-values after poling which is expected due to the alignment of the polarization direction. These values are of a similar order to the piezoelectric coefficients for the preliminary poling study (Figure 4.11) performed before soaking. It, therefore, confirms that the poling is kept after soaking. The d_{33} absolute values of the high-poled BT samples after poling range from 127-222 pC/N. This is in accordance with literature values, ranging between 150-200 pC/N for poled BT samples with an average grain size between 10-100 µm [54].

The piezoelectric properties are also upheld after soaking in UPW, which is seen respectively for the unpoled and high-poled samples in Figure 4.32 and Figure 4.33. The figures show symmetrical ferroelectric hysteresis loops and butterfly-shaped strain curves. A prior study by Holum showed some broadening of the hysteresis loops of BT after soaking in UPW for 5 days [1]. This effect was not seen for the BT samples soaked in UPW this time. This could be due to the samples having an initial lower amount of defects before soaking or a less amount of pores.

5.4 Soaking study in SBF

The main goal of soaking the material in SBF was to study the effect of poling on precipitation. As explained in section 2.3, a piezoelectric material has been shown to enhance bone healing through the attraction and deposition of hydroxyapatite (calcium apatite). Simulated body fluid was used as the soaking media due to having ion concentrations mimicking the human blood plasma. Studying biomaterials using SBF is a well-known method, that is a precise *in-vitro* study method.

5.4.1 Precipitation after soaking

Weight changes

The first step in studying the effect of poling on the precipitation of the BT samples was weighing the samples. Precipitation on the surface of the BT samples will increase the weight while leaching of Ba^{2+} will theoretically decrease the weight. Figure 4.25 shows the weight change of the unpoled and poled BT samples for the different soaking time intervals and the poled samples all follow a similar trend. The poled samples decrease in weight until 1 day of soaking and increase by further soaking. This could be explained by the dissolution of $BaTiO_3$ happening mostly for the early part of soaking and after some days the precipitation increase and combat the initial weight decrease, leading to an approximately net zero weight change. The unpoled sample showed a decreased weight already after 1 hour, before increasing and then decreasing slightly up until 5 days of soaking. The rapid weight decrease for the unpoled sample can be seen in relation to the pH measurements that showed a large pH increase for the unpoled sample already after 1 hour. However, it is important to not draw any concluding remarks from the weight data, due to the changes only varying between $\Delta\text{wt\%} = -0.15\%$ and $\Delta\text{wt\%} = 0.05\%$. This is a marginal change that would be influenced by errors in the weight scale and calibration of the weight scale. Nonetheless, the weight change could possibly be considered significant, due to the leaching and precipitation being surface reactions and thus only covering a small volume of the sample. To confirm the results from the weight data, further studies of the precipitation had to be made.

Microstructure

The precipitation on the surface of the BT pellets was further studied using SEM. The SEM data show a clear correlation between soaking time, poling state, and precipitation. The 1-hour and 24-hour soaked BT pellets only show precipitation on the high-poled (300-second poled) sample, while the samples soaked for 5 days all experienced signs of precipitation. These microstructures are seen in Figure 4.26, 4.27, and 4.28. This behavior matches well with the theory described in section 2.7, and substantiates the hypothesis, that an increased poling would lead to more precipitation. A larger soaking time also gives the ions more time to adhere to the charged surface of barium titanate. The BT samples were placed with the negatively charged surface pointing upwards and it is predicted that the mechanism leading to precipitation is both due to gravity and the attraction of positive ions (Na^+, K^+, Ca^{2+}, Mg^{2+} etc.). This is justified by the unpoled sample only showing signs of precipitation after 5 days, due to not having a strong contribution from a charged surface. A similar effect of increased precipitation on a negatively charged surface of barium titanate is shown in 2001 by Park et al. [10]. The barium titanate discs were soaked in minimum essential medium (MEM) instead of SBF, but the ion concentrations in MEM are relatable to the ones in SBF. Park's research was focusing on the calcium apatite precipitates, and as described in section 2.7, increased precipitation of CaP is a good indication of the biocompatibility of the material. Therefore EDS had to be conducted in this thesis to determine which elements are present in the precipitates seen in Figure 4.26, 4.27, and 4.28. The precipitated crystals shown in Figure 4.29a, are presented in Figure 5.7, where the white crystal is marked with a red oval, and the irregular-shaped precipitate is marked with a blue oval.

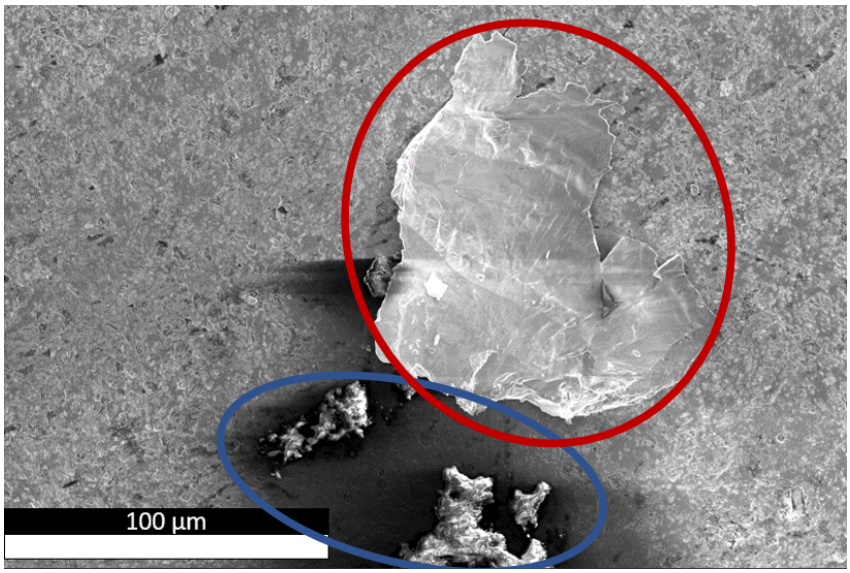

Figure 5.7: SEM image of the precipitates observed for the poled BT sample soaked in SBF for 5 days. The white crystal is marked with a red oval, while the irregular-shaped precipitate is marked with a blue oval.

The EDS data in Figure 4.29 does not give a clear understanding of the chemical properties of the precipitated crystals. The EDS maps show increased concentrations of carbon and calcium for the irregular-shaped precipitate, but a decrease in the barium, sulfur, phosphorous, and oxygen concentrations is observed. The Ca Lα1.2 energy overlaps with the C Kα1.2, and therefore the EDS maps can influence each other. The Kα energy of P, has some overlap with the Kα energy of the neighboring S. If the irregular-shaped precipitate was calcium apatite, it would be expected to see a similar EDS map for P as for Ca. The results are therefore in conflict with the general theory, that explains the formation of calcium phosphate in SBF through the following equation [59]:

$$Ca^{2+} + HPO_4{}^{2-} \leftrightarrow CaHPO_4. \tag{5.7}$$

The equilibrium constant at 37 °C is reported to be 681 [60]. This is a relatively large value, that would predict crystallization of CaP considering the ion concentrations in the SBF. A reason for not seeing a clear CaP precipitation could be that the polishing procedure creates a very flat BT surface that decreases the total surface area and therefore the total surface energy. Leng and Lu explain how the theoretical nucleation of CaP is exponentially related to the activation energy, which again is related to the surface energy [59]. A lower surface energy would therefore decrease the rate of nucleation. As explained in experimental section 3.4 the SBF-immersed pellets were carefully rinsed with UPW. This was done to remove loosely adhered precipitation, but to keep the predicted chemically adhered CaP left on the pellet. This rinsing method may actually have led to the removal of some CaP precipitates.

The EDS map of the white crystal shows the opposite trend of the irregular-shaped crystal. The white crystal has a higher concentration of O, S, Ba, and P than the irregular-shaped crystal, but it did not show an increased amount compared to the rest of the BT surface. The obtained EDS data does not provide sufficient information to conclude the chemical composition of the precipitation, but the SEM images show increased precipitation when extending the soaking time and poling time.

Surface roughness

The barium titanate pellets soaked in SBF show a similar trend in surface roughness as the pellets soaked in UPW, seen in Figure 4.17. The relative increase of the S_A-value is slightly higher for the BT pellets soaked in SBF than the ones soaked in UPW, and this is numerically presented in Table 5.1. A plausible reason for this is the precipitation on the surface of the SBF-soaked samples, creating a height difference and a larger average height, S_A. The precipitates are quite small so the effect is not drastic, but it is substantial. The standard deviation of the surface roughness measurements for the 24-hour and 5-day soaked samples soaked in UPW and SBF vary between 0.008-0.049 µm. This gives a relative standard deviation varying between 7.02% -20.2%. This was calculated by taking the standard deviation and dividing it by the average surface roughness of the BT samples for a given soaking time and media. The calculation is shown in Appendix C. The difference in surface roughness change (ΔS_A) between the samples soaked in UPW and SBF is in the range of the largest relative standard deviation of 20.2%. Even though, the surface roughness data can not confirm the findings in the SEM, due to a large relative standard deviation, it still shows signs of precipitation, by showing a trend of increased surface roughness for the SBF-soaked samples compared to the UPW-soaked samples.

Table 5.1: Relative surface roughness changes before and after soaking for the 24-hour and 5-day soaked BT samples.

Soaking time and media	S_A (before soaking)	S_A (after soaking)	ΔS_A [%]
24 hours, UPW	0.111	0.133	19.82
24 hours, SBF	0.179	0.243	35.75
5 days, UPW	0.112	0.114	1.79
5 days, SBF	0.101	0.112	10.89

5.4.2 Phase purity

The XRD diffractograms of the soaked samples fit well with the diffractogram for the unsoaked sample. This can indicate that any eventual precipitation was too thin or only present in small amounts and therefore did not change the XRD diffractograms. The XRD measurement run was a bulk XRD, and therefore the x-rays reached further into the sample, and the precipitation did not change the diffractograms. The same effect of poling described in section 5.3.4, is also observed for the poled BT samples soaked in SBF. This is seen in Figure 4.20, where all the poled BT samples show increased intensity of the left side of the 22° peak in the XRD diffractograms. This data further supports the findings by Ghosh et al. [55].

5.4.3 Piezoelectric properties

The piezoelectric properties after soaking in SBF show similar behavior as after soaking in UPW, except for the unpoled sample soaked in SBF for 24 hours (BT03p5). This is seen in Figure 4.30 as a large broadening of the polarization loop, indicating leakage current. A leakage current is defined as a current that flows through a supposedly insulating boundary. As explained earlier the main form of dissolution of the BT surface is through the leaching of Ba^{2+} ions. This will create potential barium and oxygen vacancies, and these defects on the surface can create a pathway for the current to travel through the initially non-conductive barium titanate sample. Due to the surface roughness measurements indicating an increased roughness after soaking, it is expected that the defects are on the surface of the sample. This means that the current flows at the surface and not through the sample. The polarization loops are made by measuring the current, which means that an increased leakage current does lead to an added current being measured, which will lead to a broadening of the polarization loops. It is also worth mentioning that increased Ba^{2+} leaching during soaking could lead to a TiO_2 outer layer. TiO_2 is not piezoelectric and this outer layer could therefore worsen the piezoelectric properties of the BT pellets. This was not observed, due to most of the samples showing the same piezoelectric properties before and after soaking.

The poled samples already have an internal electric field, due to an alignment in the polarization direction after poling. In the piezoelectric measurements, an external electric field is applied for 7 seconds, and this does not give the material enough time to flip completely back to a neutral poling state. Therefore the poled samples experience asymmetrical polarization loops for the first piezoelectric measurements. The piezoelectric measurements were done by linearly increasing the electric voltage up to 1.5 kV. By studying Figure 5.8, the BT02p6 (1-hour soaked SBF) sample does not reach a positive remnant polarization when poling at 600 V, due to the initial internal negative electric polarization in the material. By increasing the electric voltage the hysteresis loop becomes more symmetrical and reaches an approximately similar negative

and positive remnant polarization. However, when applying a 1.5 kV electric voltage, there was still observed a shift on the x-axis of the hysteresis loops towards larger electric field values, as seen in Figure 4.31. This offset is explained by the external electric field having to overcome the internal polarization of the poled material. Therefore the polarization response begins at a higher electric field, creating a shift in the hysteresis loop.

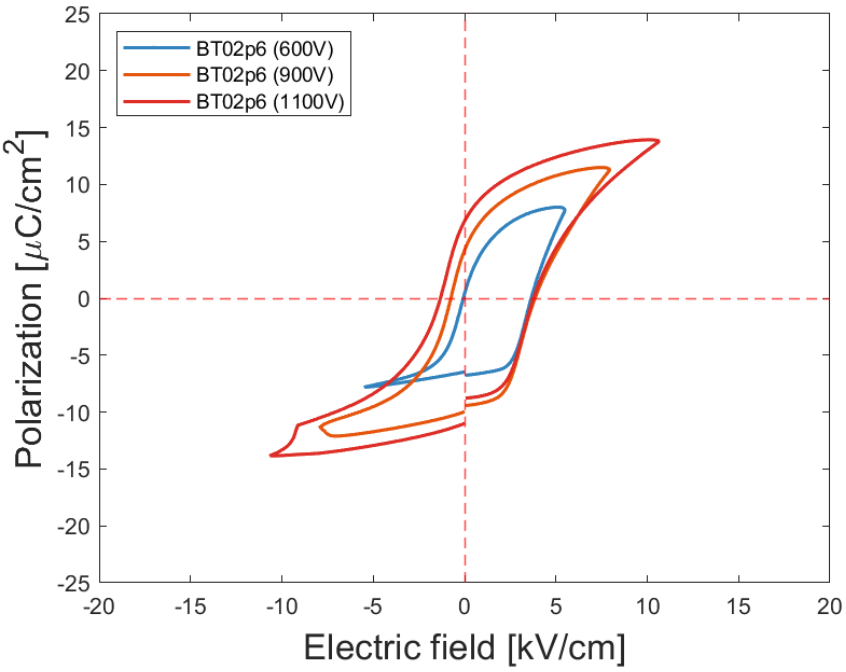

Figure 5.8: The polarization loops of increased applied external field during piezoelectric measurements on BT02p6 after soaking in SBF for 1 hour.

6 Conclusion

In this work, barium titanate has been synthesized through a solid-state synthesis and the microstructure has been improved. It can be concluded that by increasing the sintering temperature to 1350 °C the $BaTiO_3$ microstructure showed a unimodal grain size distribution of grains at the micrometer scale. By changing the synthesis equipment some small unidentified peaks in the XRD diffractograms declined in intensity, and the secondary phase was no longer of substantial significance. A preliminary poling study gave great insight into the behavior of barium titanate when applying an electric field using a corona discharge setup. The BT pellets experienced a semi-linear increase in the piezoelectric coefficients before reaching saturation. This polarization alignment after poling was also studied using PFM. By improving the polishing procedure, the BT sample surface topography was on the nanometer scale and both the herringbone domain pattern and stripe domain pattern was observed. A predicted size increase of the domains after poling was not observed, and a more thorough PFM analysis has to be performed.

The main conclusion in this thesis can be drawn from the soaking studies. The UPW soaking study gave great insight into the mechanism of Ba^{2+} leaching on the BT surface, through the pH and surface roughness data. Both of the data indicated strongly that the dissolution of BT is a surface reaction and that the leaching is rapid at the early stage of soaking before reaching a plateau. This correlates well with prior research [33–35]. The UPW soaking study also indicated reduced leaching of Ba^{2+} and increased chemical stability for the poled samples. Furthermore, the EDS data showed indication of Ba^{2+} leaching, due to a larger x-ray signal of Ti than Ba.

The BT samples were also soaked in simulated body fluid, and a clear positive correlation between precipitation, poling, and soaking time was demonstrated. An increased poling of barium titanate, leads to a charged surface attracting ions, while an extended soaking time gives the ions more time to adhere to the surface. The SEM results showed clear evidence of precipitation, while both the weight data and surface roughness data also showed supporting results. The EDS data was not able to confirm the chemical composition of the precipitates, and further studies need to be conducted. Due to the EDS data not being able to confirm the presence of CaP, any conclusions on the effect of poling on the biocompatibility of BT can not be drawn.

Most importantly, the BT pellets showed great piezoelectric properties before and after soaking. A conclusion can be made that the piezoelectric properties of $BaTiO_3$ are intact, even though leaching of Ba^{2+} was experienced. This was crucial and promising for the onward research on barium titanate as a model system for ferroelectric bone implants. To be able to increase the lifetime of such implants, it is important that the functional properties are upheld after soaking. It can be concluded that poling of $BaTiO_3$ increased the piezoelectric coefficient, together with

showing signs of increased chemical stability, and increased precipitation on the surface. This is also encouraging results for the further study of barium titanate in the use of bone implants.

7 Further work

This thesis aimed to study the effect of electrical poling and soaking on the domain structure and chemical surface properties of barium titanate. By soaking $BaTiO_3$ in ultrapure water for 5 days, great insight into the behavior of Ba^{2+} leaching was made. It indicated that most of the leaching happens at the early stage. Therefore, by performing a soaking study with shorter time intervals for the first hours, a more accurate description of the chemical stability of $BaTiO_3$ can be made. The overarching goal is to create bone implants with increased lifetime, and therefore soaking studies longer than 5 days also have to be performed. Running a soaking study with simulated body fluid over a longer time period would give an increased understanding of the precipitation on the surface. By performing a more thorough SBF soaking study, better EDS data can be gathered and the presence of CaP can hopefully be determined.

This thesis also presents the domain structure of $BaTiO_3$, but a more thorough PFM study on barium titanate, both before and after soaking has to be performed. PFM is a complex characterization method and for further work, a dedicated study only observing the domain structure should be carried out. The out-of-plane polarization direction of the different domains can be determined by rotating the sample and removing the buckling effect. This study has shown that it is difficult to compare domain structures of different polycrystalline samples. For further studies, the same sample should be measured with PFM and for each poling step the structure of the domain has to be measured and the area has to be marked. An enhanced study on the domain structure of barium titanate, could help explain how the ferroelectric domains are affected by soaking, and give extensive insight into the biocompatibility and lifetime of a piezoelectric bone implant.

References

[1] Vetle Holum. Effect of soaking on the chemical stability and microstructure of ferroelectric implant materials, 2022.

[2] S.F. Hulbert, J.J. Klawitter, and L.S. Bowman. History of ceramic orthopedic implants. *Materials Research Bulletin*, 7(11):1239–1246, 1972.

[3] B.J. McEntire, B.S. Bal, M.N. Rahaman, J. Chevalier, and G. Pezzotti. Ceramics and ceramic coatings in orthopaedics. *Journal of the European Ceramic Society*, 35(16):4327–4369, 2015.

[4] Charlotte Skjöldebrand, Joanne L. Tipper, Peter Hatto, Michael Bryant, Richard M. Hall, and Cecilia Persson. Current status and future potential of wear-resistant coatings and articulating surfaces for hip and knee implants. *Materials Today Bio*, 15:100270, 2022.

[5] Marco P Soares dos Santos and Rodrigo M. C. Bernardo. Bioelectronic multifunctional bone implants: recent trends. *Bioelectronic medicine*, 8, 2022.

[6] Giuseppe Pezzoti. *Advanced materials for joint implants*. Pan Standford Publishing Pte.Ltd, Singapore, 2013.

[7] M. Acosta, N. Novak, V. Rojas, S. Patel, R. Vaish, J. Koruza, G. A. Rossetti, and J. Rödel. $BaTiO_3$-based piezoelectrics: Fundamentals, current status, and perspectives. *Applied Physics Reviews*, 4(4):041305, 2017.

[8] Amir Hossein Rajabi, Michael Jaffe, and Treena Livingston Arinzeh. Piezoelectric materials for tissue regeneration: A review. *Acta Biomaterialia*, 24:12–23, 2015.

[9] Eiichi Fukada and Iwao Yasuda. On the piezoelectric effect of bone. *Journal of the Physical Society of Japan*, 12(10):1158–1162, 1957.

[10] Yeong-Joon Park, Kyu-Seog Hwang, Jong-Eun Song, Joo L Ong, and H Ralph Rawls. Growth of calcium phosphate on poling treated ferroelectric batio3 ceramics. *Biomaterials*, 23(18):3859–3864, 2002.

[11] Kenji Uchino. *Advanced piezoelectric materials*. Woodhead Publishing Limited, Cambridge,UK, 2010.

[12] L.S. Miller and J.B. Mulling. *Electronic materials from silicon to organics*. Springer, New York, 1991.

[13] A.R. L.S. West. *Solid state chemistry and its applications*. Wiley, Chichester, 2014.

[14] Li Jin, Fei Li, and Shujun Zhang. Decoding the fingerprint of ferroelectric loops: Com-

prehension of the material properties and structures. *Journal of the American Ceramic Society*, 97(1):1–27, 2014.

[15] Hrishikesh Kulkarni, Khaja Zohaib, A. Khusru, and K. Shravan Aiyappa. Application of piezoelectric technology in automotive systems. *Materials Today: Proceedings*, 5(10, Part 1):21299–21304, 2018. International Conference on Smart Engineering Materials (ICSEM 2016), October 20-22, 2016.

[16] Heung Soo Kim, Joo-Hyong Kim, and Jaehwan Kim. A review of piezoelectric energy harvesting based on vibration. *International Journal of Precision Engineering and Manufacturing*, 2011.

[17] Ashish Kumar, Arathy Varghese, Anup Sharma, Mahanth Prasad, Vijay Janyani, R.P. Yadav, and Khaled Elgaid. Recent development and futuristic applications of mems based piezoelectric microphones. *Sensors and Actuators A: Physical*, 347:113887, 2022.

[18] Joon Park and R.S. Lakes. *Biomaterials: an introduction*. Springer Science & Business Media, New York, 3rd edition, 2007.

[19] Denitsa D Kiradzhiyska and Rositsa D Mantcheva. Overview of biocompatible materials and their use in medicine. *Folia Med (Plovdiv)*, 61(1):34–40, 2019.

[20] Giuseppe Pezzotti. Bioceramics for hip joints: The physical chemistry viewpoint. *Materials*, 7(6):4367–4410, 2014.

[21] D.F. Williams. Bioinertness: An outdated principle. *Tissue Engineering of Prosthetic Vascular Graft*, 1999.

[22] Iain H. Kalfas. Principles of bone healing. *Neurosurgical Focus FOC*, 10(4):1 – 4, 2001.

[23] F. R. Baxter, C. R. Bowen, I. G. Turner, and A. C. E. Dent. Electrically Active Bioceramics: A Review of Interfacial Responses. *Annals of Biomedical Engineering*, 38(6):2079–2092, 2010.

[24] M. Cerrolaza, V. Duarte, and D. Garzon-Alvarado. Analysis of bone remodeling under piezoelectricity effects using boundary elements. *J Bionic Eng*, 14:659–671, 2017.

[25] JE Davies. The importance and measurement of surface charge species in cell behaviour at the biomaterial interface. *Surface characterisation of biomaterials*, pages 219–223, 1988.

[26] Jürgen Rödel, Wook Jo, Klaus T. P. Seifert, Eva-Maria Anton, Torsten Granzow, and Dragan Damjanovic. Perspective on the Development of Lead-free Piezoceramics. *Journal of the American Ceramic Society*, 92(6):1153–1177, 2009.

[27] Julia García-Lestón, Josefina Méndez, Eduardo Pásaro, and Blanca Laffon. Genotoxic effects of lead: An updated review. *Environment International*, 36(6):623–636, 2010.

[28] Goldschmidt VM. Geochemisce verterlungsgesetze der elemente. *Norsk Videnskap*, 1927.

[29] Sindre Tuset. Dft studies of $BaTiO_3$ interfaces, 2016.

[30] Jigong Hao, Wei Li, Jiwei Zhai, and Haydn Chen. Progress in high-strain perovskite piezoelectric ceramics. *Materials Science and Engineering: R: Reports*, 135:1–57, 2019.

[31] Tadashi Kokubo and Hiroaki Takadama. How useful is SBF in predicting in vivo bone bioactivity? *Biomaterials*, 27(15):2907–2915, 2006.

[32] Atkins P.W. *Physical chemistry*. Oxford University Press, 9 edition, 2010.

[33] Achim Neubrand, Reinhard Lindner, and Peter Hoffmann. Room-temperature solubility behavior of barium titanate in aqueous media. *Journal of the American Ceramic Society*, 83(4):860–864, 2000.

[34] M.C. Blanco-Lopez, B. Rand, and F.L. Riley. The properties of aqueous phase suspensions of barium titanate. *Journal of the European Ceramic Society*, 17(2):281–287, 1997.

[35] M.C.Blanco López, G. Fourlaris, and F.L. Riley. Interaction of barium titanate powders with an aqueous suspending medium. *Journal of the European Ceramic Society*, 18(14):2183–2192, 1998.

[36] Florence Barrère, Clemens A. van Blitterswijk, and Klaas de Groot. Bone regeneration: Molecular and cellular interactions with calcium phosphate ceramics. *International Journal of Nanomedicine*, 1(3):317 – 332, 2006. Cited by: 435.

[37] Rolf Landauer. Electrostatic considerations in $BaTiO_3$ domain formation during polarization reversal. *Journal of Applied Physics*, 28(2):227–234, 1957.

[38] Jacob L. Jones, Elliott B. Slamovich, and Keith J. Bowman. Domain texture distributions in tetragonal lead zirconate titanate by x-ray and neutron diffraction. *Journal of Applied Physics*, 97(3), 01 2005. 034113.

[39] A. Pathak and R.M. McMeeking. Three-dimensional finite element simulations of ferroelectric polycrystals under electrical and mechanical loading. *Journal of the Mechanics and Physics of Solids*, 56(2):663–683, 2008.

[40] Dragan Damjanovic. Ferroelectric, dielectric and piezoelectric properties of ferroelectric thin films and ceramics. *Reports on Progress in Physics*, 61(9):1267, sep 1998.

[41] Haidong Lu, Yueze Tan, Leonie Richarz, Jiali He, Bo Wang, Dennis Meier, Long-Qing

Chen, and Alexei Gruverman. Electromechanics of domain walls in uniaxial ferroelectrics. *Advanced Functional Materials*, 33(15):2213684, 2023.

[42] Bert Voigtländer. *Atomic force microscopy*. Springer Cham, Switzerland, 2nd edition, 2020.

[43] Brian J. Rodriguez, Sergei V. Kalinin, Stephen Jesse, G. Thompson, A. Vertegel, Sophia Hohlbauch, and Roger Proksch. Nanoelectromechanics of inorganic and biological systems: From structural imaging to local functionalities. *Microscopy Today*, 16(1):28–33, 2008.

[44] Elisabeth Soergel. Piezoresponse force microscopy (pfm). *Journal of Physics D: Applied Physics*, 44(46):464003, nov 2011.

[45] Maria Teresa Buscaglia, Marta Bassoli, Vincenzo Buscaglia, and Rocco Alessio. Solid-state synthesis of ultrafine $BaTiO_3$ powders from nanocrystalline baco3 and tio2. *Journal of the American Ceramic Society*, 88(9):2374–2379, 2005.

[46] David W. Richerson. *Modern ceramic engineering: Properties, processing and use in design*. CRC Press, Taylor & Francis Group, Florida, 3rd edition, 2006.

[47] Sangkyu Lee, Ungyu Paik, Vincent A. Hackley, Yeon-Gil Jung, and Kyung-Jin Yoon. Microstructure and permittivity of sintered $BaTiO_3$: influence of particle surface chemistry in an aqueous medium. *Materials Research Bulletin*, 39(1):93–102, 2004.

[48] Shih-Chun Lu, Yin-Hua Chen, Wei-Hsing Tuan, Jay Shieh, and Chin-Yi Chen. Effect of microstructure on dielectric and fatigue strengths of $BaTiO_3$. *Journal of the European Ceramic Society*, 30(12):2569–2576, 2010.

[49] Magnus Rotan, Mikalai Zhuk, and Julia Glaum. Activation of ferroelectric implant ceramics by corona discharge poling. *Journal of the European Ceramic Society*, 40(15):5402–5409, 2020.

[50] Marcus Hoseth Bentzen. Aerosol deposited piezoelectric ceramic coatings for biomedical applications, 2021.

[51] K. S. Mazdiyasni, R. T. Dolloff, and J. S. Smith II. Preparation of high-purity submicron barium titanate powders. *Journal of the American Ceramic Society*, 52(10):523–526, 1969.

[52] Truman S. Light, Elisabeth A. Kingsman, and Anthony C. Bevilacqua. The conductivity of low concentrations of CO_2 dissolved in ultrapure water from 0-100 ℃. *American Chemical Society National Meeting*, 1995.

[53] Shih-Chun Lu, Yin-Hua Chen, Wei-Hsing Tuan, Jay Shieh, and Chin-Yi Chen. Effect of microstructure on dielectric and fatigue strengths of $BaTiO_3$. *Journal of the European Ceramic Society*, 30(12):2569–2576, 2010.

[54] P. Zheng, J.L. Zhang, Y.Q. Tan, and C.L. Wang. Grain-size effects on dielectric and piezoelectric properties of poled $BaTiO_3$ ceramics. *Acta Materialia*, 60(13):5022–5030, 2012.

[55] Dipankar Ghosh, Akito Sakata, Jared Carter, Pam A. Thomas, Hyuksu Han, Juan C. Nino, and Jacob L. Jones. Domain wall displacement is the origin of superior permittivity and piezoelectricity in batio3 at intermediate grain sizes. *Advanced Functional Materials*, 24(7):885–896, 2014.

[56] Sushree Swarupa Tripathy and Ashok M. Raichur. Dissolution properties of batio3 nanoparticles in aqueous suspensions. *Journal of Experimental Nanoscience*, 6(2):127–137, 2011.

[57] Yuji Shindo, Yuichi Fujioka, Kazuhisa Takeuchi, and Hiroshi Komiyama. Kinetics on the dissolution of co2 into water from the surface of co2 hydrate at high pressure. *International Journal of Chemical Kinetics*, 27(6):569–575, 1995.

[58] Yubo Chen, Yuanmiao Sun, Maoyu Wang, Jingxian Wang, Haiyan Li, Shibo Xi, Chao Wei, Pinxian Xi, George E Sterbinsky, John W Freeland, Adrian C Fisher, Joel W Ager, 3rd, Zhenxing Feng, and Zhichuan J Xu. Lattice site-dependent metal leaching in perovskites toward a honeycomb-like water oxidation catalyst. *Sci. Adv.*, 7(50), December 2021.

[59] Xiong Lu and Yang Leng. Theoretical analysis of calcium phosphate precipitation in simulated body fluid. *Biomaterials*, 26(10):1097–1108, 2005.

[60] A Chughtai, R Marshall, and G H Nancollas. Complexes in calcium phosphate solutions. *J Phys Chem*, 72(1):208–211, January 1968.

A Crystallographic data used for VESTA

Table A.1: The table shows the crystallographic data (CIF files) used for making the unit cells in VESTA, which is presented in Figure 2.4. The unit length of a and b is the same, and $\alpha = \beta = \gamma$ for both space groups.

Space group	CIF filename	a (Å)	c (Å)	$\alpha(^\circ)$
P4mm	1507756	3.99990	4.01700	90
$Pm\bar{3}m$	1542140	3.99600	3.99600	90

B Calculation of weight of precursors

The calculation of the theoretical weight of the precursors is based on reaction B.1.

$$BaCO_3(s) + TiO_2(s) \longrightarrow BaTiO_3(s) + CO_2(g) \tag{B.1}$$

Reaction B.1 shows a stoichiometry of $BaCO_3$, TiO_2, $BaTiO_3$ being 1:1:1. As shown in Table 3.5, the theoretical weight of $BaTiO_3$ for Batch1 and Batch3 was 20 g, while the theoretical weight for Batch2 was 14 g. The theoretical mole is calculated using equation B.2.

$$n = \frac{m}{M} \tag{B.2}$$

where n is moles, m is the mass and M is the molar mass. The molar mass of $BaTiO_3$ is $M_{BaTiO_3} = 233.1922\frac{g}{mol}$. The theoretical moles of $BaTiO_3$ for the different batches can then be calculated:

$$n_{BaTiO_3} = \frac{m_{BaTiO_3}}{M_{BaTiO_3}} \tag{B.3}$$

$$n_{BaTiO_3} = \frac{20g}{233.1922\frac{g}{mol}} = 0.0858 \tag{B.4}$$

$$n_{BaTiO_3} = \frac{14g}{233.1922\frac{g}{mol}} = 0.0600 \tag{B.5}$$

The molar mass of $BaCO_3$ and TiO_2 is respectively $n_{BaCO_3} = 197.3359g$ and $n_{TiO_2} = 79.8658g$. This gives the theoretical precursor masses for Batch1, Batch2, and Batch3:

$$m = M * n \tag{B.6}$$

$$m_{BaCO_3}(\text{Batch1 and Batch3}) = 197.3359\frac{g}{mol} * 0.0858mol = 16.9251g \tag{B.7}$$

$$m_{TiO_2}(\text{Batch1 and Batch3}) = 79.8658\frac{g}{mol} * 0.0858mol = 6.8498g \tag{B.8}$$

$$m_{\mathrm{BaCO_3}}(\mathrm{Batch2}) = 197.3359\frac{g}{mol} * 0.0600mol = 11.8479g \tag{B.9}$$

$$m_{\mathrm{TiO_2}}(\mathrm{Batch2}) = 79.8658\frac{g}{mol} * 0.0600mol = 4.7949g \tag{B.10}$$

C Calculation of relative standard deviation (RSD) of the surface roughness

The relative standard deviation is given by equation C.1.

$$\mathrm{RSD} = \frac{\sigma}{\mu} \cdot 100, \tag{C.1}$$

where σ is the standard deviation and μ is the average surface roughness value of BT samples for a given soaking time and media. This gives the calculated values of relative standard deviation as follows:

$$\mathrm{RSD} = \frac{\sigma}{\mu} = \frac{0.008\,\mu\mathrm{m}}{0.114\,\mu\mathrm{m}} * 100 = 7.02\% \tag{C.2}$$

$$\mathrm{RSD} = \frac{\sigma}{\mu} = \frac{0.049\,\mu\mathrm{m}}{0.243\,\mu\mathrm{m}} * 100 = 20.2\% \tag{C.3}$$

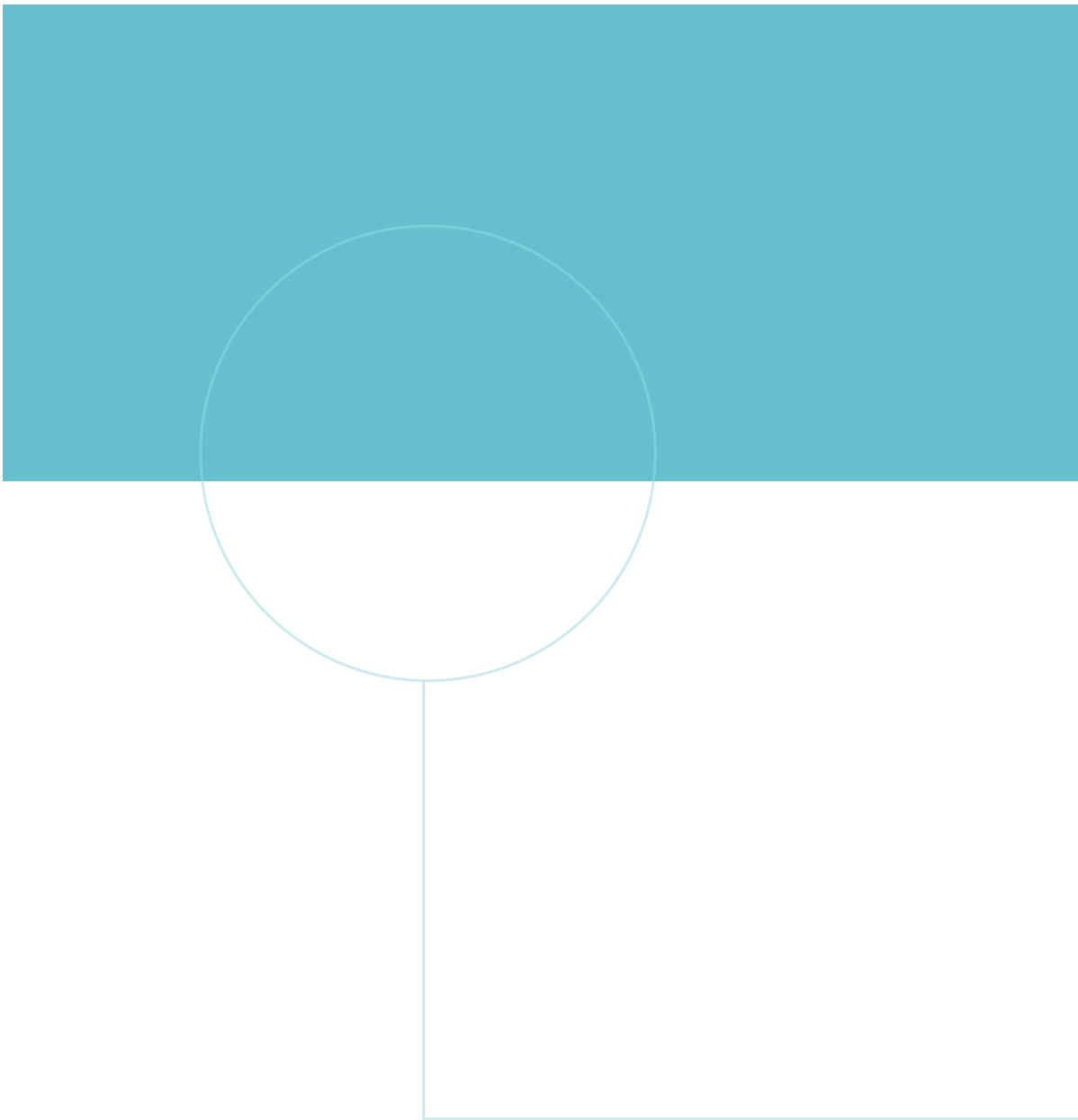

NTNU

Norwegian University of
Science and Technology